| | |
|---|---|
| Title | Irradiation effect of Ortho deuterium for UCN source |
| Author(s) | 三島, 賢二 |
| Citation | 大阪大学, 2004, 博士論文 |
| Version Type | VoR |
| URL | https://hdl.handle.net/11094/1879 |
| rights | |
| Note | |

Dissertation Submitted to
Graduate School of Science of Osaka University
for a Doctorate of Science

# Irradiation effect of Ortho deuterium for UCN source

Kenji Mishima

-2004-
Research Center for Nuclear Physics (RCNP), Osaka University

# Abstract

Production of ultra-cold neutrons (UCN) by a solid deuterium ($sD_2$) in the ortho state has been offered as one of the powerful UCN sources for fundamental physics research. However, since this type of UCN source is usually exposed to strong radiations generated by a spallation target nearby, there may be a serious conversion from the ortho to para $D_2$, which eventually deteriorates the UCN source performance.

In the present work, the irradiation effect on the ortho $sD_2$ at 25 K (liquid phase) was experimentally investigated by the SINQ (Spallation Neutron Source) at PSI (Paul Scherrer Institute), Zürich, Switzerland and the 30-MeV Electron LINAC at KURRI (Kyoto University Research Reactor Institute), Kumatori, Kyoto University.

In the former experiment, the ortho-$D_2$ fractions sampled from the SINQ moderator twice during few month were measured by means of the Raman spectroscopy with a 70-mW Ar ion laser, from which one can deduce information on the equilibrated ortho/para ratios determined from the competing processes between the ortho- to para-$D_2$ and vice versa.

In the latter experiment, the ortho-$D_2$ fractions sampled from the ortho-$D_2$ irradiated by Bremsstrahlung gamma-rays generated by the LINAC were measured also by means of the Raman spectroscopy with a 10-W Ar ion laser at Dept. of Physics, Kobe University. To investigate the ortho fractions varied with the radiation dose, absolute values of radiation dose were measured by using the foil activation analysis in corporation with energy spectra of gamma-rays calculated with the Monte Carlo simulation, Geant4.

The experimental results were analyzed by solving the rate equations, in which conversion effects from the ortho- to para-$D_2$, and vice versa caused by complicated processes such as dissociations, recombination for relevant $D_2$ molecules, D atoms, $D^+$, $D^-$ ions, and impure molecules playing in the $D_2$ sample were reasonably taken into account.

One of the striking results deduced from our measurement is that the conversion rate from the ortho- to para-$D_2$ due to irradiation is larger by a factor 5 than the established value so far, which suggests participation of unknown conversion

processes to explain our enhanced conversion rate. We propose a novel process relevant with $D_3^+$ ion as one of candidates for this enhancement.

According to our established model calculation, the ortho fraction is expected to be no serious effect on a realizable UCN density for the source planned at PSI.

Acknowledgements

First of all, I am grateful to Masayoshi Tanaka, Masahiko Utsuro and Yasuki Nagai for guidance in carrying out this research and discussion.

I greatly appreciate Klaus Kirch, Manfred Daum and Reinhold Henneck for carrying out this research in PSI. I also thank Tomasz Brys and Martin Giersch for help my work, and Gregor Knopp for discussion about Raman spectroscopy.

I also thank to corroborators for experiment at KURRI, Yoshiaki Kiyanagi and Motoki Ooi for experiment and discussion, Katsuhei Kobayashi, Kiyoshi Okumura, Hirohumi Yoshino and Masahiro Hino for the experiment setup, Kiyoshi Takami and Toshiharu Takahashi for operation the linac, and Jitsuya Takada for operation of the germanium detector.

I am grateful to Yukio Hukuda and Toshiro Komoto for Raman spectroscopy. I thank for Takamasa Momose for discussion about hydrogen properties.

I appreciate Tatushi Shima for the discussions of fundamental physics. I thank to Hiroyuki Makii, Mariko Segawa, and Atsushi Tomyo for the help to use simulation and other computer problems.

Finally I would like to express my special thanks to family for supporting my school life.

Contents

# Chapter 1 Introduction

Neutrons with kinetic energies less than 330 neV can be trapped in material bottles due to the almost complete reflection by the Fermi potential and are called as ultra cold neutrons (UCNs) [1]. Since UCNs are stored in the bottles for a long time, they have been working as one of the most excellent probes to measure the neutron electric dipole moment[2] or neutron lifetime[3][4] for study on the fundamental physics toward verification of the standard model and beyond from the T (or CP) violation and the unitarity of the CKM matrix element. UCNs may also prove usefulness in fundamental study on the gravitational force[5]. However, all of above experimental programs are limited by the available UCN intensities. Enormous efforts have been exerted at many labs in the world toward realization of the UCN sources with high intensity. A superthermal UCN source with superfluid $^4$He has been offered as one of promising UCN sources with high intensity since the first suggestion and subsequent experimental verification [7][8][9]. In fact, this method is more advantageous than others, since the limitations to the accumulated UCN intensity are determined only by wall losses and neutron beta decay, while no neutron losses by $^4$He.

It has been pointed out that a few other materials, such as solid deuterium ($sD_2$) satisfy criteria as superthermal production. The validity of UCN source based on the $sD_2$ has already been demonstrated at Los Alamos Los Alamos National Laboratory[10] in 2002. Further, at Paul Scherrer Institute (PSI), a strong deuterium UCN source is under construction[11] in combination with the Mega Watt spallation neutron source (SUNS). This UCN source at PSI aims at production of UCN density over 2000 UCN/cm$^3$. The limiting UCN density with this method is given by the product of UCN production rate P, and the lifetime $\tau$ of UCN while presenting in the $sD_2$. Here, P is proportional to the neutron flux, while $\tau$ depends severely on the characteristic behavior of the $sD_2$, particularly on ortho/para ratios.

A deuterium has two molecular states, i.e., ortho and para, according to the symmetry of the wave functions for nuclear spins. At low temperature limit, all of the ortho deuterium is in the ground state, and all of the para deuterium is in the first excited state at 7 meV above the ground state. It is known that for the deuterium at the excited state the up-scattering cross section of UCN is 10 times larger than that for the ground state[12]. Therefore, an ortho rich deuterium is required as a suitable UCN converter. However, at room temperature, a normal deuterium consists of 67% of ortho- and 33% of para-$D_2$. Fortunately, for practical use of $sD_2$ as a UCN converter, we can produce an $sD_2$ enriched with the orth-$D_2$ by using a catalyst at a triple point of $D_2$ (~18.7 K) with ease.

In spite of the great advantage in easy handling for the $sD_2$ UCN source relative to the UCN source based on superfluid $^4$He, the former source has been discussed on its practicability in terms of the performance deterioration due to increase of the para-$D_2$ by irradiation. Therefore, to investigate the irradiation effect on the ortho/para-$D_2$ ratio is of crucial importance in proving the validity of the UCN source with the $sD_2$ converter.

On the basis of the abovce aspect, the motivation of present work is summarized as follows:

1) to investigate the change of ortho-/para-$D_2$ ratio according as the irradiation time and to theoretically discuss the possible mechanism of the irradiation effect in comparison with the data and theories so far,
2) to provide the data for optimization of the $sD_2$ UCN source, SUNS[11].

Though the irradiation effect should basically be investigated with the $sD_2$, our measurement must compromise with a liquid deuterium because sampling of irradiated deuterium with the solid phase was technically difficult.

Firstly, the measurement was done with the spallation neutron source, SINQ at PSI, where a liquid $D_2$ was exposed with cold neutrons with a high flux (the heat deposit on the liquid $D_2$ was ~230 mW/g) continuously for a long period with some interruptions[13]. To measure the ortho-/para-$D_2$ ratios the Raman spectroscopy was employed. For this purpose, a 488-nm line from an Ar ion laser was used for generating the Raman scattering lines and a double monochrometer with a CCD detector, was set up, and was adjusted for automatic data acquisition system allowing high counting statistics. The primary aim of the measurement at PSI is to examine the ortho- to para-$D_2$ conversion in terms of dissociation of the ortho-$D_2$ into two deuteron atoms followed by subsequent recombination making an ortho-/para- ratio (2:1) corresponding to the high temperature limit. However, the measurement at PSI was too ambiguous to settle the theoretical model definitely. In fact, the irradiation period was over 9 months, the measured results on the relaxation of the ortho- to para-$D_2$ were almost those for the steady state, which masks behavior occurring in a short period. This, eventually, makes it difficult to discuss the role of dissociated deuteron atoms and that of the wall relaxation. Further, there was ambiguity in the sampling process of irradiated $D_2$ in its gas phase because the gas feeding system at SINQ was somehow complex allowing mixture of other gases.

Secondly, to overcome above difficulties, an experiment at KURRI (Kyoto University Research Reactor Institute) was planned to enable measuring the time dependence of the ortho-/para-$D_2$ in a short period, and more reliable data sampling. For this purpose, we used a 33-MeV electron beam from the electron linac[14]. Incidence of the electron beam on a thick Ta target generated strong Bremsstrahlung gamma-rays and the gamma-rays was incident on a liquid $D_2$ with a heat deposit of about 100 mW/g through a tungsten collimator. Here, most of the liquid $D_2$ was purified to the ortho-$D_2$ by using a catalyst in advance to the irradiation measurement. Interestingly the conversion rates deduced from the time dependent measurement of the ortho- to para-$D_2$ ratio fairly deviated from the established values[13][15]. I will discuss this discrepancy in terms of possible presence of a new relaxation mechanism no one has ever pointed out.

The theory of UCN production is described in Chapter 2. The theory of ortho/para conversion is given in Chapter 3. The development of UCN deuterium source at PSI and the measurement of SINQ deuterium moderator are given in Chapter 4. The experimental setup and procedure of KURRI are given in Chapter 5. In Chapter 6, we discuss the mechanism of the irradiation effect on the ortho to para conversion in comparison with the observed results and theoretical calculations on the microscopic and macroscopic basis. In particular, I will emphasize that a new mechanism which has not been discussed so far should be present to explain the observed conversion rate unexpectedly short. Finally, in Chapter 7, the summary of my work and the future outlook will be mentioned.

# Chapter 2 UCN source

In this chapter, a general view is presented on the various production methods and related topics of the ultra-cold neutrons (UCN).

UCN are produced by cooling neutrons by means of neutron moderators. The efficiencies of the moderators are given in Sec. 2.1. Though a Doppler shifter can increase an extraction efficiency of UCN from the moderators by converting cold neutron to UCN, it cannot increase the phase space density of neutron due to the restriction of Liouville's theorem. On the other hand, a new method called a "superthermal method" is expected to provide the UCN production rate beyond the thermal equilibrium value.

A basic principle of the superthermal method is described in Sec. 2.2. A subsequent subsection is devoted to description of the UCN source based on a solid $D_2$ ($sD_2$) which is one of the promising superthermal methods practically available or planned at some laboratories[10][11] in the world. The production efficiency of $SD_2$ UCN source is described in Sec. 2.3, and the design of UCN source at the PSI is written in Sec. 2.4.

## 2.1 UCN production by thermal equilibrium

Neutrons are produced by a reactor or spallation reaction with a few 100 MeV kinetic energy. Neutrons are losing their energies by elastic and inelastic scatterings in a moderator down to room temperature. If neutrons are enough moderated, i.e., thermalized, by the moderator, their energies disperse in accordance with the Maxwell-Boltzmann distribution at room temperature. The energy distribution per unit neutron flux is given by

$$\Phi(E)dE = \Phi_0 \frac{E}{(k_B T)^2} \exp\left(-\frac{E}{k_B T}\right) dE \tag{2.1}$$

where $\Phi_0$ is a flux of thermal neutrons, T is a temperature, $k_B$ is the Boltzmann constant. The UCN flux can be calculated by integration of eq. (2.1) in the energy range from 0 to $V_{UCN}$ which is an effective UCN potential. If we suppose that $V_{UCN}$ is 252 neV corresponding to the Be cut off[16] and T is 300 K, the UCN flux is given by

$$\Phi_{UCN} = \int_0^V \Phi(E)dE \cong \frac{V_{UCN}{}^2}{2(k_B T)^2} = 4.75 \times 10^{-11} \Phi_0 [n/cm^2/\mathrm{sec}] \tag{2.2}$$

assuming that $V_{UCN} \ll k_B T$. If neutrons are enough moderated (thermalized), they distribute with the same density in all phase space at low energy region ($E \ll k_B T$). A particle density in the phase space volume is kept constant in case of the conservative force field (Liouville's theorem). Therefore, the UCN density represents an inherent UCN intensity independent of their volume and velocity. Consequently, the UCN intensity is generally written in unit of density. The UCN density $\rho_{UCN}$ for the thermalized neutrons at 300 K is given by

$$\rho_{UCN} = \int_0^{V_{UCN}} \frac{\Phi(E)}{v} dE = \frac{2}{3} \Phi_0 \sqrt{\frac{m}{2}} \frac{V_{UCN}{}^{\frac{3}{2}}}{(k_B T)^2} = 9.1 \times 10^{-14} \Phi_0 [n/cm^3/\mathrm{sec}] \tag{2.3}$$

where v and m is a velocity and mass of neutron, respectively.

## 2.2 Superthermal method

The UCN density from the thermalized neutrons cannot achieve the value larger than $\rho_{UCN}$ given in eq. (2.3) as far as the conservative force field is concerned. However, R. Golub and J. M. Pendlebry suggested a possibility of the superthermal method in 1975[8], which enables highly enhancing the UCN density relative to the thermal distribution.

### 2.2.1 Principle of superthermal method

In this subsection, an outline of the superthermal method is described. This method uses a non-equilibrated process between two states, the idea of which was derived from the principle of the thermodynamics[18]. For simplicity, we consider the system consisting of two subsystems, A and A', each of which has two different energy states, r and s for A, and s' and r' for A', respectively. An interaction between A and A' subsystems will induce the change of their states if the energy conservation law

$$E_r + E_{r'} = E_s + E_{s'} \tag{2.4}$$

is satisfied. Here, $E_r$, $E_{r'}$, $E_s$, and $E_{s'}$ are the energy of state r, r', s, and s', respectively. In this case, we assume that the system A' is enough large not to be disturbed by the system A, and all the transitions of A are caused by the interaction with A', in other words, there is no self interaction in the system A.

As a next step, we contact A with the subsystem A'. The transition probability from the state ss' to rr', W(ss'→rr'), should have a symmetry relation given by

$$W(ss' \to rr') = W(rr' \to ss') \tag{2.5}$$

from the principle of the detailed balance. The Transition scheme is shown in Fig. 2.1.

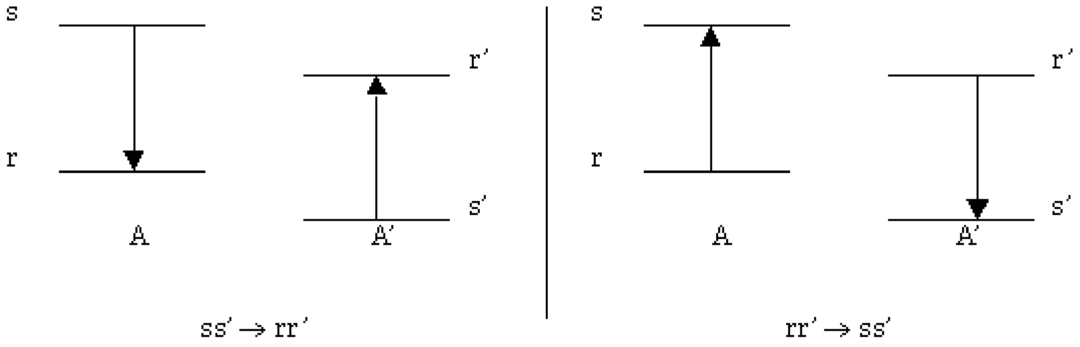

Fig. 2.1: Transition scheme; ss' to rr' is shown in the left, ss' to rr' is shown in the right.

On the other hand, when the two transitions, ss'→rr' and rr'→ss', are equilibrated, the equation

$$p_r p_{r'} W(ss' \to rr') = p_s p_{s'} W(rr' \to ss') \tag{2.6}$$

must be satisfied, where $p_r$ and $p_s$ are the probabilities taht A is in r or s, $p_r$' and $p_s$' are the probabilities A' is in r' or s'. Using eq. (2.5), we can get the following relation between the probabilities of

$$\frac{p_r}{p_s} = \frac{p_{s'}}{p_{r'}} \tag{2.7}$$

Because the A' is always equilibrium at temperature T, the $p_{r'}$ and $p_{s'}$ are given by the canonical distribution as

$$\frac{p_{s'}}{p_{r'}} = \frac{e^{-\beta E_{s'}}}{e^{-\beta E_{r'}}} = e^{-\beta(E_{s'}-E_{r'})} \tag{2.8}$$

where $\beta = k_B T$.

By using (2.4) and (2.7), we can get

$$\frac{p_r}{p_s} = \frac{e^{-\beta E_r}}{e^{-\beta E_s}} = e^{-\beta(E_r-E_s)} \tag{2.9}$$

as the enhancement.

On this model, we discuss about cooling of neutrons. First, the two states, the state 1 for cold neutron and the state 2 for UCN, are defined. The UCN density $\rho_2$ can be written by using the production rate, P, as.

$$\frac{d\rho_2}{dt} = P(1 \to 2) - P(2 \to 1) \tag{2.10}$$

where P is written as $N\Sigma\phi$, where N is the number of the target nuclei, $\Sigma$ is the cross section, and $\phi$ is the flux. Assuming the neutron velocity, v, eq. (2.10) can be written as

$$\frac{d\rho_2}{dt} = N\Sigma(1 \to 2)\phi_1 - N\Sigma(2 \to 1)\rho_2 v_2 \tag{2.11}$$

This can be easily solved, and the solution for $\rho_2$ is given by

$$\rho_2 = P \times \tau \exp\left(-\frac{t}{\tau}\right) \tag{2.12}$$

where

$$P = P(1 \to 2) = N\Sigma(1 \to 2)\phi_1 \tag{2.13}$$

and

$$\tau = \frac{1}{N\Sigma(2 \to 1)v_2} \tag{2.14}$$

Here, when we write the cross section for changing of neutron from Cold to UCN, $\Sigma(1\rightarrow2)$ and vise versa as

$$\Sigma(1 \rightarrow 2) = p_{1'}\sigma(1 \rightarrow 2) \tag{2.15}$$

and

$$\Sigma(2 \rightarrow 1) = p_{2'}\sigma(2 \rightarrow 1) \tag{2.16}$$

where the $p_{1'}$ and $p_{2'}$ are the probability that the phonon states of medium are in the ground state or excited states. The detailed balance gives the equation expressed by

$$\frac{k_1}{k_2}\sigma(1 \rightarrow 2) = \frac{k_2}{k_1}\sigma(2 \rightarrow 1) \tag{2.17}$$

where $k_1$ and $k_2$ are the wave number of cold neutron and UCN respectively. According to eq. (2.8), the ratio of $p_{1'}$ to $p_{2'}$ is given by

$$\frac{p_{1'}}{p_{2'}} = \frac{e^{-\beta E_1}}{e^{-\beta E_2}} = e^{-\beta(E_2 - E_1)} \tag{2.18}$$

Thus, $\rho_{UCN}$ at the steady state is given from eqs. (2.12) and (2.18) as

$$\rho_2 = \frac{\phi_1}{v_2}\left(\frac{k_2}{k_1}\right)^2 e^{\beta(E_1 - E_2)} = \frac{\phi_1}{v_2}\frac{E_2}{E_1}e^{(E_1 - E_2)/k_B T} \tag{2.19}$$

Then, $\rho_1 = \dfrac{\phi_1}{v_1}$, $\rho_2$ is enhanced as shown by

$$\frac{\rho_2}{\rho_1} = \frac{\dfrac{\phi_1}{v_2}\left(\dfrac{v_2}{v_1}\right)^2 e^{\beta(E_1 - E_2)}}{\dfrac{\phi_1}{v_1}} = \sqrt{\frac{E_2}{E_1}}e^{(E_1 - E_2)/k_B T} \tag{2.20}$$

If we adopt a larger $E_1$ and small T, we can enhance $\rho_2$ relative to $\rho_1$ as shown in eq.(2.20). In consequence, this is called the superthermal method.

As described in eq.(2.12), the UCN density $\rho$ at the steady state resulting from the superthermal method is given by

$$\rho = P \times \tau \tag{2.21}$$

where P is the production rate per second in a unit volume, and $\tau$ is storage time of UCN in the converter.

According to eq. (2.18), the probability, $p_1$ that phonons are in excited state, $p_1$, is small, and most of phonons are in the ground state at low temperature ($p_2 \sim 1$).

The down-scattering probability is proportional to $p_1$, and the up scattering probability is proportional to $p_2$. Thus, the up scattering probability is exponentially increases with temperature, while the down-scattering probability is almost independent in temperature. Accordingly, the production rate, P, is independent of temperature, and P is depends only on the scattering medium. This will be discussed in next section.

If there is no UCN loss except the up-scattering, the UCN density $\rho_2$ can be written as eq.(2.19). However, there are practically many loss components.

Since the inverse of total lifetime $\tau$ is given by the sum of inverse of all lifetime components that cause the UCN losses, namely,

$$\frac{1}{\tau} = \sum_i \frac{1}{\tau_i} \tag{2.22}$$

The main components of the UCN losses are an up-scattering and absorption of the UCN converter. The loss due to up-scattering can be reduced by decreasing the temperature of the converter, while the absorption cross section has a specific value for each nucleus, and is usually proportional to the inverse of neutron velocity. Thus, the UCN absorption is 400 times larger than the thermal neutrons. However, the neutron lifetime in a medium is kept irrespectively of velocity.

As a further loss of neutron, the loss by the wall collisions and escape from the storage bottle should be considered. Though the loss rate by the wall collision due to tunneling effect of neutron capture is estimated to be about $10^{-5}$ per bounce theoretically[16], whereas the observed lifetime is practically ~ 230 sec[19]. Needless to say, if ideally no loss exists, the lifetime is determined only by the neutron lifetime of $\beta$ decay, i.e., 885.4 sec[3].

### 2.2.2 Candidates of superthermal UCN source

As discussed in the preceding section, the material that has a large P and long $\tau$ can work as a favorable superthermal UCN converter. For this purpose, Liu[17] recommends items for necessary materials as superthermal as shown by

1) Large scattering cross section

The energy transfer from cold neutron to the superthermal material is caused by neutron scattering. Thus, the larger cross section can induce the large production. Here, the scattering cross section we mention is the cross section in boundary.

2) Small neutron absorption

The neutron absorption should be small to increase the UCN lifetime in the medium. The absorption cross section is accounted for as the inverse of lifetime.

3) Light mass

The phonon creation cross section is proportional to the inverse of mass of nucleus. Therefore, the material should be light nuclei.

From the above reasons, we suggest three materials, ortho-$D_2$, superfluid He and $\alpha$-$^{16}O_2$, as candidates suitable for superthermal UCN source. The characteristics of these materials for UCN source are listed in Table 2.1. These value were referred from ref.[17]. These densities are $3\times10^2$~$9\times10^4$ times larger than the values derived from eq. (2.3).

| Material | Solid ortho-$D_2$ | Superfluid $^4$He | $\alpha$-$^{16}O_2$ |
|---|---|---|---|
| Interaction | Phonon | Phonon | Magnon |
| Temperature of material | 5 K | 0.7 K | 2 K |
| Optimal neutron temperature | 29 K | 9 K | 12 K |
| Ideal lifetime | 146 msec | 886 sec | 750 msec |
| Production rate with 30 K neutrons | $1.0\times10^{-8}\Phi_0$ /cm$^3$/s | $2.3\times10^{-10}\Phi_0$ /cm$^3$/s | $1.1\times10^{-8}\Phi_0$ /cm$^3$/s |
| UCN density with with 30 K neutrons | $1.5\times10^{-9}\Phi_0$ /cm$^3$ | $2.1\times10^{-7}\Phi_0$ /cm$^3$ | $7.5\times10^{-9}\Phi_0$ /cm$^3$ |

Table 2.1: Characteristics of candidates suitable for superthermal sources. The values were referred from ref. [16] and [17]. $V_{UCN}$=252neV was used.

As shown in Table 2.1, the material that creates UCN density close to the ideal condition is superfluid $^4$He. This is because $^4$He has no neutron absorption cross section. However, $^4$He is very sensitive to the up-scattering and it has to be cooled down to less than 1.0 K. On the other hand, if the temperature of $^4$He increases to 1.2 K, the lifetime decreases to 30 sec due to the up-scattering [9]. Since the UCN source must be installed under the influence of the high radiation field where the dose rate is sometimes amounts to 100 W/kg. In such a case, the superfluid $^4$He method has a difficulty in the radiation problem.

On the other hands, the solid-$D_2$ can work at relatively high temperature, for example at 5 K, and the up-scattering effect due to the temperature increase is modest compared with the $^4$He case. This is because of the difference in the Debye temperature, 110 K for $D_2$ and 20 K for $^4$He. Accordingly, it is found that use of s$D_2$ has an important technological merit. In addition to this merit, s$D_2$ has 50 times larger production rate as compared with the He case, which means that s$D_2$ can produce 50 times larger flux per the same volume, and achieve the maximum density 50 times faster as shown in Table 2.1 50times faster. This characteristic behavior is an advantage for the UCN facility like SUNS[11].

## 2.3 Solid $D_2$ UCN converter

In this section, the property of UCN converter using the s-$D_2$ is discussed. The neutron down scattering process by the solid $D_2$ is given in ref. [20] and [17].

### 2.3.1 Production rate of UCN in s$D_2$

The down scattering by phonon is discussed in this subsection. The production rate can be written as

$$P = \int_0^{V_{UCN}} \int_0^{\infty} \Sigma(E_0 \to E_{UCN}) \Phi(E_0) dE_0 dE_{UCN} \tag{2.23}$$

According to ref. [20], $\Sigma(E_0 \to E_{UCN})$ is calculated by the incoherent approximation as

$$\begin{aligned}\Sigma(E_0 \to E_{UCN}) = \sigma_0 \frac{\tau}{2E_0} \frac{G(|\varepsilon|)}{\left(\varepsilon(1-e^{-\varepsilon/k_B T})\right)} e^{-\frac{(E_0+E)}{\mu\tau}} \\ \times \left[ (E_0 + E_{UCN} + \mu\tau) Sh\left(\frac{2\sqrt{E_0 E_{UCN}}}{\mu\tau}\right) - 2\sqrt{E_0 E_{UCN}} Ch\left(\frac{2\sqrt{E_0 E_{UCN}}}{\mu\tau}\right) \right]\end{aligned} \tag{2.24}$$

where

$$\tau = \frac{\hbar^2}{2M\gamma} \tag{2.25}$$

and

$$\gamma = \frac{\hbar^2}{2M}\int_0^\infty \frac{1}{\varepsilon} Coth\left(\frac{\varepsilon}{2k_B T}\right) G(\varepsilon) d\varepsilon \tag{2.26}$$

where ε=$E_0$-$E_{UCN}$, M is the nuclear mass, and μ is the M divided by the neutron mass. G(ε) is the phonon state density. If we assume that the crystal has no specific direction, then, the phonon state density, which was measured in ref. [21] and evaluated in ref.[20], is described by the Gaussian function as

$$G(\varepsilon) = \sum_{i=1}^{N} B_i e^{-a_i^2(\varepsilon-\varepsilon_i)^2} \tag{2.27}$$

which satisfies

$$\int_0^\infty G(\varepsilon) d\varepsilon = 1 \tag{2.28}$$

where ε denotes the neutron energy transfer. The incident neutron with energy the $E_0$ deposits most of its energy to a phonon and is converted to UCN with the remaining energy, $E_{UCN}$. These parameters are described in Table 2.2, and plotted in Fig. 2.2.

| I | $B_i$ ($meV^{-1}$) | $\varepsilon_I$ ($meV^{-1}$) | $a_i$ ($meV^{-1}$) |
|---|---|---|---|
| 1 | 0.195 | 5.08 | 3.700 |
| 2 | 0.135 | 5.50 | 0.530 |
| 3 | 0.095 | 7.40 | 0.640 |
| 4 | 0.300 | 9.05 | 2.666 |

Table 2.2: Values of the Gaussian parameters obtained by fitted the phonon spectrum [20]

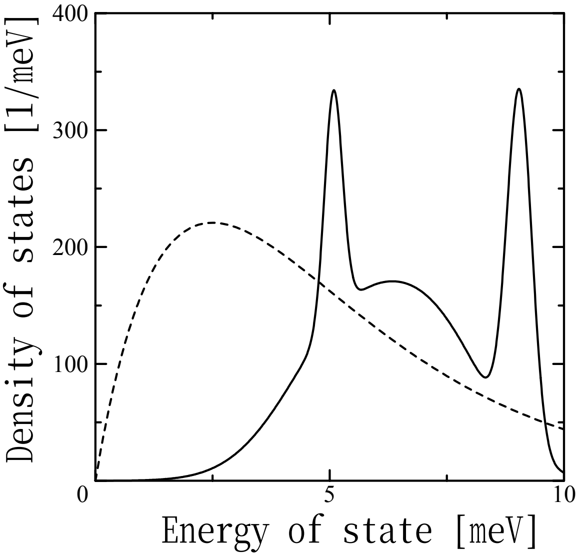

Fig. 2.2: The phonon state density for $sD_2$ evaluated by assuming the Gaussian functions[20]. The dashed line is the Boltzmann distribution of neutron flux with temperature of 29K.

From eq. (2.23), P is given by

$$P=1.0\times10^{-8}\Phi_0(30\ \mathrm{K})\ \mathrm{UCN/cm^3/s} \tag{2.29}$$

for the 30-K cold neutron and

$$P=7.9\times10^{-10}\Phi_0(300\ \mathrm{K})\ \mathrm{UCN/cm^3/s} \tag{2.30}$$

for the 300-K thermal neutron. It is found that the 29-K neutron makes P maximum.

### 2.3.2 Up scattering of UCN in $sD_2$

The up-scattering cross section of the UCN in the solid $D_2$ was calculated by Liu et.al.[12], The result of their calculation is shown in Fig. 2.3, where the UCN energy is assumed to be 335 neV the cut-off energy of $^{58}$Ni. The solid and dotted curves are the one-phonon annihilation cross section of the ortho- and para-$D_2$, and the red curve is the UCN up-scattering involving the para to ortho conversion. These inelastic cross sections were calculated assuming the incoherent approximation, and the cross sections follow the velocity inverse law. The noteworthy point is that the up-scattering cross section caused by the para to ortho conversion is extremely larger than other two one-phonon annihilation cross section. In addition, the cross section is temperature independent because the larger energy transfer to the UCN by the para to ortho conversion in $D_2$, 7 meV, makes neutron phase space larger than that given by the temperature. The up-scattering by the para to ortho conversion is 31 barn, which is about 100 times larger than the inelastic cross section of the ortho-$D_2$ at 5 K. The large up-scattering cross section gives the UCN lifetime of 4.6 msec for a normal-$D_2$ (2/3 ortho and 1/3 para-$D_2$) with the density of $3.0\times10^{22}$ $cm^{-3}$.

On the other hands, such conversion involving the up-scattering doesn't occur in the pure ortho-$D_2$ because of the energy conservation. Accordingly, the para-$D_2$ has to be eliminated as much as possible for the high intensity UCN source. If an ideally pure ortho-$D_2$ is used for the UCN source, the up-scattering is negligibly small at 4 K, then, the UCN lifetime is determined only by the neutron absorption by deuterons. Using the cross section determined by deuteron absorption the lifetime is estimated to be 146 ms.

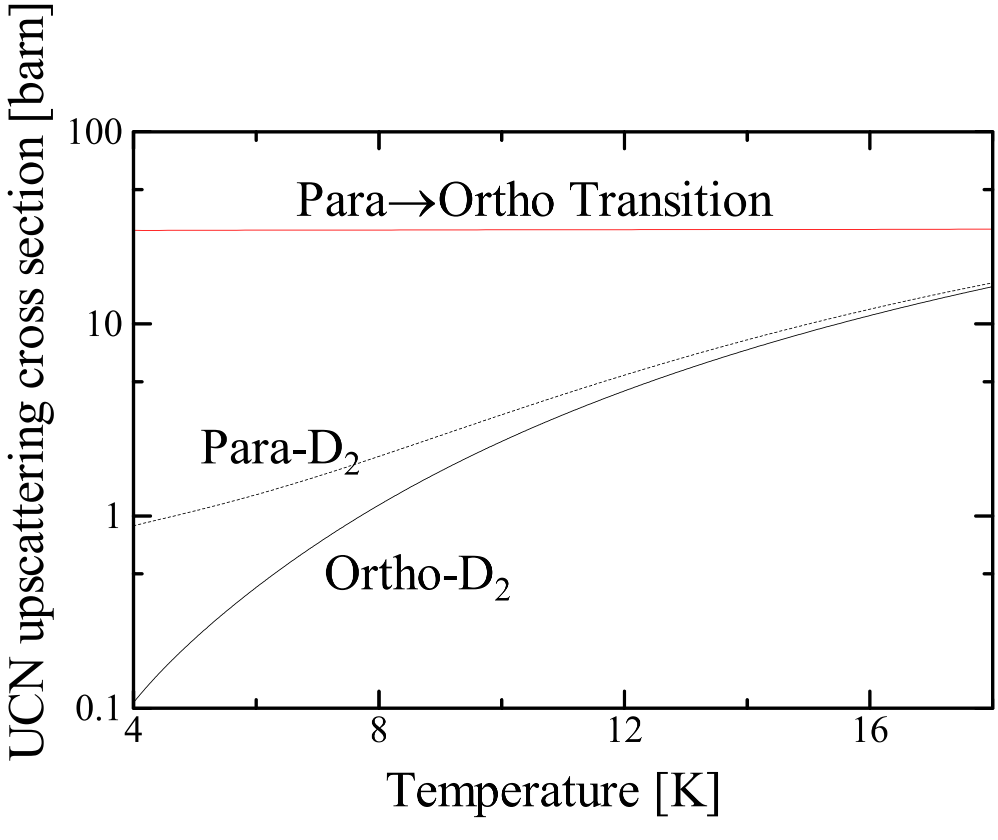

Fig. 2.3: UCN up-scattering cross section in solid $D_2$[12]. The neutron energy used in this calculation is $^{58}$Ni cut off, 335 neV.

### 2.3.3 The lifetime and UCN density

As discussed in Sec. 2.3.2, the UCN lifetime in the solid-$D_2$ varies from 4.6 ms to 146 ms according as the ortho fraction varies from 66.7% to 100%, and the lifetime is independent of the UCN energy because the cross section follows the inverse of the velocity. Practically, the equilibrium ortho fraction at triple point, 18.6 K, gives the ortho fraction of 98.5%. With this ortho fraction, the calculated lifetime is 51 msec at 5 K. The temperature dependence of total lifetimes calculated by eq. (2.22) are shown in Fig. 2.4 for the $sD_2$ with different ortho fractions.

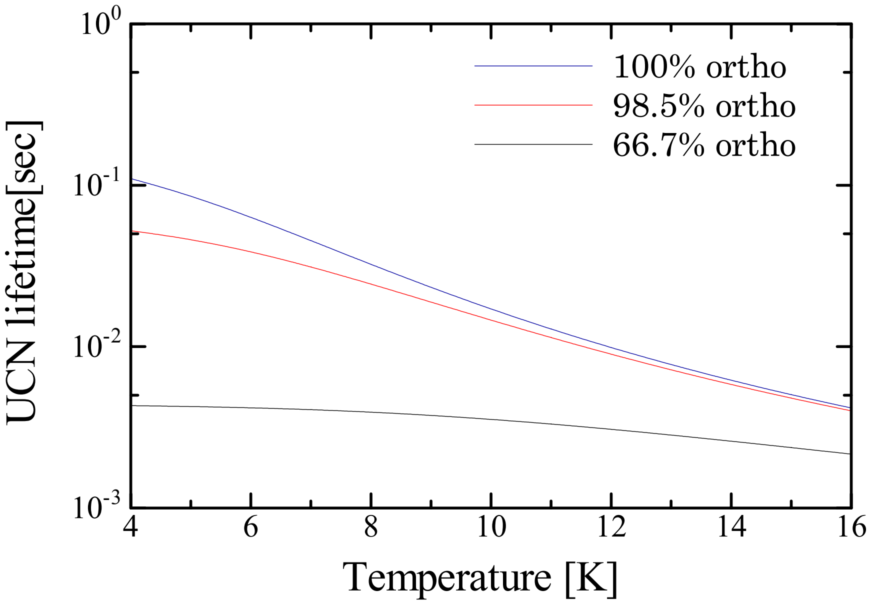

Fig. 2.4: The temperature dependence of the total lifetime for UCN in the $sD_2$ with the ortho fractions; 100%(blue), 98.5% and 66.7%.

The UCN density can be calculated by eq. (2.21). From the discussion of Sec. 2.3.1, the production rate P is given by eq. (2.29), and the P is independent of temperature. Thus, the UCN density provided by the solid-$D_2$ converter at 30 K with a neutron flux $\Phi_0$ /cm²/s is given by

$$\rho_{ucn} = 1.5\times10^{-9}\ \Phi_0(30\ \mathrm{K})\ \mathrm{UCN/cm^3} \tag{2.31}$$

for 100% ortho at enough low temperature (T<<4K), and

$$\rho_{ucn} = 5.0\times10^{-10}\ \Phi_0(30\ \mathrm{K})\ \mathrm{UCN/cm^3} \tag{2.32}$$

for 98.5% ortho at 5K.

## 2.4 UCN source at PSI

A scheme of the spallation UCN source (SUNS[11]) planned at PSI is shown in Fig. 2.5. A 590-MeV proton beam bombards a Lead/Tin alloy target to produce evaporated neutrons by the spallation reaction. The produced neutrons are cooled by the heavy water moderator down to room temperature. A solid deuterium converter is set in the moderator. The volume of solid deuterium converter is 27 liter. This solid deuterium converter works not only as a converter of the cold neutron to generate the UCN but also as a converter of the thermal neutron to generate the cold neutron. The produced UCN are stored in a storage vessel whose volume is about 2 $m^3$. The stored UCN are transported to the experimental hall through a UCN guide.

As discussed in Chapter 2, the $sD_2$ converter mixed with the ortho- and para-$D_2$ must be purified to the complete ortho-$D_2$ by converting the para-$D_2$ to ortho-$D_2$. The deuterium converter is exposed by a strong radiation from the spallation target. The power deposition in the deuterium converter is estimated as 72.7 mW/g with 1 mA proton beam[23]. The neutron flux is expected as $3.4\times10^{13}$ /$cm^2$/s/mA with the temperature about 33.6 K[23]. By using eq. (2.29), the UCN production rate can be estimated as

$$P=3.2\times10^{5}\ \mathrm{UCN/cm^3/s} \tag{2.33}$$

Using the practical lifetime 50 msec, which is expected by $sD_2$ with 98.5% ortho fraction at 5K, the density can be estimated as

$$\rho_{ucn} = 1.6\times10^{4}\ \mathrm{UCN/cm^3} \tag{2.34}$$

This source will be operated by pulsed beam. The irradiation period is planed as between 4 sec irradiation per 400sec and 8 sec irradiation per 800 sec. In both cases, the duty factor is 1/100, thus, the averaged dose will be 1/100 of 72.7 mW/g, 0.727mW/g.

The radiation makes the ortho-$D_2$ convert to the para-$D_2$ by the procedure as will be discussed in Sec. 3.3.3. The final results of the expected performance derived from our measurement is discussed in Sec. 6.4.

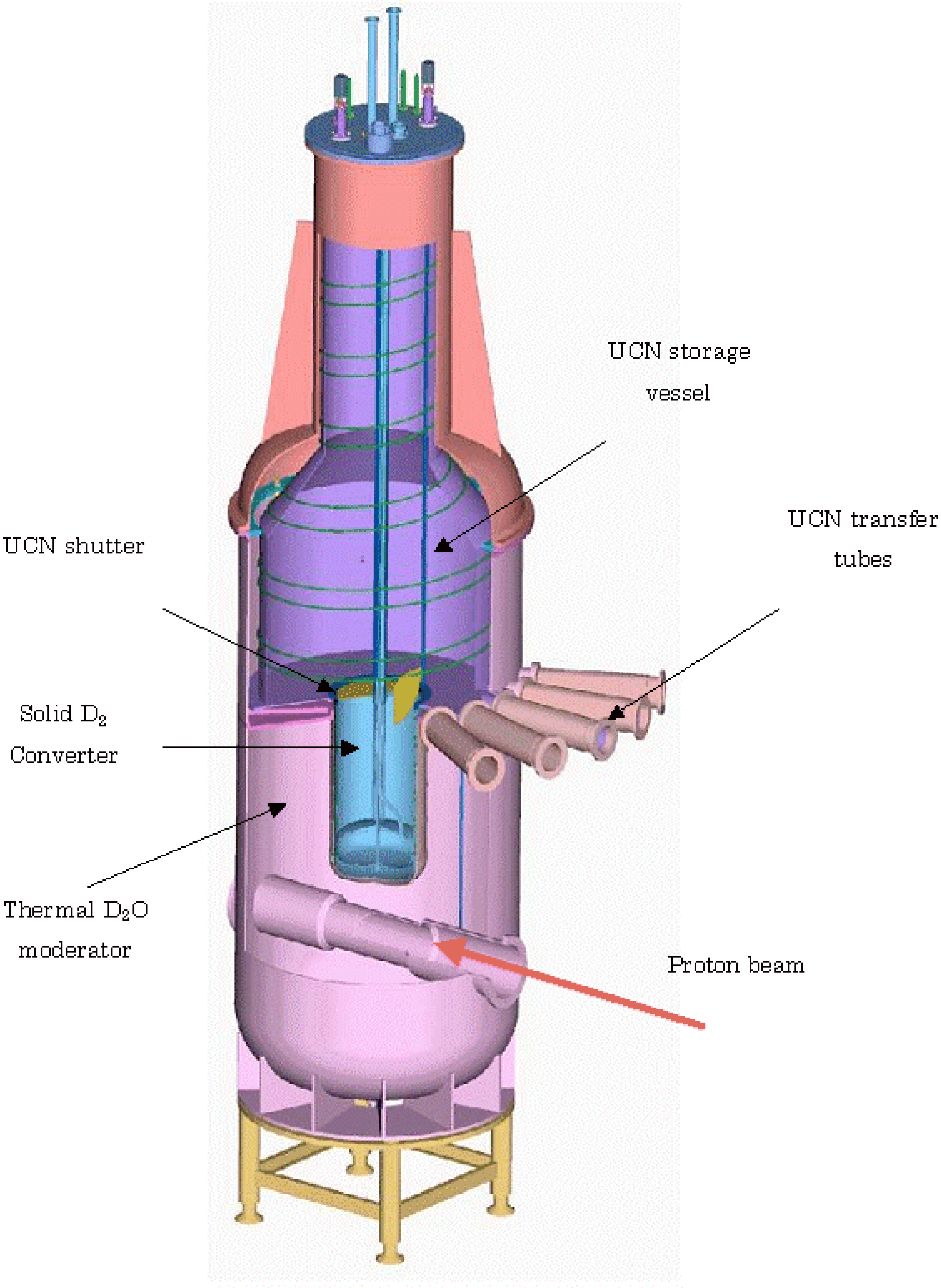

Fig. 2.5:A Schematic picture of SUNS[11].

# Chapter 3 Ortho/Para conversion of $D_2$

As described in Chapter 2, a solid $D_2$ is mentioned as a moderator suitable for the UCN sources. It is well known that $D_2$ in the ortho state (parallel nuclear spins) are effective in increasing the UCN density by the “down-scattering” process, while $D_2$ in the para state (anti-parallel nuclear spins) reduce the UCN density by the “up-scattering” process. These molecular states are physically associated with the symmetry property of the molecular wave functions.

A general view of the symmetry properties of the wave functions for the $D_2$ and other types of the hydrogen molecules is described in Sec. 3.1. In Sec. 3.2, thermal equilibrium values for the ortho/para ratio and the conversion rates from the ortho to para states at thermal equilibrium are discussed. In Sec. 3.3, an enhancement of ortho/para conversions with a catalyst and irradiation will be discussed in more detail because the latter effect is one of the central subjects of the present work. Finally, in Sec. 3.4, possible methods to measure the ortho/para ratio for the $D_2$ are mentioned, among which the method based on the Raman spectroscopy is that we used in the present work. The detail of the Raman spectroscopy is discussed in the later sections.

## 3.1 Ortho and Para state in diatomic molecules

The wave functions of homonuclear diatomic molecules such as $H_2$, $D_2$, and $T_2$ are expressed in view of the symmetry consideration with respect to the permutation of identical particles. In this case, molecular wave functions can be written as

$$\Psi_{tot} = \phi_{nuclei} \times \phi_{vibration} \times \phi_{rotation} \times \phi_{electron} \tag{3.1}$$

where $\Psi_{tot}$ is total wave functions of molecule, $\phi_{nuclei}$ is total wave function of nuclear spins, $\phi_{vibration}$ and $\phi_{rotation}$ are nuclear spatial wave functions of vibration and rotation, and $\phi_{electron}$ is electron spatial wave function.

$\Psi_{tot}$ must change its sign (antisymmetry) for exchange of fermions, and $\Psi_{tot}$ must not change its sign (symmetry) for exchange of bosons from the requirement of the quantum mechanics.

In Eq. (3.1), $\phi_{electron}$, which represents the spatial wave function of electrons, doesn't change its sign as far as the coupling of two electrons forms the singlet. $\phi_{vibration}$ is also symmetric irrespectively of exchange. The rotational wave function $\phi_{rotation}$ changes its sign depending on the rotational quantum number J as

$$\phi_{rotation} = (-1)^J \phi'_{rotation} \tag{3.2}$$

where $\phi'_{rotation}$ is exchanged wave function. Above equation means $\phi_{rotation}$ is symmetric if J is even, and antisymmetric if J is odd.

Accordingly, depending on the symmetry of nuclear wave function $\phi_{nuclei}$, J takes either odd or even, i.e., J takes even for the asymmetric nuclear wave function, and J takes odd for the symmetric nuclear wave function.

More specifically, this is given by the following relationship;

$$\Psi_{tot}(Fermion) = \phi_{vibration}\phi_{electron} \begin{cases} \phi_{rotation}(J = odd) \times \phi_{nuclei}(symmetry) \\ \phi_{rotation}(J = even) \times \phi_{nuclei}(antisymmetry) \end{cases} \tag{3.3}$$

and

$$\Psi_{tot}(Boson) = \phi_{vibration}\phi_{electron} \begin{cases} \phi_{rotation}(J = odd) \times \phi_{nuclei}(antisymmetry) \\ \phi_{rotation}(J = even) \times \phi_{nuclei}(symmetry) \end{cases} \tag{3.4}$$

We call the molecule with $\phi_{nuclei}$(symmetry) as "ortho" and $\phi_{nuclei}$(antisymmetry) as "para". For example, ortho $H_2$ is a state with J=odd, and ortho $D_2$ with J=even. Since the ground state of the rotational band for hydrogen isotopes ($H_2$, $D_2$, and $T_2$) has J=0, only para $H_2$, para $T_2$ and ortho $D_2$ are allowed to exist as the molecular ground state. The above mentioned ortho and para states can be regarded as different molecules each other. In fact, the conversion from the ortho to para states or vice versa are very slow under the normal condition.

The abundance of the symmetric component relative to the antisymmetric component is obtained from the statistical weight as discussed in Appendix A. This result is given in (A.10) as

$$\frac{symmetry}{antisymmetry} = \frac{(I+1)}{I} \tag{3.5}$$

where I is the nuclear spin.

Let us continue the discussion on the heteronuclear diatomic molecules like HD. Because the HD consists of two different nuclei, the HD states having J with even and odd J can exist for all the possible I. In case of $^{16}O_2$, the symmetry property of the total wave function becomes somehow complicated. Since the $^{16}O$ nucleus has a spin 0, the total nuclear spin I of $^{16}O_2$ is 0, and $\phi_{nuclei}$ is symmetric, which means that the only ortho $^{16}O_2$ state is allowed to exist. Because the $^{16}O$ nucleus is a boson, $\Psi_{tot}$ must be symmetric for exchange. Here, we have to think about the symmetry of $\phi_{electron}$. Since the electron spins of the $O_2$ ground state ($^3\Sigma^-_g$) couple not anti-parallel but parallel, $\phi_{electron}$ of $O_2$ is symmetric for exchange. Finally, $\phi_{rotation}$ allows only J=odd state.

## 3.2 Thermal equilibrium value of ortho and para molecules

As discussed in the previous section, the homonuclear diatomic molecules have $J_{even}$ or $J_{odd}$ rotational states corresponding to the symmetry property of nuclear wave functions. The energy of the rotational state with $J^{th}$, $E_J$ for the molecular hydrogen is given in Appendix B. At room temperature, the populated excited states are restricted to the rotational state with the lowest vibrational state because the energy of the excited vibrational states are too high to be populated.

When the molecular hydrogen is thermally populated in the excited rotational band in accordance with the Boltzmann distribution, the population of the $E_J$ state P(J) is given by

$$P(J) = (2J+1)\exp(-E_J / k_B T) \tag{3.6}$$

where $k_B$ is the Boltzmann constant and T is the temperature. $E_J$ of $D_2$ molecule is given in Appendix B.

The populated fraction in $J^{th}$ state, N(J), is given by

$$N(J) = \frac{Q(J)P(J)}{\sum_J Q(J)P(J)} \tag{3.7}$$

where Q(J) is nuclear spin degeneracy with $J^{th}$ rotational state allowed by selection rule discussed in former section. The Q(J) takes only two value, $Q_o$ and $Q_p$. In case that rotational state allows only symmetric nuclear spin, the $Q(J)=Q_o$, and $Q(J)=Q_p$ in opposite case. Because symmetric rotational state requires $D_2$ to have symmetric nuclear spin state, the Q(J) is given by

$$Q(J) = \begin{cases} Q_o & J = even \\ Q_p & J = odd \end{cases} \tag{3.8}$$

where

$$Q_o = \sum_{I=symmetry} g(I) = \sum_{I=0,2} g(I) \tag{3.9}$$

$$Q_P = \sum_{I=antisymmetry} g(I) = \sum_{I=1} g(I) \tag{3.10}$$

where g(I) is the degeneracy of a nuclear spin, I, and is given by

$$g(I) = (2I+1) \tag{3.11}$$

The nuclear spin I of deuteron is 1, $Q_o$, $Q_p$ and Q is 6 and 3 respectively.

In case of $D_2$ molecule, the molar fractions of the ortho, $c_o$, and para, $c_p$, are respectively given by

$$c_o = \frac{\sum_{J=0,2,4...} Q_o P(J)}{\sum_J Q(J)P(J)} \tag{3.12}$$

$$c_p = \frac{\sum_{J=1,3,5...} Q_p P(J)}{\sum_J Q(J)P(J)} \tag{3.13}$$

See Appendix A for detailed discussion of nuclear degeneracy. Because of its definition, $c_o+c_p=1$.

At the high temperature limit ($T>>E_1$),

$$\sum_{J=0,2,4...} P(J) \cong \sum_{J=1,3,5...} P(J) \tag{3.14}$$

is approximately correct. Therefore, ortho and para ratio is approximated expressed by $Q_o : Q_p$. For example, a total nuclear spin of the hydrogen molecule can take either I=1 or 0. The hydrogen with I=1 has a symmetric nuclear wave function, and I=0 has antisymmetric one. From (3.11), g(0) and g(1) are 1 and 3 respectively. Therefore, the ratio of the ortho to para hydrogen $Q_o$:$Q_p$ is 1:3 at high temperature limit.

On the other hand, in case of the deuterium, the deuterium has I=0,1, and 2. Then, $g(I_{ortho}) : g(I_{para})$ is given by g(0)+g(2) : g(1) = 6 : 3 by using eqs. (3.12) and (3.13). As a result, the equilibrium ortho fraction $C_o$ at room temperature (300 K) is 66.67%, which is the value given as the high temperature limit. The molecules that have equilibrated ortho-para ratio corresponding to high temperature limit are called as "normal molecular hydrogen".

On the other hand, at low temperature ($E_1 >> T$), we can neglect terms with J≥2 because P(2) is negligibly small. Therefore, by using (3.12) and (3.13), $C_p$ is approximated by

$$c_p \cong \frac{Q_p P(1)}{Q_o P(0)} = \frac{3 \times (2 \times 1 + 1) \exp(-E_1 / k_B T)}{6} = \frac{3}{2} \exp\left( -\frac{E_1}{k_B T} \right) \tag{3.15}$$

The energy of the first exited state $E_1$ for the deuterium is 7.41 meV corresponding to 86K. Using E1 derived in Appendix **B** the temperature dependence, the para ratio $C_p$ was obtained as shown in Fig. 3.1. It is noted that equilibrium $c_p$ is 1.48% at the triple point of $D_2$ (T=18.69 K).

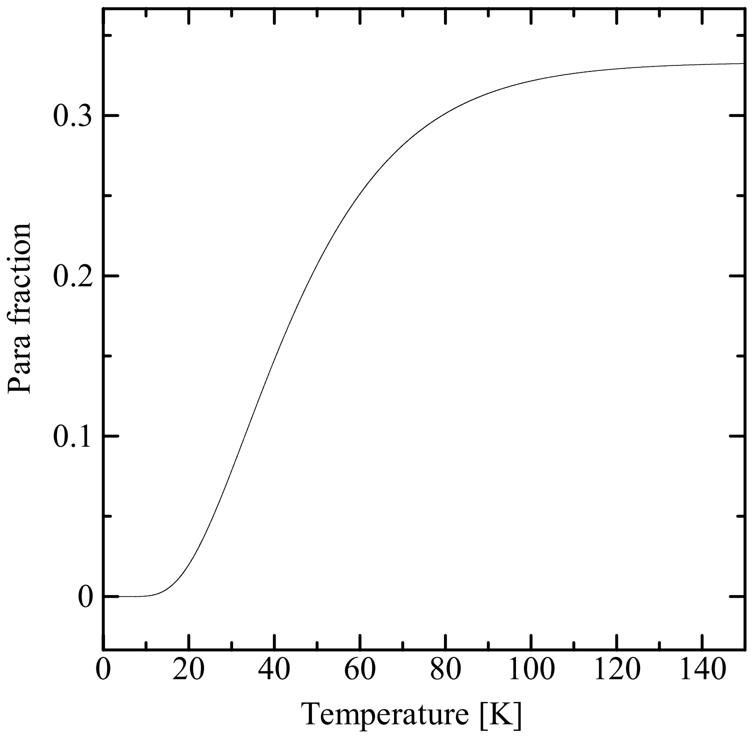

Fig. 3.1: Temperature dependence of equilibrium fraction of the para deuterium $c_p$. The para fraction asymptotically increases up to 2/3 with temperature.

## 3.3 Ortho/Para conversion

In this subsection, the theory of ortho/para conversion is discussed.

### 3.3.1 Conversion by spontaneous relaxation

The rotational quantum number J can easily change by collision with other molecules or by absorption and emission of light. However, the total nuclear spin I can hardly change the direction because of smallness of the nuclear magnetic moment compared to the atomic ones. In other words, with a pure deuterium sample, conversion between ortho and para hardly occurs even the ortho and para ratio is not equilibrated. Because orbital electrons have anti-parallel spins and their magnetic moments are canceled each other, only the dipole-dipole interaction with the nuclear magnetic moment of other molecules or the quadrupole-quadrupole interaction between the nuclear quadrupole moment and electric field gradient produced by the molecules can cause the ortho-para conversion. The self-conversion rate at temperature T is given by

$$\frac{dc_p}{dt} = -K_{nat} c_o^{\ 2} - K'_{nat}\, c_o (1 - c_o) \tag{3.16}$$

in ref. [26][15]. The $K_{nat}$ and $K'_{nat}$ are the rate constant in (mol fraction·s)$^{-1}$. From ref. [13], (3.16) is extended as a function of temperature T as

$$\frac{dc_o}{dt} = -K_{nat} c_o^{\ eq}(T) c_o^{\ 2} - K'_{nat}\, c_o^{\ eq}(T) c_o (1 - c_o) \tag{3.17}$$

where the $c_o^{eq}(T)$ is equilibrium fraction of ortho-$D_2$ with temperature T given by (3.12). Experimentally and theoretically, the rate constant $K_{nat}$ and $K'_{nat}$ are almost equal [26] Therefore, it is described by

$$K_{nat} \cong K'_{nat} \tag{3.18}$$

By using (3.17) and (3.18), (3.17) is approximately written as

$$\frac{dc_o}{dt} = K'_{nat}\, c_o^{\ eq}(T) c_o \tag{3.19}$$

This equation gives exponential solution. From reference[22][27], K' is $3.2 \times 10^{-4}$ hour$^{-1}$, which corresponds to the lifetime of 129 days for a liquid deuterium at 20.4 K. Because of this slow conversion rate, the ortho and para molecules can be regarded as different molecules in a short period.

## 3.3.2 Conversion by catalyst

As described in the former section, it is not easy to convert the para deuterium to the ortho deuterium in a short time only by cooling the pure deuterium sample down to the freezing point. To overcome this difficulty, a catalyst is usually used to equilibrate the ortho/para ratio. In general, materials with paramagnetism such as $Fe(OH)_3$, $CrO_3$, and $MnO_2$ are suitable for catalysts, since the large electron magnetic moment can induce the spin-flip of the deuteron. The conversion rate (especially para to ortho conversion) is proportional to a contacting surface area of the catalyst and the deuterium, which is given by

$$\frac{dc_o}{dt} = \beta_{cat} A \tag{3.20}$$

where $\beta_{cat}$ is rate constant of conversion by catalyst, A is surface area of catalyst. Typically, material with $\beta_{cat} > 10^{-6}$ mol/m$^2$/s works as catalyst. The conversion rate is independent of the para fraction until it becomes small[22][25]. This behavior causes the selective conversion of the para deuterium to the ortho deuterium on the catalytic surface. If diffusion speed is enough slow compared to the conversion time as in case of the solid deuterium, or if the para fraction is so small that the total deuterium volume might be insufficient to contact with the catalyst, then the time dependence of the conversion rate has an exponential function.

A molecular oxygen is also known as a catalyst because it is a paramagnetic molecule with the spins of outermost electrons are parallel. The conversion probability by dipole-dipole reaction, $P_{dip}$, is given by

$$P_{dip} \propto V\left[\begin{pmatrix} magnetic \\ dipole \end{pmatrix}\right]^2 \cong \left(\frac{\mu_0}{4\pi}\frac{\mu_i \mu_j}{r^3}\right)^2 \tag{3.21}$$

where $\mu_0/4\pi=10^{-7}$ N/A, $\mu_i$ and $\mu_j$ is magnetic moment, r is the distance between the two dipoles. The magnetic moment of the proton, deuteron, and electron are 14.1 4.33, $9284\times10^{-27}$ J/T, respectively[28]. Therefore an oxygen molecule induces the conversion with $1.8\times10^7$ times larger probability than a deuteron.

The catalytic conversion by molecular oxygen in a first order process is given by

$$\frac{d[D_2{}^o]}{dt} = \beta_{ox} c_o{}^{eq}(T)[O_2][D_2{}^p] - \beta_{ox}\left(1 - c_o{}^{eq}(T)\right)[O_2][D_2{}^o] \tag{3.22}$$

where $\beta_{ox}$ and $\beta'_{ox}$ are rate constant of catalytic conversion by oxygen, $c_o^{eq}(T)$ is equilibrium fraction of ortho-$D_2$ with temperature T. The $[D_2^p]$, $[D_2^o]$ and $[O_2]$ are molar fraction in medium. From ref.[29], $\beta_{ox}$ for catalyzing $H_2$ is given by

$$\beta_{ox}(H_2)=1.15 \pm 0.08\ \mathrm{s}^{-1} \tag{3.23}$$

as high temperature limit (above 8K). By using eq.(3.21), the $\beta_{ox}(D_2)$ may be estimated as about $(1/3)^2$ of eq.(3.23). However, the smaller conversion energy from J=1 state (para) to J=0 state (ortho), which corresponds half of conversion of hydrogen, is more easily to be absorbed by its phonon state[22]. Comparing to the self-catalyzing of liquid hydrogen and deuterium[22], the enhancement by smaller energy is estimated as 7.3 times. Thus we finally estimate the $\beta_{ox}(D_2)$ as

$$\beta_{ox}(D_2)=0.791\ \mathrm{s}^{-1} \tag{3.24}$$

### 3.3.3 Radiation induced conversion

Since the UCN source based on the solid deuterium is located close to the target on which the accelerated proton beam is bombarded, the solid deuterium is exposed by the strong radiation. The radiation must give rise to the conversion of ortho to para deuterium, which eventually deteriorates the performance of the solid deuterium to produce the UCN. In this section, we discuss the radiation-induced conversion from both the experimental and theoretical aspects.

Let us introduce one of the well-established conversion models in ref.[15] and [13] for easier discussion below. In this model, firstly, the radiation produces ions, electrons, or both of them by the collisions with the deuterium target. The produced ions and electrons are losing their kinetic energy by the collisions of electrons of the target molecules. The excited molecules, then, form the molecular ions, such as $D^+$ or $D_2^+$. Thereafter, these molecular ions produce the free atoms by dissociation and neutralization. The free atoms drift in the medium (target deuterium) until the free atom finds other free atom and again forms a $D_2$ molecule by recombination. The recombination energy for $D_2$ is 4.5 eV [30]. The release of this energy to the recombined $D_2$ makes it be in the high temperature. As a result, it is easily understood that ortho/para ratio for the recombined $D_2$ should be 2:1, which is the equilibrium ratio at the high temperature limit. These processes are expressed by

$$\left.\begin{array}{l} D_2^{\,o} \xrightarrow[k]{} \\ D_2^{\,p} \xrightarrow[k]{} \end{array}\right\} 2D \left\{\begin{array}{l} \xrightarrow[2\alpha/3]{} D_2^{\,o} \\ \xrightarrow[\alpha/3]{} D_2^{\,p} \end{array}\right. \tag{3.25}$$

In the next, we think about the specific values for the parameters used in this model. Assuming that the breakup rate k of the $D_2$ is equal to the atom creation rate of the tritium gas, it is found that 5.1±0.3 atoms are created per one ion pair [31], and one ion pair is created per 36.6 eV energy loss of the electron with high energy (>100 keV) [32][33]. Hence, the molecular breaking up coefficient, k, can be estimated as

$$k = 2.89 \pm 0.20 \times 10^{-6}\, P \text{ g/J} \tag{3.26}$$

where P is radiation dose in unit of W/g.

On the other hand, the α represents the recombination rate of the free atoms. Because the recombined molecule creates the high temperature equilibrium state, 2/3 of the recombined molecules will be the ortho states, and other 1/3 will be the para states.

It is known that the free atoms (produced by radiation) work as a catalyst due to their unpaired electrons [15][34][35][36]. In other words, the free atoms change the ortho-para ratio to the equilibrium value as schematically shown by

$$\begin{aligned} D_2{}^p &\xrightarrow[\beta_{rad} c_o{}^{eq(T)}]{} D_2{}^p \\ D_2{}^o &\xrightarrow[\beta_{rad}\left(1-c_o{}^{eq(T)}\right)]{} D_2{}^o \end{aligned} \tag{3.27}$$

where $\beta_{rad}$ is the conversion rate by catalyzing of free atoms that leads the ortho fraction to equilibrium value. Because catalyzing rate by free atoms is proportional to mol fraction of D-atoms, [D], a differential equation for fraction of ortho-$D_2$ can be written as

$$\frac{d[D_2{}^o]}{dt} = \beta_{rad} c_o{}^{eq}(T)[D][D_2{}^p] - \beta_{rad}\left(1 - c_o{}^{eq}(T)\right)[D][D_2{}^o] \tag{3.28}$$

The former equation can be simplified as

$$\frac{d[D_2{}^o]}{dt} = \beta_{rad} c_o{}^{eq}(T)[D][D_2] - \beta_{rad}[D][D_2{}^o] \tag{3.29}$$

### 3.3.4 Time dependence of ortho fraction

As discussed in the former section, the differential equation of the ortho fraction is given as

$$\begin{aligned} \frac{d[D_2{}^o]}{dt} &= -\left(k + \beta_{rad}[D] + \beta_{nat}[D_2]\right)[D_2{}^o] \\ &\quad + c_o{}^{eq}(T)\left(\beta_{rad}[D] + \beta_{nat}[D_2]\right)[D_2] + \frac{2}{3}\alpha[D]^2 \end{aligned} \tag{3.30}$$

Then, [D] can be written by using k and α as

$$\frac{d[D]}{dt} = 2k[D_2] - 2\alpha[D]^2 \tag{3.31}$$

The former differential equation yields

$$[D] = \sqrt{\frac{k[D_2]}{\alpha}} \tanh\left(2\sqrt{k\alpha[D_2]}\,t\right) \tag{3.32}$$

as a function of time, t, when [D]=0 at t=0 is satisfied. The eq.(3.32) is asymptotically equal to

$$[D] = \sqrt{\frac{k[D_2]}{\alpha}} \tag{3.33}$$

Here we define a lifetime, $\tau_\alpha$, as

$$\tau_\alpha = \frac{1}{2\sqrt{k\alpha[D_2]}} \tag{3.34}$$

The $\alpha$ can be extrapolated as $1.19\times10^{-20}$ cm$^3$/s and $1.28\times10^{-13}$ cm$^3$/s at 10 K and 25 K[37], and if we assumed that the radiation dose was 100mW/g, k can be deduced from eq.(3.25) as $2.89\times10^{-7}$s$^{-1}$. Then, $\tau_\alpha$ can be calculated as 50 sec and 15 msec at 10 K and 25 K, respectively. These time scales are enough shorter than our scale, and the [D] value is always equilibrated. Therefore, if we define $\beta^*$ as

$$\beta^* = \beta_{rad}\sqrt{[D_2]/\alpha} \tag{3.35}$$

we can write eq.(3.33) as

$$\beta^*\sqrt{k} = \beta_{rad}[D] \tag{3.36}$$

By substituting eq.(3.36) into eq.(3.30), we can obtain

$$\begin{aligned}\frac{d[D_2{}^o]}{dt} &= -\left(k + \beta^*\sqrt{k} + \beta_{nat}[D_2]\right)[D_2{}^o] \\ &\quad + \left(c_o{}^{eq}(T)\left(\beta^*\sqrt{k} + \beta_{nat}[D_2]\right) + \frac{2}{3}k\right)[D_2]\end{aligned} \tag{3.37}$$

This differential equation can be easily calculated and the result is shown by

$$[D_2{}^o] = \left([D_2{}^o]_{t=0} - A[D_2]\right)\exp(-t/\tau) + A[D_2] \tag{3.38}$$

where

$$\tau = \frac{1}{k + \beta^*\sqrt{k} + \beta_{nat}[D_2]} \tag{3.39}$$

$$A = \tau\left(c_o{}^{eq}(T)\left(\beta^*\sqrt{k} + \beta_{nat}[D_2]\right) + \frac{2}{3}k\right) \tag{3.40}$$

$[D_2{}^o]_{t=0}$ is an initial value of $[D_2{}^o]$.

The molar ortho fraction, $c_o$, which can be written as

$$c_o(t) = \frac{[D_2{}^o]}{[D_2]} \tag{3.41}$$

is given by

$$c_o(t) = (c_o(t=0) - A)\exp(-t/\tau) + A \tag{3.42}$$

Thus, $c_o(t)$ follows an exponential function asymptotically closing to A which is defined in eq.(3.42) with a lifetime $\tau$ (eq.(3.39)).

## 3.4 Methods to measure ortho/para ratio

As discussed in Section 3.2, the ortho fraction varies from 0.67 to 1.0 with thermal equilibrium. In this section, we explain several ways to measure the ortho-para ratio.

### 3.4.1 Raman spectroscopy

The Raman spectroscopy is a method offered for the measurement of the molecular structure. This method uses an inelastic scattering and subsequent de-excitation of the laser light, usually called as Raman scattering. The spectrum taken by the Raman scattering gives us important information on the populations of molecular rotational states. The Raman spectrum of normal $D_2$ gas is shown in Fig. 3.2. The peaks named S(0), S(1)..., are correspond to the Raman scattering of state J=0 to J=2, J=1 to J=3, and so on. The intensity of peaks are given by the product of the population and the matrix element of J. Thus, the Raman spectrum can induce the information of ortho/para ratio and temperature. The detail of Raman spectroscopy is discussed in Appendix 7.1. The advantages of the Raman spectroscopy applied to measure the ortho-para ratio is to make it possible to measure ortho/para ratio absolutely. In this paper, Raman spectroscopy is only applied for gas sample, but Raman spectroscopy applied to solid state gives us information of crystal structure[38].

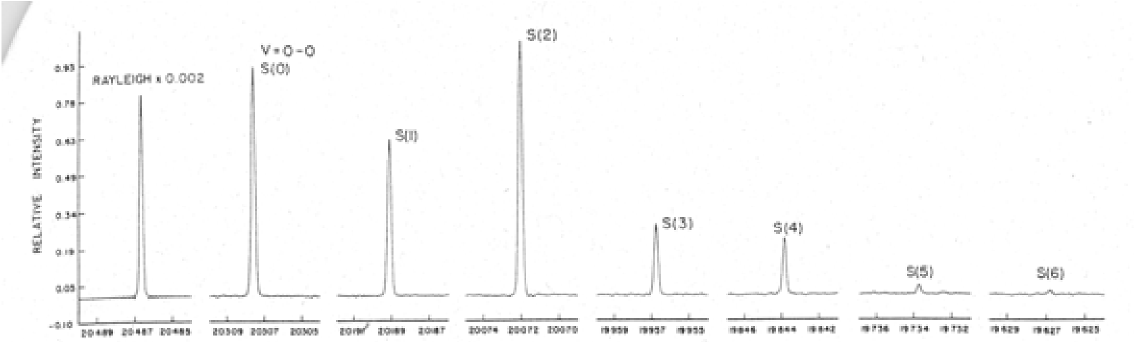

Fig. 3.2: An example of the Raman spectrum applied to measure the rotational band of $D_2$[39].

## 3.4.2 Thermal conductivity

A measurement of the thermal conductivity also can give us the information of ortho/para ratio because of difference of thermal conductivity between ortho and para state. The Pirani gage may be applied because the principle of Pirani gage is same as this method. This method can obtain the ortho/para ratio continuously. This method is often applied to measurement of ortho and para $H_2$, but it is more difficult to be applied for the measurement of $D_2$ because of the smaller difference of the thermal conductivity of ortho and para state. In addition to the difficulty, the method has a demerit that it cannot decide the absolute value of the ortho/para ratio. By comparing to normal-$D_2$ gas, the change of the ortho fraction from 66.7% can be measured as a change of the voltage, but it is difficult to determine to what the ortho fraction the voltage correspond. Because of this reason, this method did not applied in this paper. Ref.[40] can be a reference of this method.

## 3.4.3 NMR

The NMR (Nuclear Magnetic Moment) is an apparatus possible to determine the ortho/para ratio by measuring the nuclear spins. Many studies have done by using the NMR [15][41][42][43], especially for study of mobility of molecules. In this paper, the NMR method was not used because of the difficulty of the apparatus. See Chapter 26 of ref.[22] for detail of this method.

# Chapter 4 Experiment at PSI

In this chapter, the time integrated measurement on the ortho/para conversion rate for $D_2$ due to the irradiation is described. This measurement was performed at the PSI, Zurich, Switzerland under an adequate guide by Dr. K. Kirch and his colleague. The irradiated liquid $D_2$ samples used as a moderator for the SINQ neutron source were collected after gasified. The sample collection was done approximately every month, from September to December in 2002. The ortho and para contents of the collected samples were measured by means of the Raman spectroscopy.

My major role in this work was to set up a Raman spectrometer including a data acquisition system and to measure the Raman spectra from which the ortho/para contents were reliably extracted.

In Sec. 4.1, the design, construction, and achievement of the reliable data taking for the Raman spectrometer is described. It was also my job to develop an efficient method allowing conversion of the para to ortho $D_2$ states in a short time by using a catalyst and cryostat for a future practical UCN source at the PSI. This is given in Sec. 4.2. The process of sampling, measurement, and deduction of the ortho/para contents for the irradiated samples in the SINQ is described in Sec. 4.3.

## 4.1 Apparatuses of Raman spectroscopy

In order to prepare pure ortho-$D_2$ for deuterium UCN converter, the measurement system for ortho/para ratio of deuterium is necessary for its study. In our case, Raman spectroscopy is used to measure the ortho/para ratio. The schematic view of the setup for the Raman spectroscopy is shown in Fig. 4.1. A laser light (488 nm) is introduced to a sample gas stored in an aluminum vessel with a sapphire windows and the Raman scattering is induced. The scattered Raman light in the direction perpendicular to the incident laser goes out of the side window, and is focused by a lens attached close to a slit of the spectrometer (double monochrometer). The spectrometer converts the change of the wavelength to the change of the detector position. The position signals were taken by a CCD (charge-coupled detector). Data acquisition system for the CCD and the change of the wavelength of the spectrometer were computer controlled.

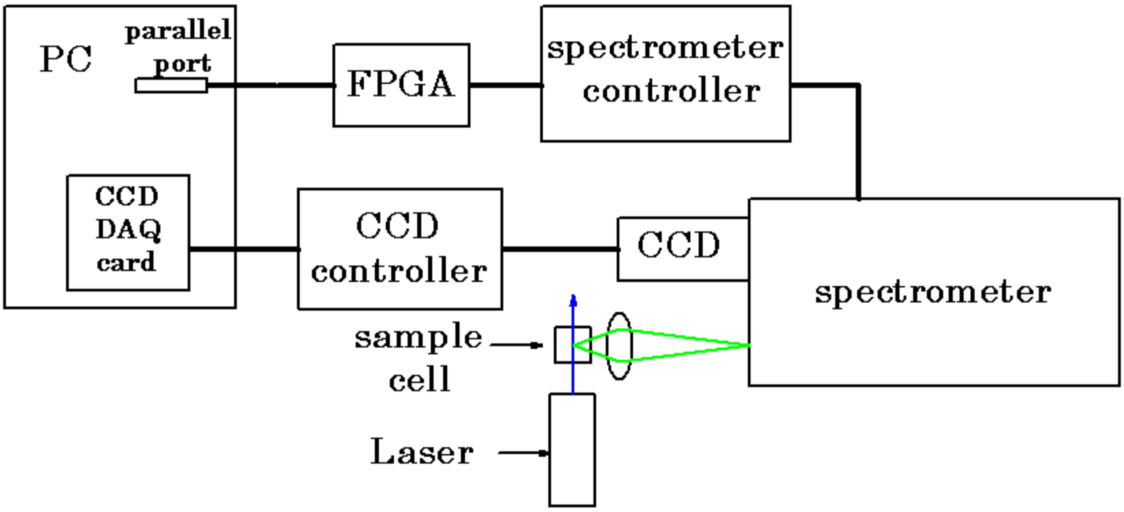

Fig. 4.1: A schematic view of the Raman spectrometer.

### 4.1.1 Spectrometer

The cross section of the Raman scattering is proportional to $\lambda^{-4}$, where $\lambda$ is the wavelength of the laser light. This means that use of shorter wavelength laser light is more efficient for the Raman spectroscopy.

In our work at PSI, an air-cooled Argon ion laser (UNIOHASE model 2013) producing a laser light with the wavelength of 488.0 nm (blue line) was used for this purpose. The laser light is strongly polarized in the transversal direction, and the polarization ratio, vertical/horizontal is more than 250 [44]. The laser power is controlled by an electric current fed to the laser. The maximum power of the laser was 75mW, while 63 mW was used for a stabilized condition.

This laser light was transported into a sample cell through a lens and mirror. The spot size of the laser beam on target was about 100 μm. A focusing lens was set between the sample vessel and an entrance slit of the spectrometer to focus the scattered light from the sample cell on the entrance slit. A schematic view of the laser optics is shown in Fig. 4.2 and Fig. 4.3. The laser is exposed with polarization with direction of perpendicular against detecting direction (up and down in Fig. 4.2 and left and right in Fig. 4.3).

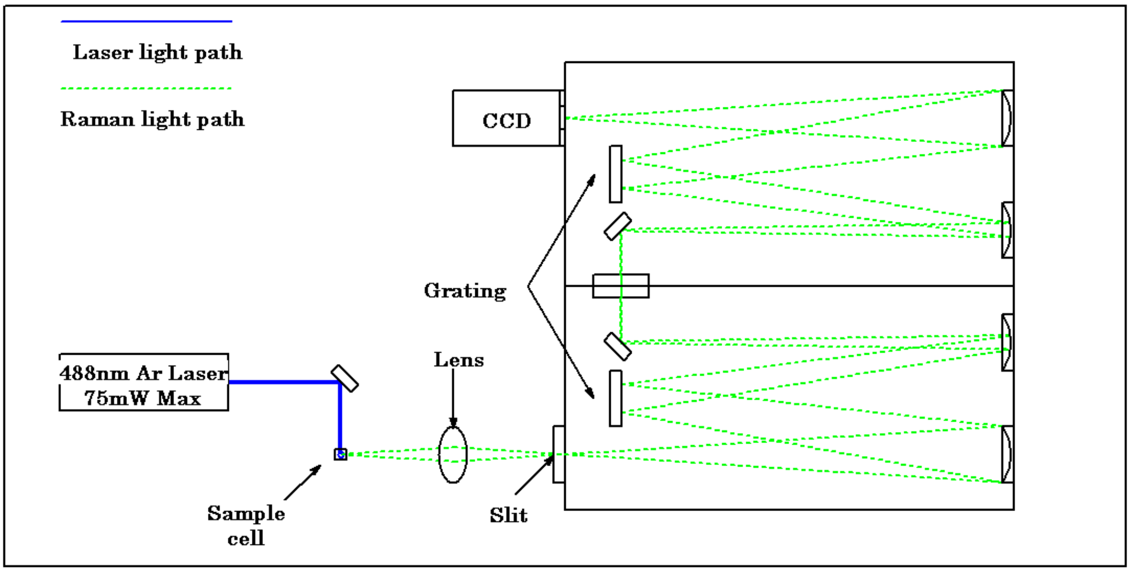

Fig. 4.2: Top view of the Raman spectrometer setup

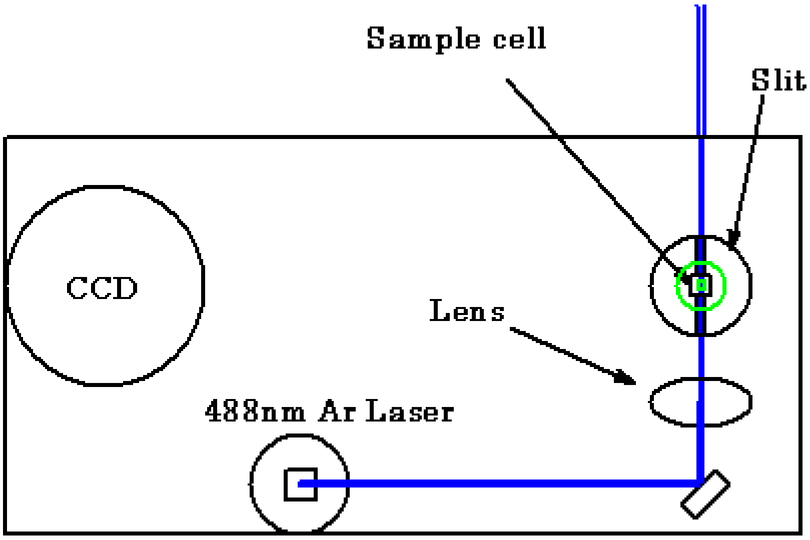

Fig. 4.3: The side view of Raman spectrometer and optics

A sample gas is stored in this sample cell as shown at Fig. 4.4 and Fig. 4.5. The cell was made of aluminum with a cubic shape having a sapphire window at each face for enabling to introduce the laser light and to observe the Raman scattering light. Each sapphire window has a diameter with 10 mm and a thickness with 0.7

mm in thickness. The hole diameter of the cubic Aluminum was 9 mm, and volume of the cell was about 1.9 $cm^3$. A gas line was connected to inside of the cell. These windows and gas connector were glued by Araldite [45]. This cell was used to be evacuated lower than $5.0\times10^{-5}$ mbar by a turbo molecular pomp. The cell was filled with a sample gas with a pressure of about 1 bar.

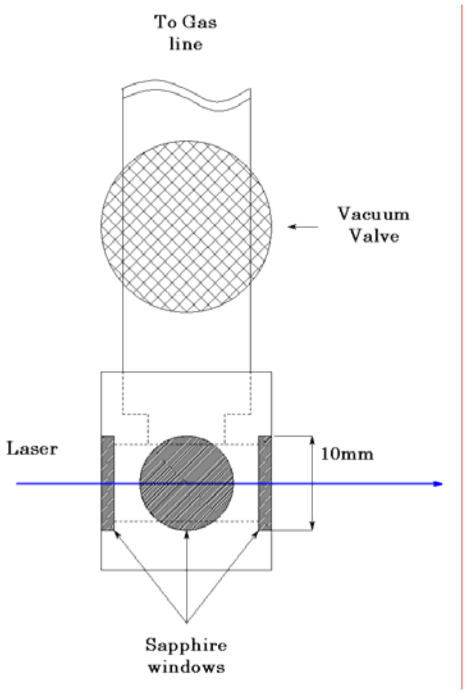

Fig. 4.4: Side view of the Sample cell. NW25 vacuum valve was connected to the cell

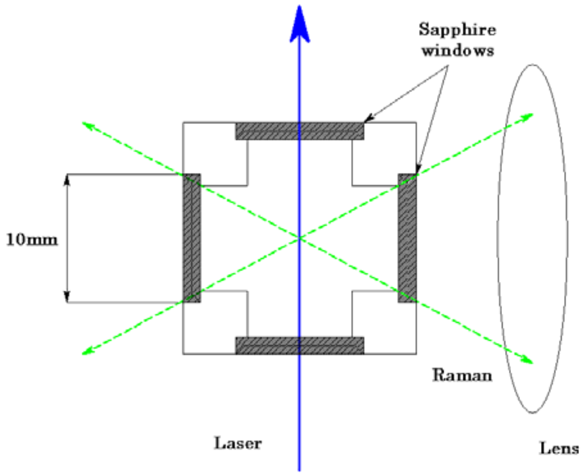

Fig. 4.5: Top view of sample cell. Laser (blue solid) and Raman (green dash) are schematically written.

The Spex14018 3/4-meter double grating spectrometer is used. This spectrometer has 2 dark cells, and 2 grating for each. The gratings have 1200 ditches in 1mm span. The spectrometer has 3 slits. The 2 entrance slits were remotely controlled vertically and horizontally respectively. The horizontal slit changes the horizontal width from 0 to 3 mm continuously, and vertical slit sets at discrete widths, 0, 2, 10, and 20 mm.

Because the light reflection angle by the grating depends on the wavelength of light, a grating can select a specific wavelength to a specific position by controlling the grating angle. The relation of the grating reflection angle is given by

$$d(\sin\alpha + \sin\beta) = m\lambda \tag{4.1}$$

where d is distance of neighboring ditches, $\lambda$ is the wavelength, m is an integer number. $\alpha$ and $\beta$ are an reflection angle of the incoming light and outgoing light measured from the direction perpendicular to the grating surface. Ditches of the gratings are directed vertically, and gratings are rotating horizontally by a stepping motor. An incoming light is reflected by a concave mirror, and is directed to the grating. The grating separates the light pointing to a specific direction for each wavelength. The spectrometer can cover the wavelength range 484 nm to 1364 nm, which correspond 20667 cm$^{-1}$ to 7333 cm$^{-1}$ in unit of wave number. The light with required wavelength is collected to exit of spectrometer by concave mirror.

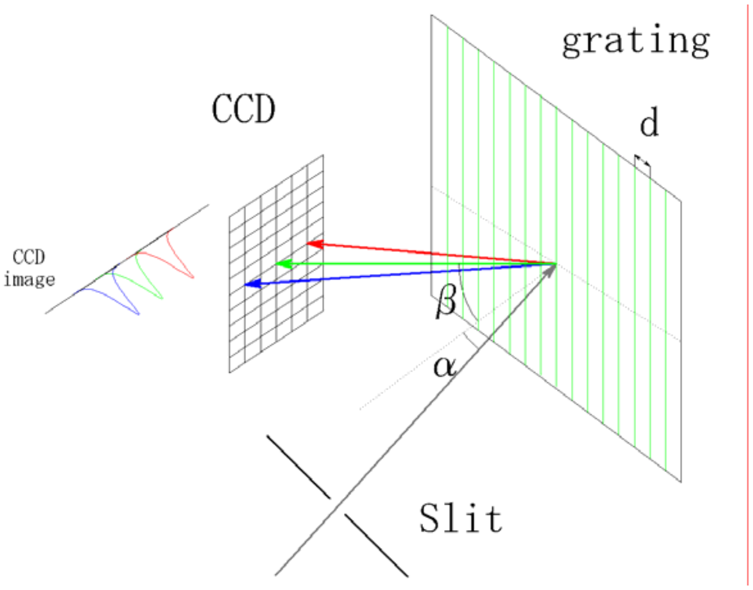

Fig. 4.6: Schematic view of grating and CCD image.

The resolution of the spectrometer is determined by a width of the horizontal entrance slit width and length of light path. For this spectrometer, the resolution is determined by entrance slit width in region that the slit width is more than 50 μm. However, resolution doesn't change even if the entrance slit width is less than 50 μm because length of light path determines the resolution in this region.

The spectrometer has two rooms that have symmetric structure each other. The light that reflected in first room passes through the center slit, and goes to the second room. By repeating same process in second room, the resolution of the spectrum can be much better because it distinguishes the Raman scattering light from the Rayleigh scattering light.

The CCD (Photometrics CH260) was set at an exit of the spectrometer to measure the spectra of the Raman scattering light. The CCD has 512×512 pixels in 1 $cm^2$, which corresponds to one pixel with 20 μm square. The CCD detects photoelectrons that are produced by the light on the CCD surface. One pixel counts photoelectron integrally up to 65535 and it makes 2 bytes binary data. The total counts of photoelectrons for each pixel are collected at the end of the measurement. The CCD has to be cooled around –100°C to suppress the thermal noise. For this purpose, the CCD has the vacuum thermal shield and it was filled with liquid nitrogen. The Photometrics CE200 controls the electronics of the CCD. This device can keep the CCD temperature constant by using a heater in the CCD. This device is also used for the data acquisition and for controlling a switching shutter of the CCD according to the request from the PC, and for supplying an electric power to CCD.

Because the Raman scattering cross section is proportional to $\lambda^{-4}$, a shorter wavelength laser is more effective for the Raman spectroscopy.

This device was inserted in ISA bus, and connected to CE200. In order to take the data from the CCD, a part of source code in the software MOJO (Mount John University Observation) [46] that works on the LINUX OS is used. This software can change the measurement time, and pixel binning.

The wavelength of the light focusing on the CCD can be changed by changing the grating angle. A stepping motor is under the grating to controls its angle. The stepping motor drives the grating when the spectrometer accepts the TTL pulses. One TTL pulse corresponds to the grating angle of 1/50 $cm^{-1}$, which is the minimum controlling unit.

The controlling TTL pulses are made by a field programmable gate array (FPGA) by the requirement of the PC. This FPGA can make the controlling TTL pulses by the required number, required speed, and required direction by the PC operation. The PC and FPGA are connected by a parallel port. The operating system of this PC is RedHat7.0, and data taking and spectrometer controlling program are written in C++ language. Analyzing programs are made by C++ and ROOT system [47].

### 4.1.2 Noise elimination by software

Photoelectrons induced by the light from the spectrometer (or cosmic rays) are stored in a pixel until end of the measurement. When the measurement is finished, the CCD collects the photoelectrons from a certain pixel, stores the number of electrons. The CCD can count the number up to 2 bytes, which means 0 to 65535 counts. The data are stored in a memory of the CCD until the data of all pixels were collected. The CCD gives as an array of 2 bytes × pixel number as a result of the measurement. The maximum data size is 256 kB when 512×512 pixels are used. A typical raw data of the Raman spectrum is shown in Fig. 4.7. Fig. 4.7 is a reconverted histogram of the binary data from the CCD. X pixels (vertical position, row) correspond to the wavelength of incoming light. Y pixels (horizontal position, column) correspond to the height of detector, which doesn't include any information of wavelength. The X projection gives 1D-histogram of the wavelength.

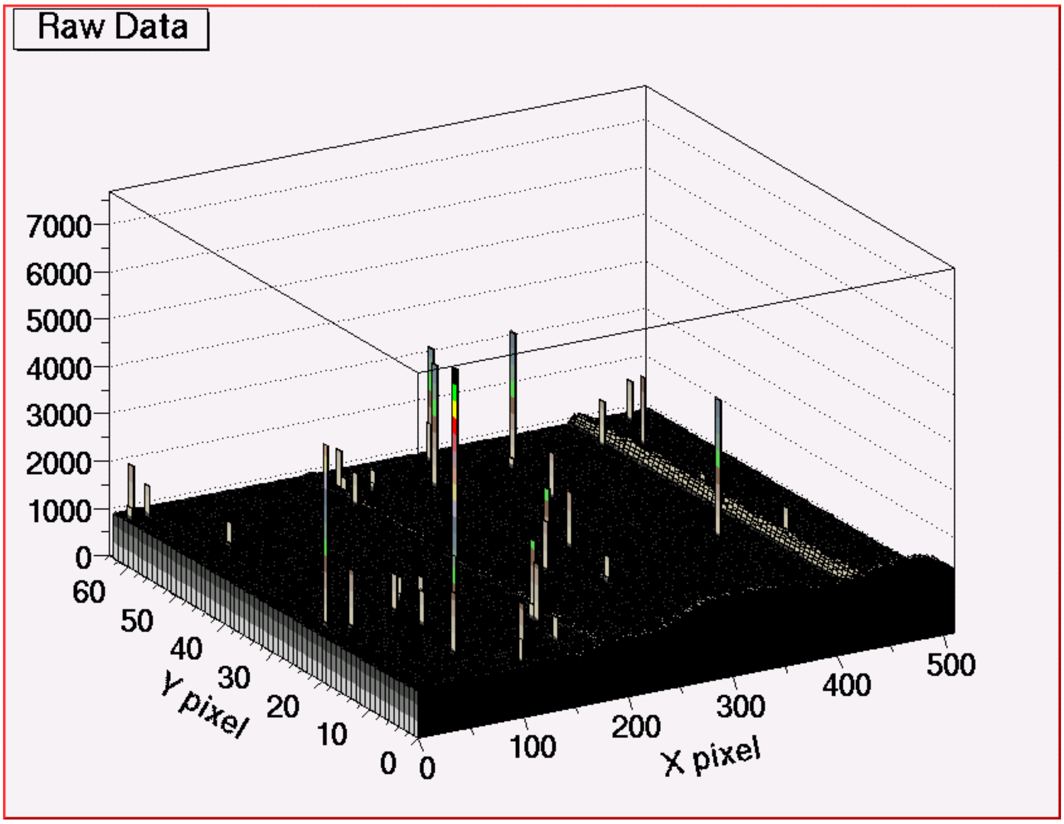

Fig. 4.7: Raw data of the $D_2$ Raman spectrum measured at 500cm$^{-1}$ with a measurement time of 600sec by a laser power of 64mW. An entrance slit width was set 200μm. This data was taken as 512×64 pixels by binning.

#### 4.1.2.1 Cosmic spikes

Huge spikes are seen in the histogram in Fig. 4.7. These spikes are caused by the cosmic rays. For a measurement longer than about 10sec, an effect of the cosmic rays is not negligible. Charged cosmic rays, such as muons or protons, induce the multiple electrons when they are incident on the CCD pixels. The number of electrons could be over 1000 counts for incidence of one charged cosmic ray, while one photon induces less than one photoelectron on average. These cosmic spikes are subtracted by software, in which they were compared with the count of neighboring pixels. An outline of the subtraction procedure is as follows.

The counts detected by each pixel are written by a X×Y dimensional matrix, where X and Y are the number of row and column, respectively.

$$\begin{pmatrix} C_{11} & \cdots & C_{X1} \\ \vdots & \ddots & \vdots \\ C_{1Y} & \cdots & C_{XY} \end{pmatrix} \tag{4.2}$$

Firstly, the value of each column corresponds to the calculated absolute difference of the count relative to the neighbor pixels. Defining the difference in (m,n) pixel as $D_{mn}$, it is given by

$$D_{mn} = \left| C_{mn} - \frac{C_{m(n+1)} + C_{m(n-1)}}{2} \right| \tag{4.3}$$

If we take an average of $D_{mn}$ for each column, it gives a mean fluctuation $\sigma_m$ for each column, where $\sigma_m$ is given by,

$$\sigma_m = \sum_{n=2}^{X-1} \frac{D_{mn}}{X-2} \tag{4.4}$$

If a pixel has an event caused by the cosmic spike, the count has a huge difference from $\sigma_m$. If the $D_{mn}$ is large enough from the column fluctuation, the pixel recognizes that the event is due to the cosmic spike. To discriminate the pixel due to the cosmic spike from the non-cosmic spike pixel, an equation

$$D_{mn} > N\sigma_m \tag{4.5}$$

is used, where N is a discriminating factor. Though in the present analysis, N>2 is enough for the present purpose, N=3 is used for practical analysis. A pixel recognized to the cosmic spike is replaced with an average values between the neighbor pixels, $C'_{mn}$, where $C'_{mn}$ is given by

$$C'_{mn} = \frac{C_{k(n+1)} + C_{k(n-1)}}{2} \tag{4.6}$$

However, in a rare event case such that the cosmic ray gives spikes on a series of columns, spikes could not be properly subtracted. In such a case, the above subtraction procedure is insufficient because even $\sigma_m$ of the normal pixel includes a fluctuation by the cosmic spike. To avoid this problem, the procedure presented from (4.2) to (4.6) is repeated with a matrix replaced with (4.6), until $D_{mn}$ that suffices $D_{mn} > N\sigma_m$ disappears. This procedure is applied to only columns (Y pixels), while the correction of the X pixel was not done because the X pixel includes important information on the wavelength of the Raman spectra. As a result, the raw 2D histogram presented in Fig. 4.7 has been corrected as shown in Fig. 4.8. The sum of Y pixels gives X projection data, which is given by

$$X_m = \sum_{n=1}^{Y} C'_{mn} \tag{4.7}$$

where $X_m$ is X projection data at $m^{th}$ X pixel.

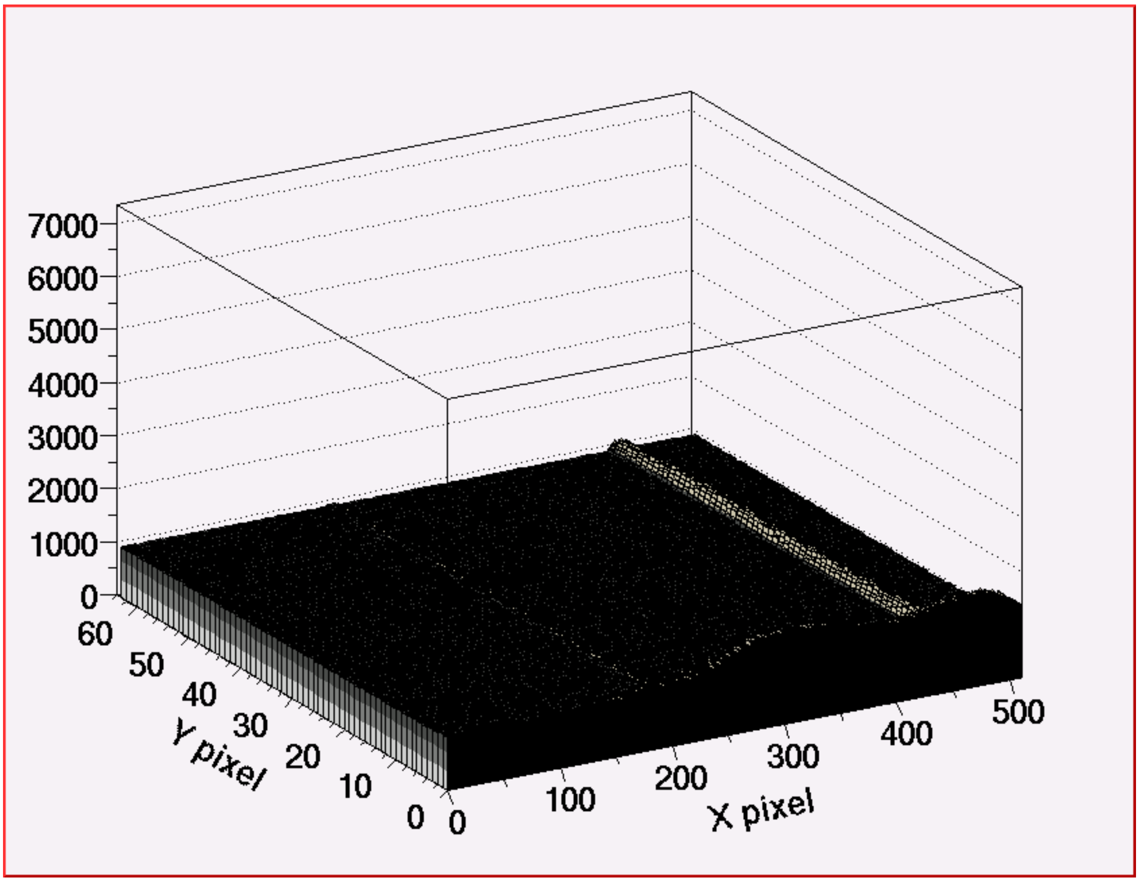

Fig. 4.8: The 2D histogram of Fig. 4.7 after subtraction of the cosmic spikes by the procedure given in 4.1.2.1. All visible cosmic spikes could be reasonably subtracted.

#### 4.1.2.2 CCD Background caused by dark current

The CCD generates a background count even if light is absent. The background spectrum is caused by a dark current in the CCD circuit. The background counts are random events, and those events occur throughout all of the pixel region with an equal probability. The background is subtracted from each pixel when Y pixels are summed to produce the histogram of the X projection. Meanwhile, the background is estimated from an average of pixels in a region where the true events are absent. The background counts for each pixel and its fluctuations are shown in Fig. 4.9 with measurement time 0.2 sec, which is minimum setting. The fluctuation was given by normal distribution around 950 with width of 5~6. The background doesn't depend on measurement time.

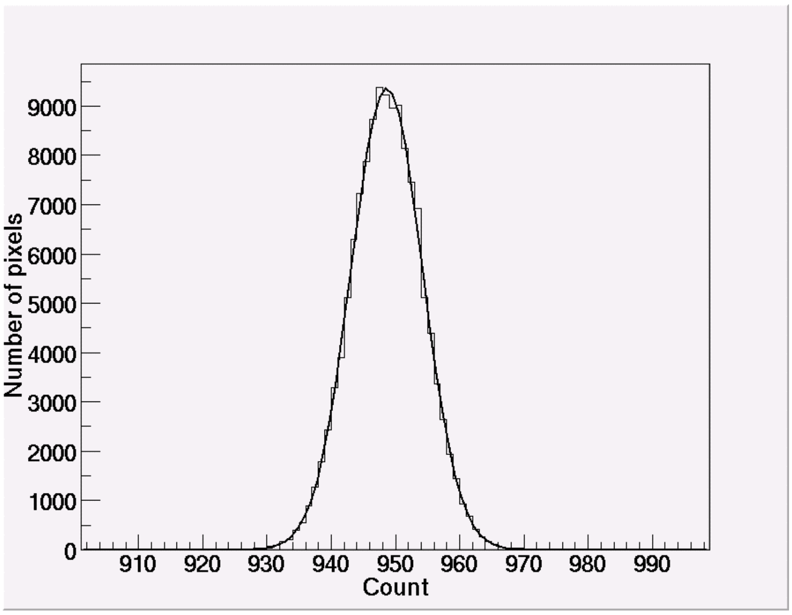

Fig. 4.9: Histogram of readout background count taken as 512×256 pixels (2 binning). The histogram follows normal distribution. The average count and standard deviation are 948 and 5.59 counts respectively.

This CCD has a function of "hardware binning". This function operates multi pixels as one pixel, thus, we can use this 512×512 CCD as 8×256, 64×64 and/or so on. Usually, the X binning is not used because it means reduction of resolution. Concerning the Y binning, it is advantageous in reducing the background fluctuation because the background fluctuation doesn't depend on the binning number, which means even if some pixels are summed to form one pixel by the hardware binning, the summed pixel has 950 counts of the background with the fluctuation 5. The fluctuation of summed background on X projection data is given by

$$\tilde{X}_m = \sqrt{\sum_{n=1}^{Y} \tilde{C}_{mn}{}^2} \tag{4.8}$$

where $\tilde{X}_m$ and $\tilde{C}_{mn}$ are the fluctuations of $X_m$ and $C_{mn}$ respectively. If $C_{mn}$ are independent of m and n, and the binning number, b, eq. (4.8) can be written as

$$\begin{aligned} \tilde{X}_m &= \sqrt{\sum_{n=1}^{512/b} \tilde{C}_{mn}} \\ &= \tilde{C}_{mn}\sqrt{\frac{512}{b}} \end{aligned} \tag{4.9}$$

Therefore, the Y binning as large as possible is favorable, which means that it is important in reducing the background fluctuation to use the Y pixels forming one pixel. However, as explained in section Sec. 4.1.2.1, the Y pixels are used for cosmic spike subtraction. Thus, the largest Y binning must be determined so that the events due to the cosmic spikes can be subtracted with the procedure presented in Sec. 4.1.2.1. Practically the best binning was 8, which means the CCD used with 512×64 pixels.

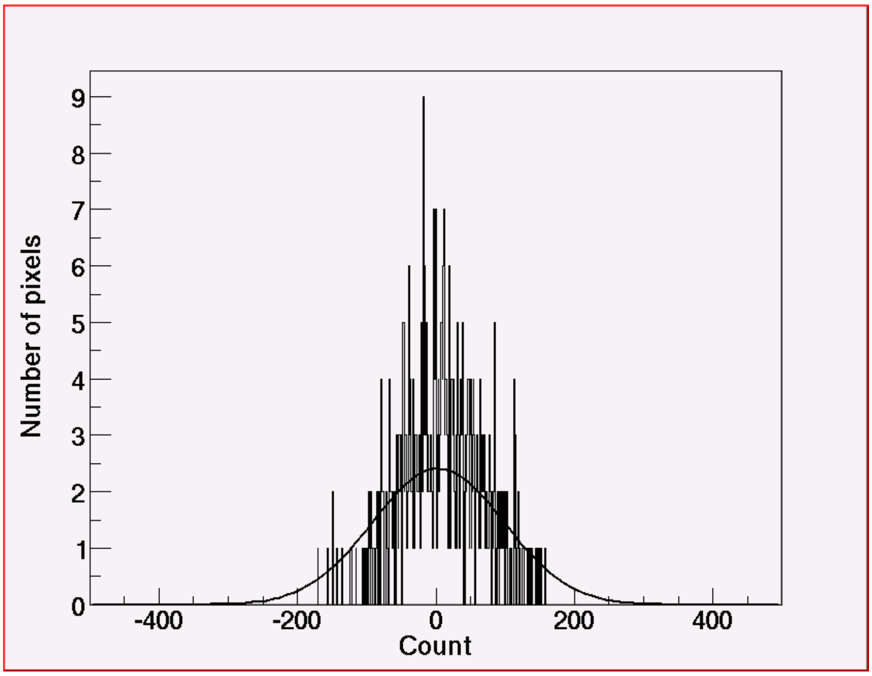

Fig. 4.10: Histogram of X projection of Fig. 4.9. The histogram deviates from the normal distribution.

| Y pixel | Binning | Root Mean Square of Single pixels | Root Mean Square of X projection |
|---|---|---|---|
| **16** | **32** | **5.58** | **31.0** |
| **64** | **8** | **5.58** | **50.9** |
| **256** | **2** | **5.59** | **59.3** |

Table 4.1: The relationship between the binning and root mean square value of the background fluctuation. The root mean square value of the X projection has a trend to follow eq.(4.9) though there is still mismatch with eq.(4.9). This is caused that the fluctuation of each pixel in a column is not independent but has some correlation between pixels.

#### 4.1.2.3 Noise spot

This CCD device has a noise spot at the corner of bottom-right, which correspond to the high X and low Y pixel as shown in Fig. 4.8. The noise is present even if a CCD shutter is closed, and is proportional to the measurement time. In order to remove the events due to the noise spot, a lower part of the Y pixel (about lower 30%) is not used for the present data analysis.

As a result, the final 2D-histogram becomes background free as shown in Fig. 4.11.

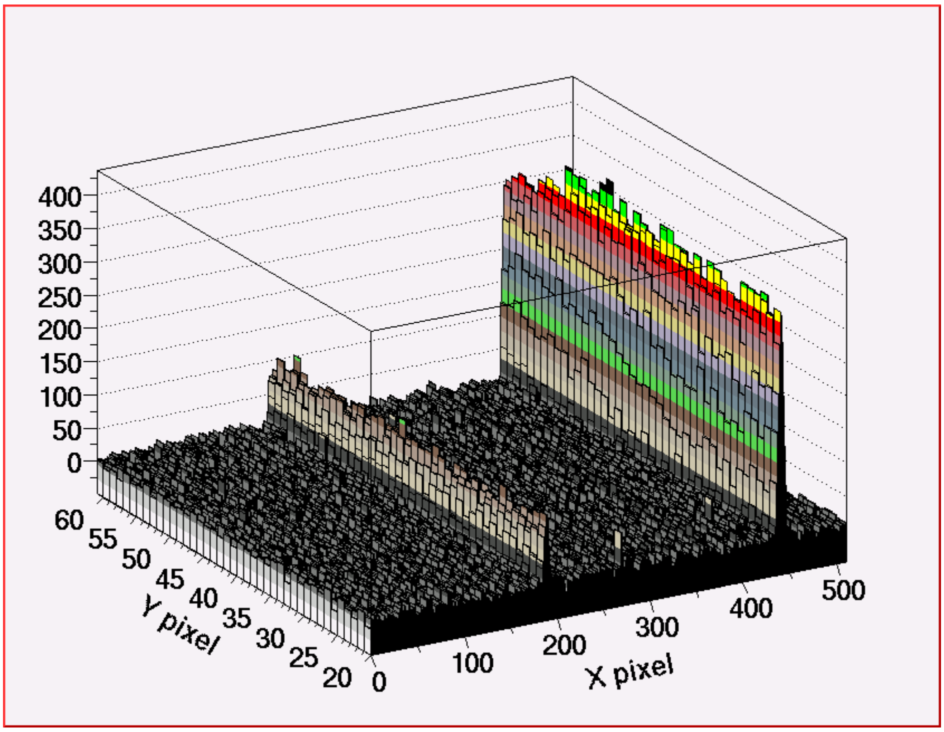

Fig. 4.11: Final data of Fig. 4.7.

Then X projection spectrum is given by summing Fig. 4.11.

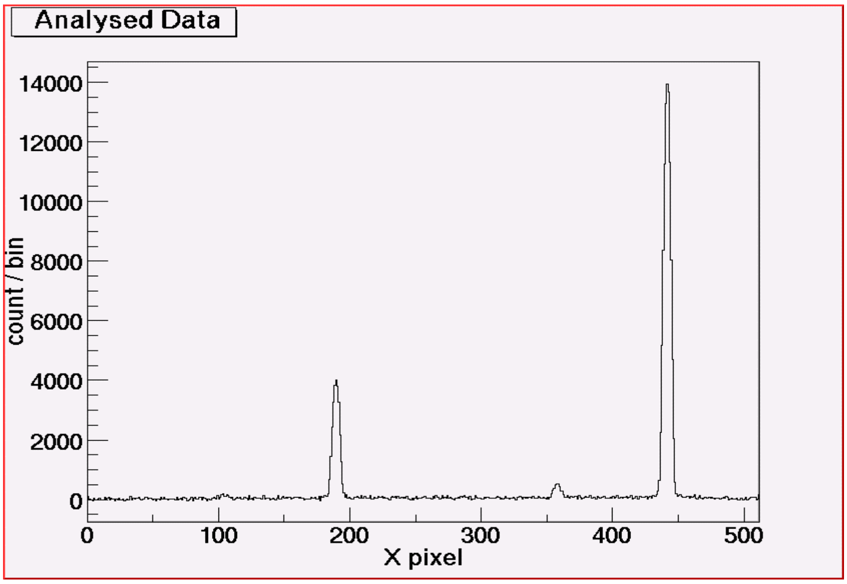

Fig. 4.12: The X projection of Fig. 4.11. High X pixel corresponds to the spectrum at the low Raman shift.

### 4.1.3 Evaluation of Wave number

In Fig. 4.12, X pixel corresponds to the Raman shift. The relationship between the X pixel and Raman shift can be simply evaluated by the wavelength of incident laser, light pass length, interval of groove on grating, angle of grating (spectrometer position), and width of the CCD pixel. The Raman shift is almost proportional to the X pixel, and 1 pixel correspond to 0.3~0.4cm$^{-1}$ in unit of the wave number. Then, X pixels of Fig. 4.12 are converted to unit of the wave number as shown in Fig. 4.13.

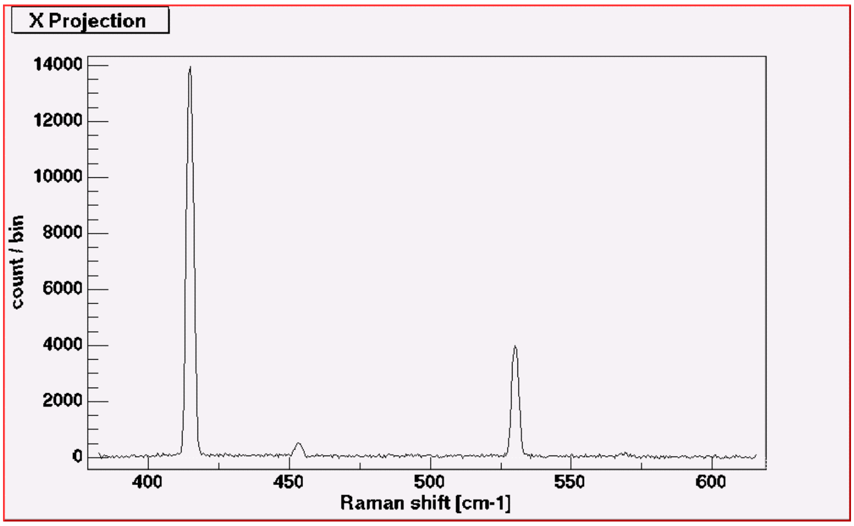

Fig. 4.13: The spectrum of Raman shift made by converting X axis of Fig. 4.12.

### 4.1.4 Performance of spectrometer

#### 4.1.4.1 Monochromaticity of incident laser

In Fig. 4.13, peaks around 410 and 530 cm$^{-1}$ are true events from J(2→4) and J(3→5) transition due to the incidence of 488 nm. The other small peaks in 450 and 570 cm$^{-1}$ are due to the satellite lines deviated from the 488nm line. Fig. 4.14 is spectrum around 0 cm$^{-1}$ taken by air. The peak component is caused by Rayleigh scattering.

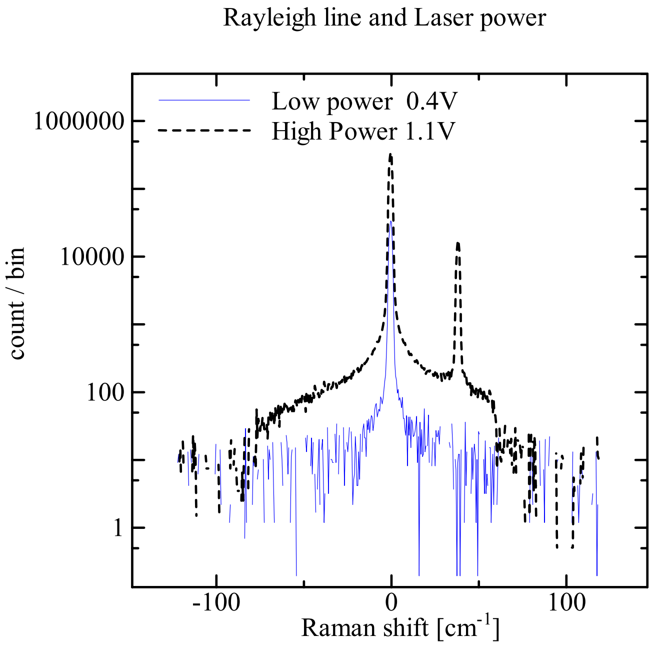

Fig. 4.14: The spectrum of Rayleigh scattering by air. With a at high power operation, a small peak appears with at 40 cm$^{-1}$ wave number. The peak height of small peak was 5% relative to the main peak.

### 4.1.4.2 Resolution

Basically, resolution of the spectrometer is determined by a diameter of laser beam, a width of an entrance slit, and a length of light pass. The wavelength shift from the incident laser and Doppler broadening due to the gas kinematics are negligible small. Fig. 4.15 shows peaks corresponding to the Rayleigh scattering obtained by varying a width of the entrance slit. With a wider slit width than 400 μm, the resolution is restricted by a diameter of the incident laser spot, i.e., the incident laser spot on target is about 400 μm. In the region from 400 μm to 100 μm, the resolution is almost proportional to slit width in this region. In the region less than 100 μm, the resolution doesn't decrease even if the slit width is smaller, while only the peak count decreases. This saturated resolution is determined by the light pass length of the spectrometer.

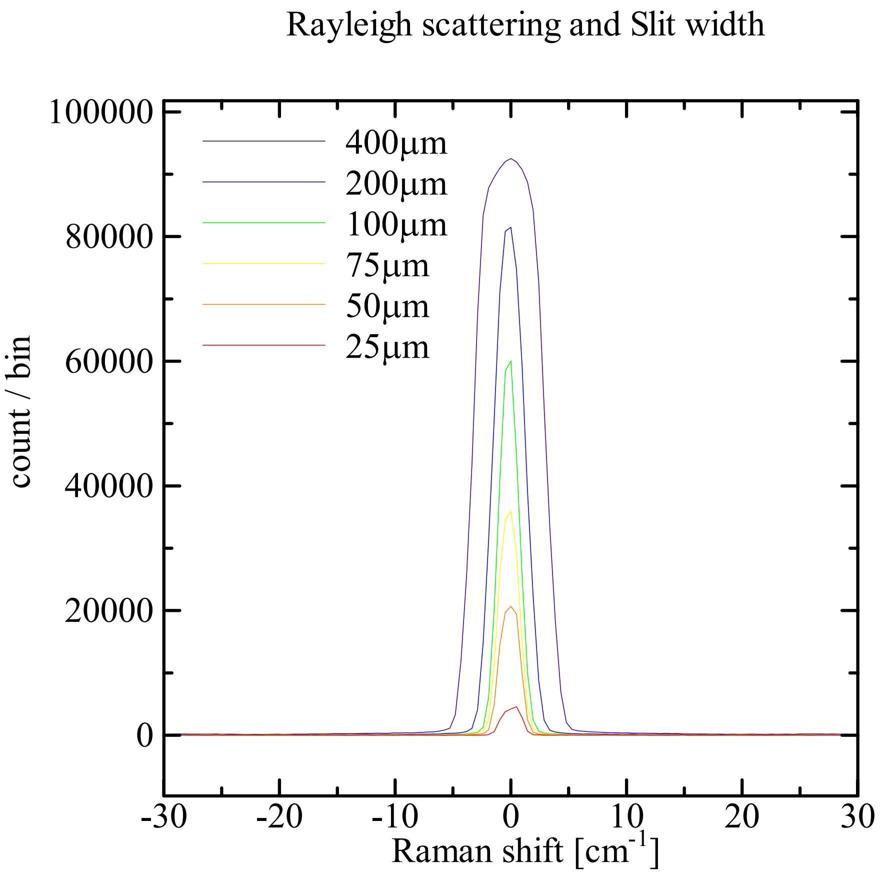

Fig. 4.15: Spectrum of the Rayleigh scattering by air with a different width of entrance slit. The peak width decreases in proportion to a slit width until 100 μm. In the region of less than 100 μm, the peak width is saturated.

### 4.1.4.3 Background from Rayleigh scattering

The cross section of Rayleigh scattering is more than $10^6$ times larger than that of the Raman scattering. Therefore, reduction of contribution from the Rayleigh scattering is very important for the Raman spectroscopy, especially for the measurement around the low Raman shift region. Generally, a usual single grating spectrometer is not ideal because it sometimes induces unfavorable scattering, use of two or three gratings are useful for a precise measurement at the low Raman shift region. A typical spectrum of $D_2$ gas measured around 200 cm$^{-1}$ Raman shift is shown in Fig. 4.16. At a smaller region below 160 cm$^{-1}$ the Rayleigh scattering or diffused laser by the sample cell becomes predominated. The laser light diffused by the Raman cell was 10 times larger than the Rayleigh scattering from gas.

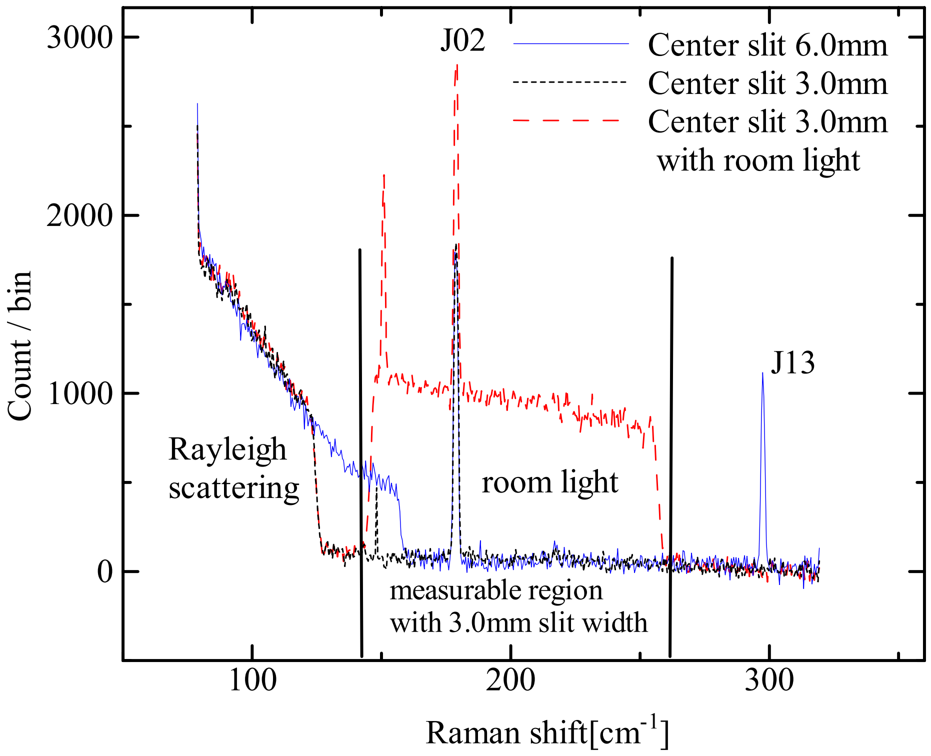

Fig. 4.16: Raman spectrum around 200 cm$^{-1}$. The solid line (blue) and dot (black) line correspond to the measurements with a center slit width of 6mm and 3 mm respectively. The dash line (red) corresponds to the same condition of the dot line with a fluorescent lamp. The lamp spectrum is almost white (containing all of visible line continuously) but has an intrinsic peak at 150 cm$^{-1}$.

Our double grating monochrometer has two cells, and a slit (center slit) is located between two cells. By adjusting the width of the center slit, an effect of the pedestal background caused by the Rayleigh scattering was minimized. In Fig. 4.16, it is seen that the change of slit width from 6.0mm to 3.0 mm cut a part of the pedestal at 120~160 cm$^{-1}$. However, 3.0 mm slit width reduces measurable region to 150~260 cm$^{-1}$ though 6.0 mm slit covers region of 80~320 cm$^{-1}$. The measurement region was checked by using the fluorescent lamp.

### 4.1.5 Raman spectrum and ortho fraction of $D_2$

By using the former setup and analysis, the $D_2$ spectra were measured. Some of the measured spectra of the rotational band (v,J→v,J+2) and vibrational band (v,J→v+1,J) are shown in Fig. 4.17 and Fig. 4.18, respectively. The peak areas are obtained by Gaussian fitting, and the ortho fraction and temperature can be deduced by using these peak areas. See Appendix 7.1 for further detail of the Raman scattering.

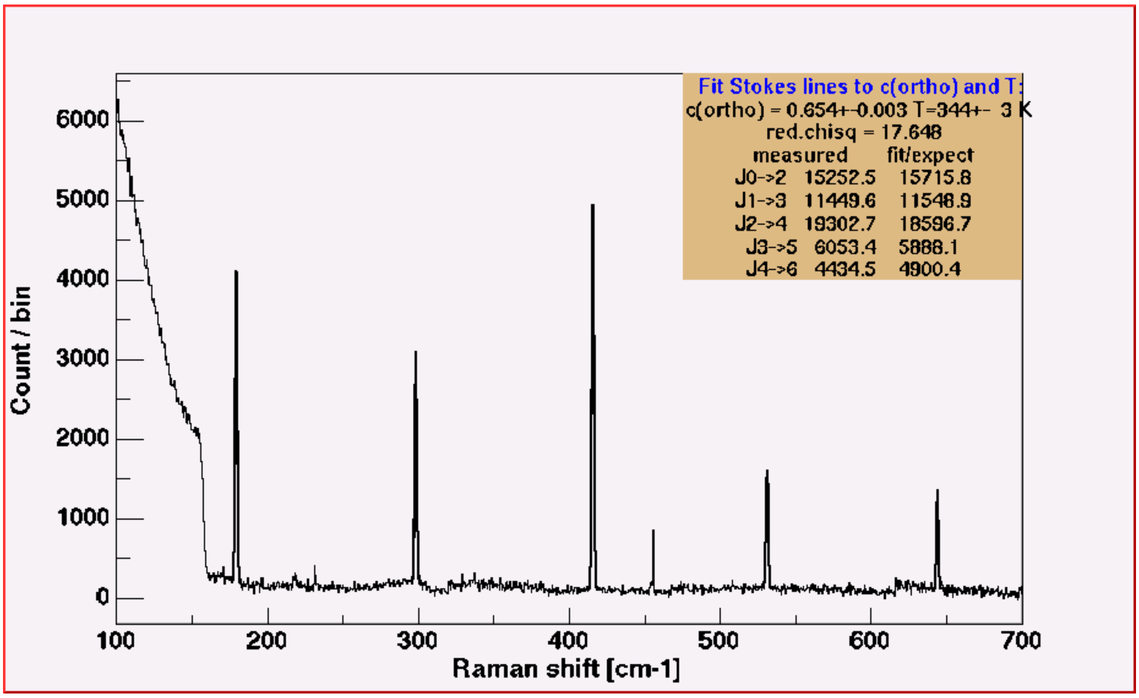

Fit Stokes lines to c(ortho) and T:
c(ortho) = 0.654+-0.003 T=344+- 3 K
red.chisq = 17.648

| | measured | fit/expect |
|---|---|---|
| J0->2 | 15252.5 | 15715.8 |
| J1->3 | 11449.6 | 11548.9 |
| J2->4 | 19302.7 | 18596.7 |
| J3->5 | 6053.4 | 5888.1 |
| J4->6 | 4434.5 | 4900.4 |

Fig. 4.17: Raman spectrum of the rotational band for the thermal $D_2$ from J0→J2 transition to J4→J6 transition (Stokes). This spectrum was constructed by folding 4 measurements at 200, 350, 500, and 600 $cm^{-1}$. Each measurement is taken with a period of 600sec, a laser power of 63mW, and a slit width of 50 μm.

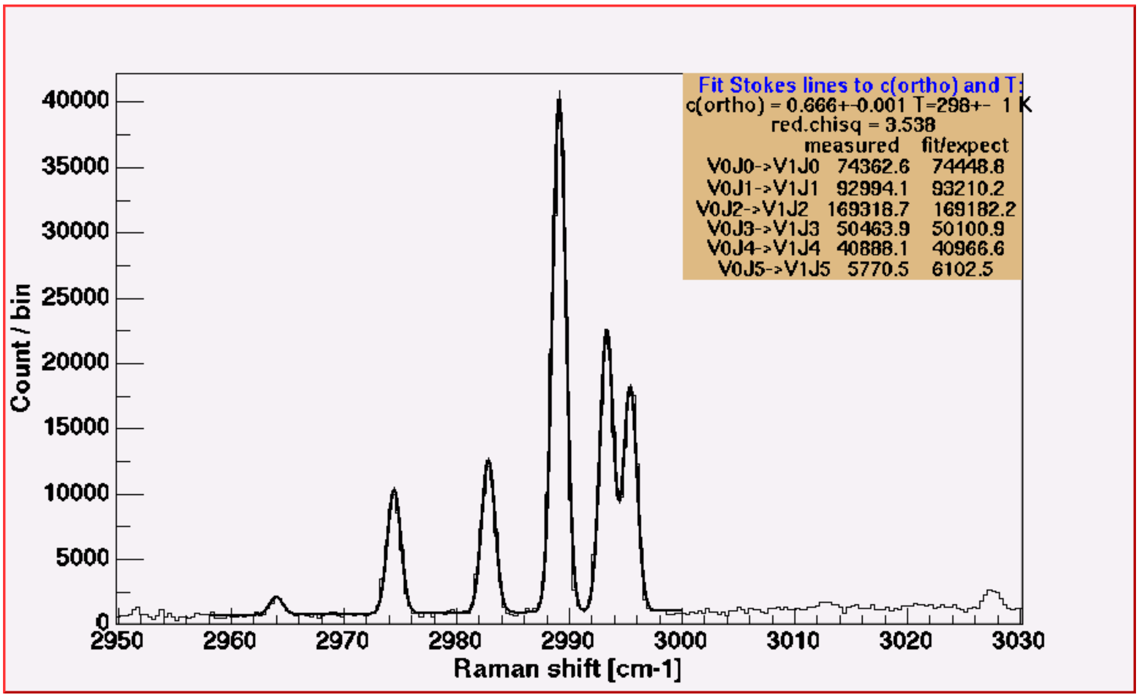

Fig. 4.18: Raman spectrum of the vibrational band for the thermal $D_2$ from J0→J2 transition to J5→J7 transition. This spectrum was constructed by summing up of 5 measurements taken at 3000 $cm^{-1}$. Each measurement is taken with a period of 600sec, a laser power of 63 mW, and a slit width of 100 μm.

#### 4.1.5.1 Observation of Rotational band

In Fig. 4.17, the observed five Stokes lines for the rotational scattering are shown. The peak at the lowest Raman shift corresponds to the transitions of the rotational state with J=0 to that with J=2 for the $D_2$ molecule. The 2nd, 3rd, 4th, and 5th peak correspond to the transition from J=1 to J=3, that from J=2 to J=4, that from J=3 to J=5, and that from J=4 to J=6, respectively. According to Chapter 3, Appendix A,B, and 7.1, the peak yields of $J^{th}$ Stokes lines, Y(J), can be written as

$$Y(J) = I\Omega\varepsilon(\omega_J)\omega_J{}^4 c(J)P(J)B_{JJ+2} \tag{4.10}$$

where I is a flux of incident laser, ω and $\omega_J$ are a wave numver of incident laser and photon scattered by a molecule in the $J^{th}$ rotational state, $\varepsilon(\omega_J)$ is an efficiency of the spectrometer for photon with $\omega_J$, Ω is an effective solid angle subtended by the spectrometer, P(J) is a population function given in eq.(3.6), $B_{JJ+2}$ is the Placzeck Teller coefficient given in eq.(C.3) in Appendix 7.1. The c(J) is a function given by the molecular ortho/para fraction, which is described as

$$c(J)=\begin{cases} c_o & J=even \\ c_p & J=odd \end{cases} \tag{4.11}$$

where $c_o$ and $c_p$ is ortho and para fraction given in (3.12), and $c_o+c_p=1$.

The procedure to determine the ortho fraction is as follows. In order to determine the value of $c_o$, other parameters in eq(4.10) have to be decided in advance. $B_{JJ+2}$ are theoretically given in (C.3) in Appendix 7.1. P(J) can be calculated assuming the Maxwell-Boltzmann distribution if the sample temperature is known because the energy state of $D_2$, $E_J$, are given in Appendix B. Thus, if the Raman shift is enough small so that $\omega_J$ may be approximately constant, eq(4.10) is simplified as

$$Y(J)=Wc(J)P(J)B_{JJ+2} \tag{4.12}$$

and with P(J) expressed by the Maxwell-Boltzmann factor, Y(J) is given by

$$Y(J)=Wc(J)(2J+1)\exp(-\frac{E_J}{k_BT})\frac{(J+1)(J+2)}{(2J+1)(2J+3)} \tag{4.13}$$

The eq (4.13) has three free parameters, W, T, and $c_o$, and these three parameters can be obtained in the course of the peak fitting procedure.

#### 4.1.5.2 Observation of vibrational band

Fig. 4.18 is a spectrum of the vibrational band in the region of the Q-branch. The highest Raman-shifted peak at 2996 $\text{cm}^{-1}$ corresponds to the transition from (v=0, J=0) state to (v=1,J=0) state, where v is the vibrational quantum number. Other lower Raman-shifted peaks correspond to the rotational band with the higher angular momenta. These peak heights also include information of the ortho fraction and temperature and these parameters can be simultaneously obtained by the fitting procedure. In a similar way that the Raman spectrum for the rotational transition can be fitted with eq(4.10), the vibrational transition can be fitted with the function $Y_V(J)$ given by

$$Y_V(J)=I\Omega\omega_J{}^4c(J)P(J)\left(\varepsilon(\omega_J)\alpha^2+\varepsilon_\perp(\omega_J)\gamma^2\frac{4}{45}B_{JJ}+\varepsilon_\parallel(\omega_J)\gamma^2\frac{3}{15}B_{JJ}\right) \tag{4.14}$$

where α and γ are the Raman isotropic and anisotropic polarizability, respectively. For the vibrational transition, the cross section and scattering direction depends on the direction of polarization of incident laser while the rotational transitions are independent of the polarization and the scattering direction. As shown in eq(4.14), the equation consists of an isotropic term including α and anisotropic term including γ and $B_{JJ}$. The anisotropic terms can be divided into two components: one is a term corresponding to a photon with the perpendicular polarization and the other is a term corresponding to a photon with the parallel polarization scattered by the grating grid. In this case, an incident laser has a perpendicular polarization, where the perpendicular scattering means a scattering of photon with the same polarization with respect to the incident laser.

In eq(4.14), three efficiencies, $\varepsilon(\omega_J)$, $\varepsilon_{\perp}(\omega_J)$ and $\varepsilon_{||}(\omega_J)$ corresponding to the isotropic, perpendicular, and parallel polarization, respectively, are used because reflection efficiencies of the grating strongly depend on the polarization and grid direction. Since the necessary information for the fitting procedure is only J dependence of $Y_V(J)$, $Y_V(J)$ in eq. (4.14) can be simplified as a function of J as shown by

$$Y_V(J) = Wc(J)P(J)\left(1 + kB_{JJ}\right) \tag{4.15}$$

Therefore, the fitting function can be written as eq.(4.15) with one more free parameter, k relative to eq. (4.12). In consequence, eq.(4.15) can be written as

$$Y(J) = Wc(J)(2J+1)\exp(-\frac{E_J}{k_B T})\left(1 + k\frac{J(J+1)}{(2J-1)(2J+3)}\right) \tag{4.16}$$

### 4.1.5.3 Procedure to calculate ortho fraction

The $\chi^2$ square fitting is used to fit the Raman spectra. The procedure is as follows. In the $\chi^2$ fitting procedure, the parameters are decided so that the $\chi^2$ prescribed by

$$\chi^2 = \sum_J \frac{\left(S(J) - Y(J)\right)^2}{\Delta S(J)^2} \tag{4.17}$$

may be minimized, where S(J) is a peak count for the $J^{th}$ peak, Y(J) is the theoretical function given in eq. (4.13), and ΔS(J) is the error of S(J).

For rotational band, the peak counts are decided by fitting them assuming the Gaussian function with first polynomial, f(x), which can be written as

$$f(x) = a_0 \exp\left(-\left(\frac{x - a_1}{a_2}\right)^2\right) + a_3 x + a_4 \tag{4.18}$$

where x is a bin of x-axis, and $a_0$~$a_4$ are fitting parameters. The peaks are fitted by function f(x) by using the least squares method.

The S(J) is given by integration of f(x), which is given by

$$S(J) = \int_{-\infty}^{\infty} f_J(x)dx = \sqrt{2\pi}a_0 a_2 / b \qquad (4.19)$$

where $f_J(x)$ is a function f(x) which is used to fit the $J^{th}$ peak, b is width of bin, 0.3~0.4 $cm^{-1}$. The error of the peak counts ΔS(J) is given by the errors caused by the statistical error and the background subtraction, which is given by

$$\Delta S(J) = \sqrt{S(J) + \Delta B(J)^2} \qquad (4.20)$$

where ΔB(J) is the fluctuation caused by the background subtraction described in Sec4.1.2.2. Thus, ΔB(J) is given by the fluctuation in case of 8binning, 50.9 per bin, times square root of number of bin used for summention, here $2a_2/b$ was used. Thus, ΔB(J) was about 150 count.

In case to deducde peak counts of vibrational lines, peaks, especially v1J0 and v1J1 transision, are too close to distinguish, and overlaping each other. Thus, fitting function of $f_v(x)$

$$f_v(x) = \left\{ \sum_{n=1}^{6} a_{n0} \exp\left( -\left( \frac{x - a_{n1}}{a_{n2}} \right)^2 \right) \right\} + a_3 x + a_4 \qquad (4.21)$$

is used instead of f(x) of eq(4.18). S(J) and ΔS(J) are deduced by same procedure for rotational band.

When we observe the peak number larger than the number of free parameters (in this case three), the unknown parameters that give the minimum $\chi^2$ are obtained as the most probable values.

A typical example of the fitting is carried out for a $D_2$ sample at room temperature as shown in Fig. 4.17, where the parameters, temperature T and ortho fraction $c_o$, were obtained and T=344±3 and $c_o$=0.654±0.003 were deduced. The errors are due to the statistics. On the other hand, the most probable values of $c_o$ should coincide with the theoretical prediction, i.e., 2/3 (0.667) and T should be room temperature. Therefore, some inconsistency seems to exist.

The fitting of Fig. 4.18 with four free parameter gave T=298±1 and $c_o$=0.666±0.001. This result shows a satisfactory agreement with the expection. The parameter k is determined by the intrinsic charactaristics of the spectrometer. The deduced k from the analysis of Fig. 4.18 is 0.273. A certain discrepancy between the experimental result and fitting curves are observed for the rotational transition. This suggests the presence of efficiency variation with $\omega_J$.

On the other hand, though the vibrational transition need much better resolution than rotation, it has the following merits:

1) The spectrum is free from Rayleigh scattering.
1) Whole spectrum can be taken in one picture. It makes possible to ignore fluctuation of laser intensity.
3) All scattering photon wave number $\omega_J$ are very close so that $e(\omega_J)$ is constant over all J.

1) The spectrum is free from the Rayleigh scattering,
2) Since the whole spectrum can be taken in one setting of the spectrometer, there is no instrumental instability due to other settings of the spectrometer.
3) $e(\omega_J)$ can be regarded as constant because the range of $\omega_J$ is narrow.

Because of these reasons, the observation of the vibrational transition was adopted for the measurement of the ortho fraction.

## 4.2 Measurement of ortho/para conversion

### 4.2.1 Apparatus for ortho/para conversion

As described in section 3.3, a cold catalyst can change ortho/para ratio of $D_2$.

It is a well known fact that a para-magnetic material is effective to conversion of the ortho/para states. In the present work, Oxisorb®[48] is used as a catalyst. Oxisorb® consists of a silica gel impregnated with $CrO_3$[49] which has been used as an oxygen filter because it absorbs a plenty amount of oxygen. The catalyst is set in a cell in the GM cryostat which has a cooling power down to 10K.

A scheme of the cryostat system is shown in Fig. 4.19. The catalyst is set in a copper cell with caps at both ends. Narrow gaps (~20 μm) at both ends allowed gas or liquid $D_2$ to flow through them.

The gas system is shown in Fig. 4.20.

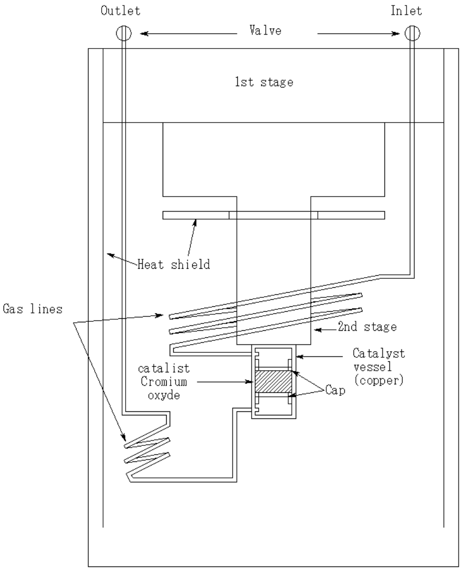

Fig. 4.19: Scheme of cryostat for $D_2$ ortho/para conversion [53].

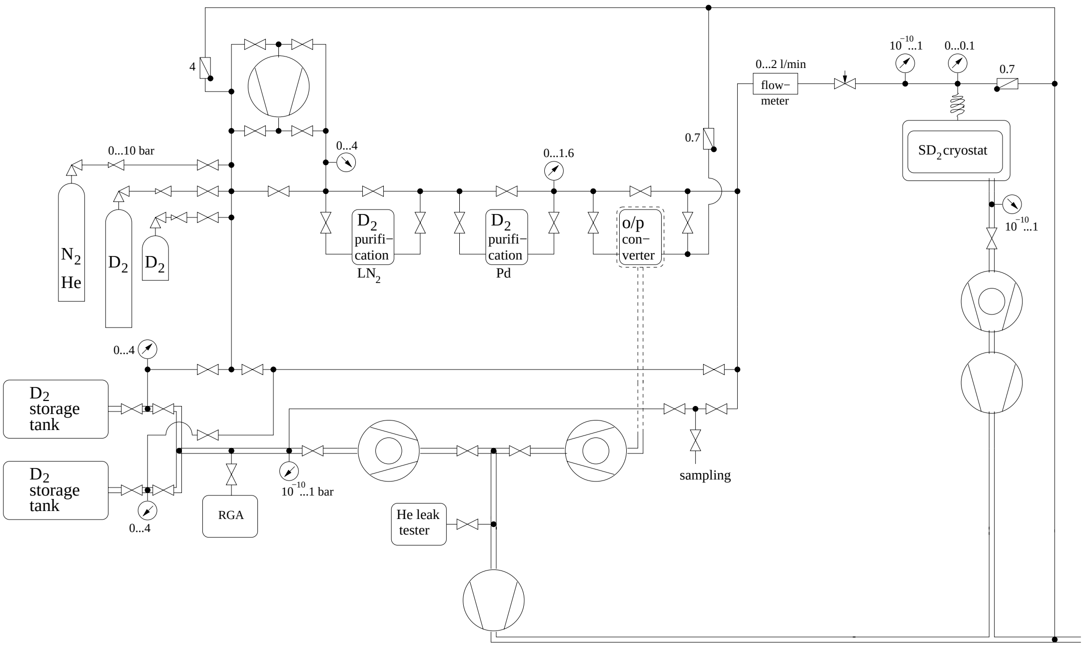

Fig. 4.20: Scheme of $D_2$ gas line [53].

For conversion of $D_2$ gas, 40 liter of $D_2$ gas was kept in the catalyst cell at 18.7 K (the triple point of $D_2$). The $D_2$ gas was introduced to the catalyst cell after cooling. In order to remove the gas staying in the capillary tube that did not contact with the catalyst, gas flushing was done a few times.

The ortho fraction of the gas was 86.1±0.4% after 2.5 hours cooling. After 1.3 days it became 98.5%±0.1%, which is just the value of thermal equilibrium expected by eq. (3.15). On the other hand, the ortho fraction of $D_2$ cooled without catalyst was 68.0% with 8 hours cooling.

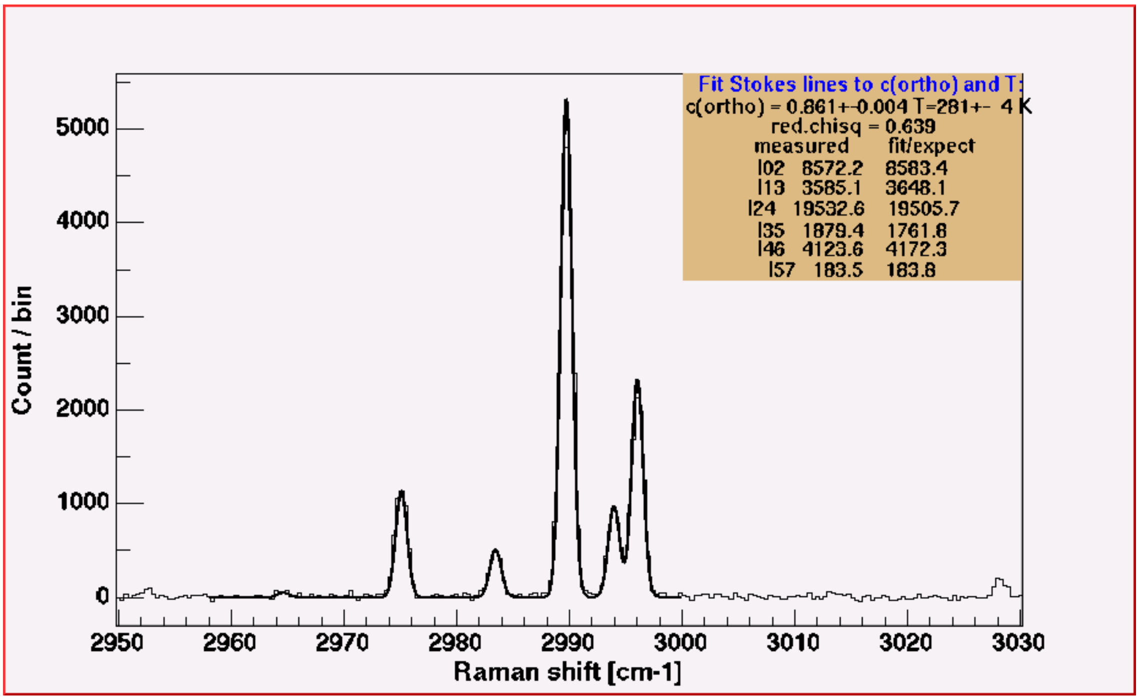

Fig. 4.21: Raman spectrum for the vibrational band of $D_2$ gas after 2.5 days cooling at 18.7K with catalyst.

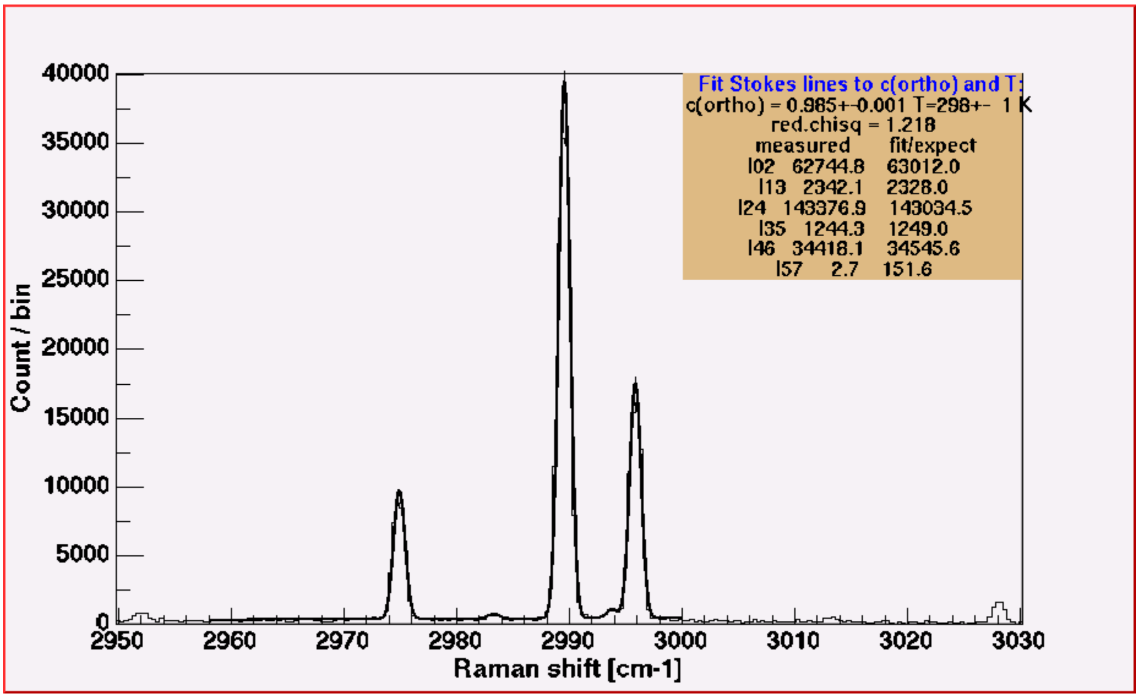

Fig. 4.22: Raman spectrum for the vibrational band of $D_2$ gas after 1.3-day cooling at 18.7 K with catalyst.

### 4.2.2 Relaxation

As shown in the next section, the irradiated liquid $D_2$ is sampled from the SINQ after gasification and stored in a sample vessel (50 cc volume) made of stainless steel for the Raman spectroscopy. It is a well known fact that the conversion from the ortho to para is very slow; a relaxation time (conversion time) due only to the gas collisions is sometimes over 100 days. However, the relaxation time due to a wall collision of the stainless steel is not established yet. Generally speaking, the relaxation mechanism of the wall surface is known to depend not only on the surface material but also on the ratio of the surface area to the container volume. In the present work, it is of particular importance to experimentally determine the relaxation time due to the wall relaxation time for the reliable measurement of the irradiation effect on the ortho/para conversion.

For this purpose, we use the ortho $D_2$ purified by the catalyst at low temperature. This purified $D_2$ sample is, then, gasified and stored in a stainless vessel at room temperature for the Raman spectroscopy.

The relaxation (conversion) effect due to the wall relaxation is given by eq. (3.20). The solution of eq. (3.20) shows that the ortho fraction is linear with the time.

The time dependence of the ortho fractions for the purified ortho $D_2$ gas stored in the stainless steel vessel was measured 4 times over 34 days as shown in Fig. 4.23, where the solid curve is a theoretical calculation assuming an exponential function with a relaxation time of 36±0.7days. The vessel pressure was decreasing to almost half of initial pressure because a part of the stored gas should be transferred to a Raman cell at each measurement of the Raman spectroscopy.

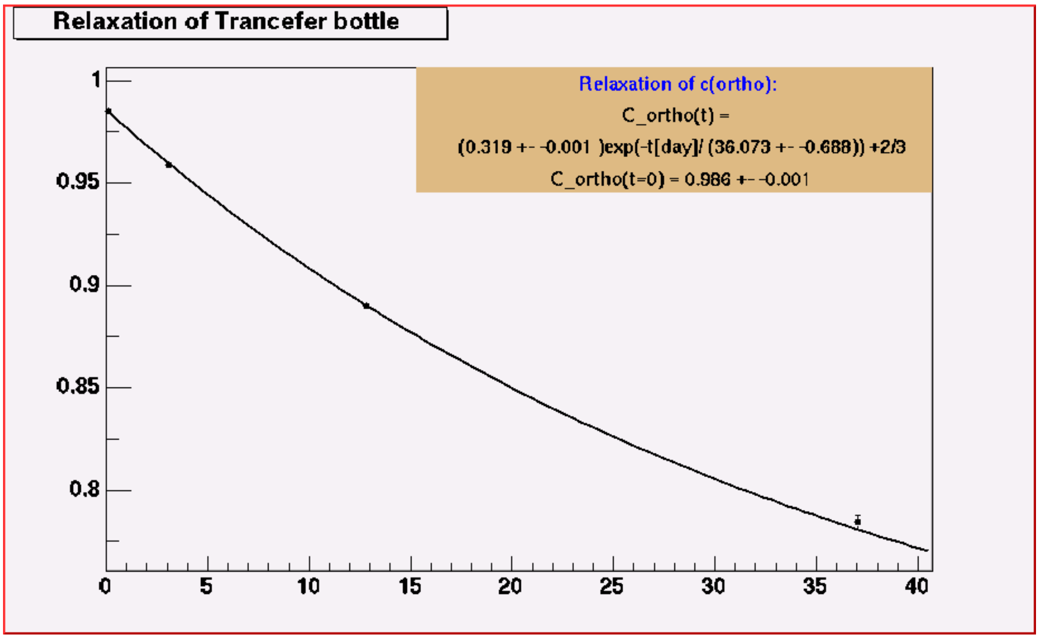

Fig. 4.23: Observed ortho fractions are plotted as a function of time (day). The solid curve is an exponential curve with a lifetime of 36 days.

The fact that the experimental results are well reproduced by the calculation suggests that both of the ortho and para $D_2$ components are equally influenced by the catalyzing effect of the wall surface.

On the other hand, the purified ortho $D_2$ gas was kept for a long time in the sample cell of the Raman spectroscopy made of Al with 4 sapphire windows and the time dependence of the relaxation was measured. The results showed the relaxation time of 8.4 days. It is very interesting to compare this result with the result obtained from the much larger Al container (~40 liter) of liquid $D_2$ used for the moderator of the SINQ. The relaxation time for this big container was 903 days.

From the above experimental results it is found that the wall relaxation time is mainly determined by the surface to volume ratio, which is reasonably understood in terms of the surface catalyzing model described in eq(3.20), i.e., the number of molecules which converse from the ortho to para or vice versa is proportional to the surface area and the total number of molecules is proportional to the volume of the container.

### 4.2.3 HD contamination

The HD contamination in the $D_2$ makes a serious reduction in the UCN density when the D2 is used as a converter of UCN production. In fact, the absorption cross section of thermal neutron by hydrogen is 333 mbarn, which is 600 times larger than the deuteron absorption cross section of 520 μbarn[54]. Therefore, it is very important to estimate the HD fraction contained in the $D_2$ gas. Fortunately, we have developed a convenient method to determine it by the Raman spectrum.

As shown in Appendix B, the energy levels of HD are about 1.5 times larger than $D_2$. By comparing the peak intensities of the rotational transition from J=2 to J=4 of $D_2$ and that from J=1 to J=3 of HD, the fraction of the HD can be deduced. Appendix 7.1 is instructive to know the Raman spectrum of the HD. The temperature was assumed as 300K, then the HD molar fraction, [HD] is given by

$$\frac{[\mathrm{HD}]}{[\mathrm{H}_2][\mathrm{D}_2]} = K(300K) = 1.78 \tag{4.22}$$

from ref.[55], where $[H_2]$ and $[D_2]$ are molar fraction of $H_2$ and $D_2$. At the higher temperature, K(T) is asymptotically becoming close to 2.

The Raman peaks in the region of 500 $\mathrm{cm}^{-1}$ are shown in Fig. 4.24. The peak at 416$\mathrm{cm}^{-1}$ is the J2→J4 transition of $D_2$, and the peak at 444 $\mathrm{cm}^{-1}$ is the J1→J3 transition of HD.

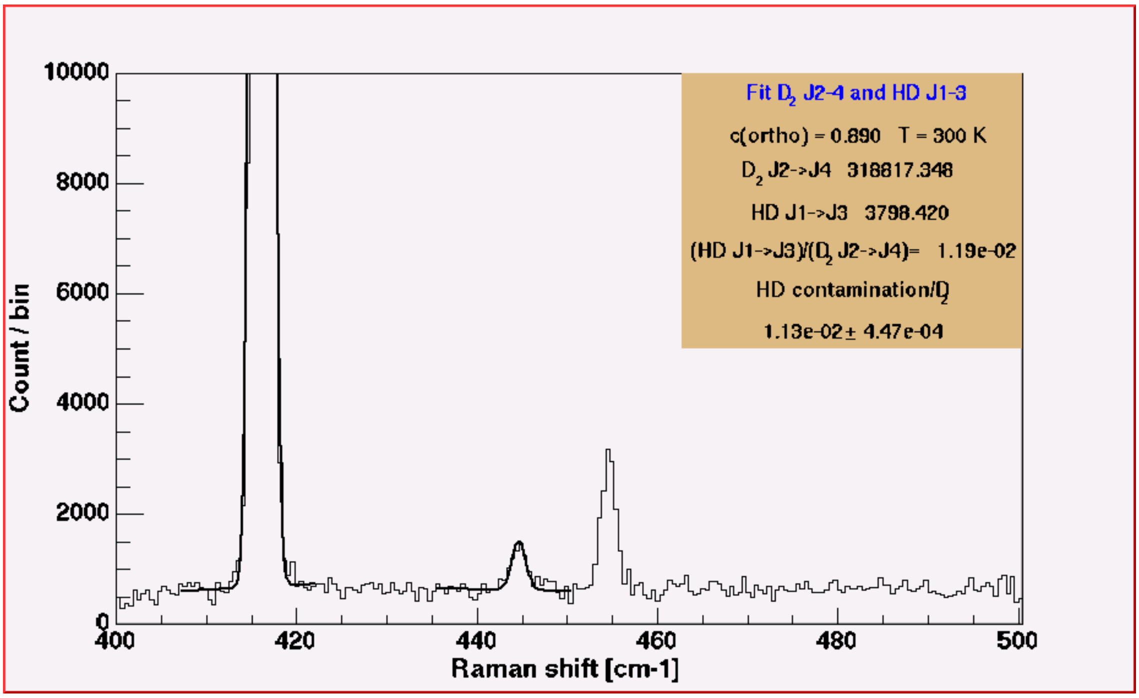

Fig. 4.24: Raman spectrum for the rotational bands of the $D_2$ gas contained HD as a contamination. The peak at 416 $cm^{-1}$ is due to the J2→J4 transition of D2, and the peak at 444 $cm^{-1}$ is due to the J1→J3 transition of HD. The 444 $cm^{-1}$ peak consists of the multi line due to the primary laser line as shown in Fig. 4.14.

The fraction of HD/$D_2$ obtained by analyzing the spectrum in Fig. 4.24 was $1.1\times10^{-2}$, which corresponds to the purification degree of 99.8%. This value is 5 times worse than the nominal specification. A typical value of the favorable purification should be larger than 99.95%, which corresponds to the neutron total cross section ratio H/D of about 0.2. With this number, the UCN lifetime is estimated to be about 550 ms. Consequently it is found that a practical UCN source is available with this purification.

## 4.3 Measurement of Ortho/Para fraction for $D_2$ irradiated in the SINQ

In order to study the effect of the radiation induced ortho/para conversion in $D_2$, a liquid $D_2$ moderator for the spallation neutron source at PSI was investigated.

### 4.3.1 Feature of SINQ

The SINQ is the Spallation Neutron Source at the PSI, Switzerland. This neutron source provides the thermal and cold neutrons with a flux of $10^{14}$ n/cm$^2$/s by using a Mega-Watt spallation neutron source operated with the 590-MeV proton beam from the PSI ring-cyclotron couples. In the SINQ, 20 liter liquid deuterium at 25 K is used as a neutron moderator, and it is irradiated with dose of 190 mW/g when the proton beam current is 1mA. More detailed information is shown in Table 4.2, and schematic view is shown in Fig. 4.25.

| Profile of SINQ Liquid $D_2$ moderator | Value |
|---|---|
| Proton Energy | 590 MeV |
| Averaged Beam Current | 927 μA |
| Averaged Beam Power | 547 kW |
| Irradiated Period | 247 days (02/04/19~02/12/23) |
| Volume of liquid $D_2$ moderator | 19.8 litter |
| Temperature of liquid $D_2$ moderator | 25 K |
| Heat Deposition to $D_2$ moderator | 176±37 mW/g/mA [13] |
| Total Dose on $D_2$ moderator in 2002 | $3.7\times10^6\pm0.79$ J/g |

Table 4.2: Specification of the SINQ and an employed liquid $D_2$ moderator.

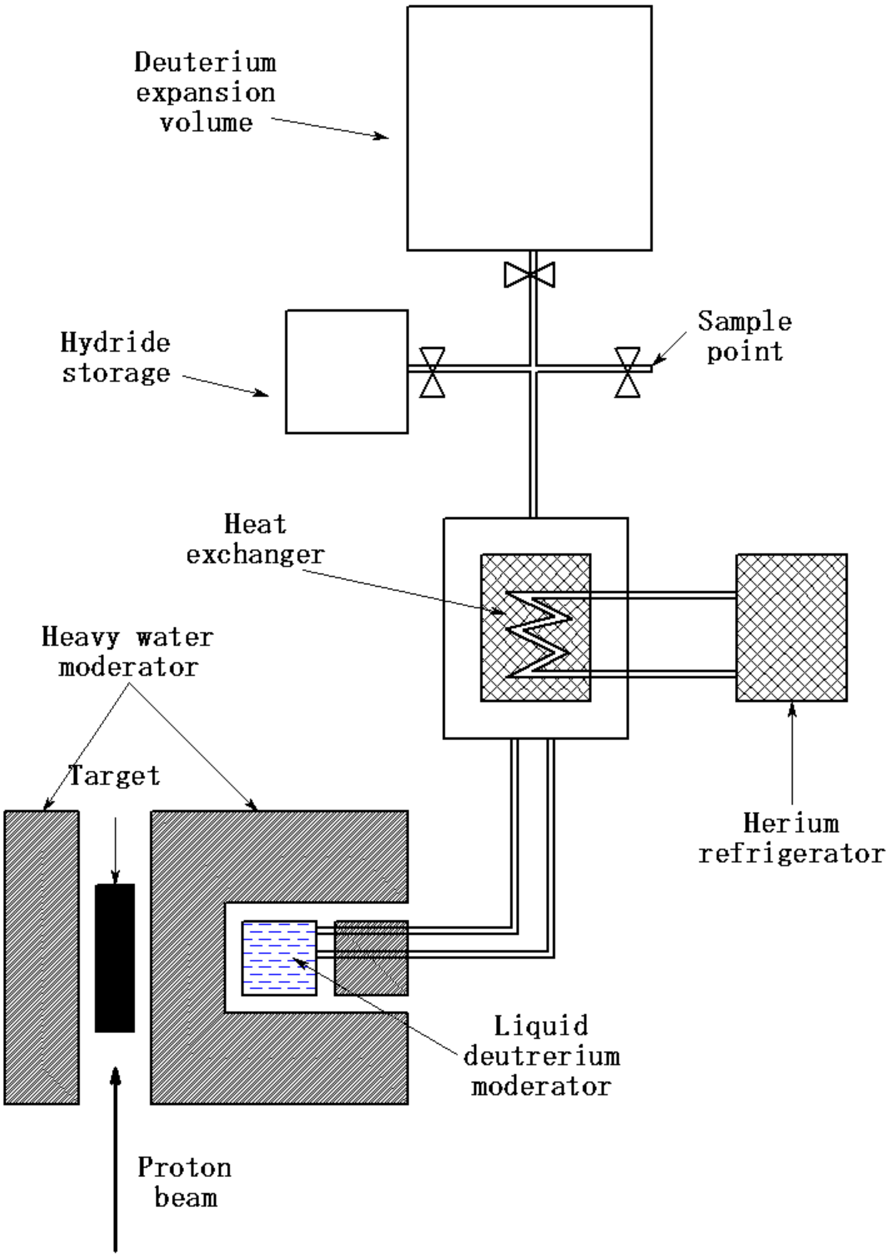

Fig. 4.25: Schematic view of the SINQ cold moderator system [56].

Fig. 4.25 is a schematic view of the SINQ cold moderator system. The 20 liter of liquid-$D_2$ moderator was set in the heavy water reflector at room temperature in order to moderate thermal neutron to cold neutron. The temperature of liquid $D_2$ moderator is kept at 25 K by helium refrigerator. The refrigerator cools evaporated $D_2$ gas of the moderator with the heat exchanger, where the mass flow between the heat exchanger and $D_2$ moderator is about 5 g/s/mA. The total cooling power is

670W/mA, 550 and 120 W/mA for $D_2$ and container, respectively. This value agreed with calculation within 20% of accuracy.

The connection from $D_2$ moderator to the heat exchanger consists of 8 m pipes of 50mm diameter, and connection from the heat exchanger to the $D_2$ expansion volume consists of 60m pipe of 90mm diameter. The $D_2$ expansion volume is about $20m^3$. The $D_2$ gas exchange rate between the expansion volume and liquid $D_2$ container can be calculate as more than 70 years so that we can ignore the effect of the expansion volume to ortho fraction of liquid $D_2$.

The experimental procedure as follows; first, $D_2$ gas was filled in a whole setup (expansion volume, cryostat and moderator) at the pressure of 280 kPa, which corresponds to 10 kg of the $D_2$ mass. Then, 20 liter (3.5 kg) of $D_2$ was liquefied in the cryostat and the produced liquid $D_2$ was flowing into the moderator container. Thus, about 1/3 of total amount of $D_2$ was in the moderator container as liquid $D_2$, and other 2/3 was stored in the expansion volume as gas. During the beam operation, the pressure of the system was kept at 150 kPa, where the density of liquid $D_2$ was $0.16g/cm^3$ at this pressure. The ortho fraction of input gas is estimated to be in equilibrium at room temperature, 0.667, because the used $D_2$ gas was kept in hydride storage for 2~3 month before using.

### 4.3.2 Extraction of $D_2$

The beam operation of the cyclotron at PSI in 2002 started on 19th Apr. and ended on 23rd Dec.. The log of beam current in 2002 is shown in Fig. 4.26. The $D_2$ from the moderator was sampled during regular service shutdowns. The sampling was done on 4th Sep 2002 and 23rd Dec 2002. The gas was sampled at a sample point (described in Fig. 4.25) immediately after the proton beam was stopped by switching off the cryostat and warming up the cold moderator. This operation was done in 2~3 hours. The gas was transferred into 40 $cm^3$ gas container made of stainless steel whose relaxation time had been measured before as described in Fig. 4.23.

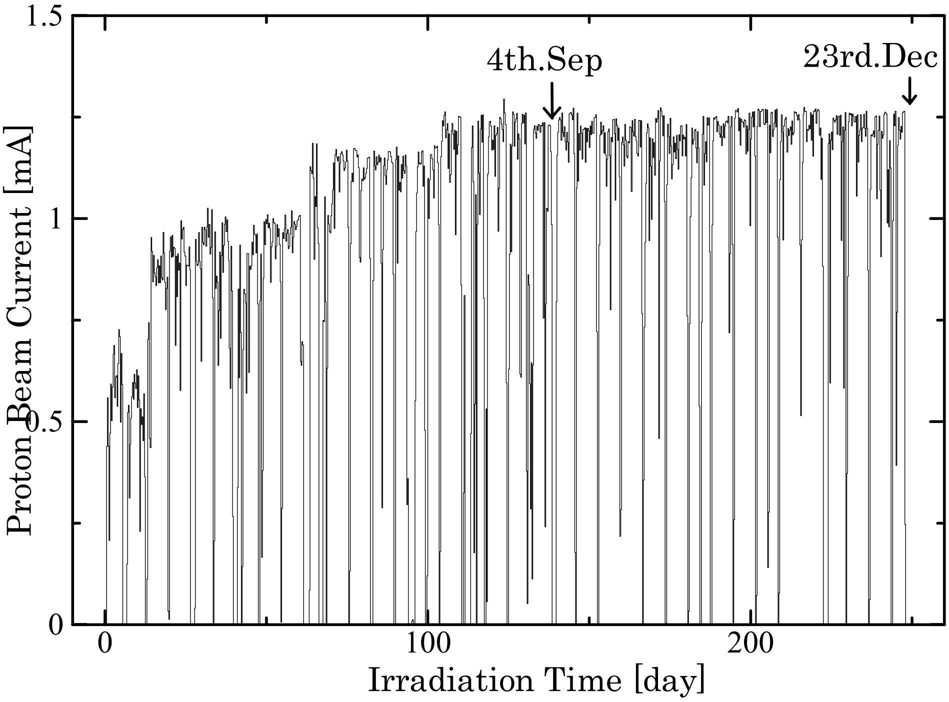

Fig. 4.26: Beam log of the proton beam on the target in SINQ during 19th Apr 2002 to 23rd Dec 2002. The arrows in this graph show sampling times performed on 4th Apr 2002 and on 23rd Dec 2002, respectively.

The sampling procedures performed on the different day were different each other. The procedure for sampling on 4th Sep is as follows. The cold moderator was warmed up slowly by switching off the cryostat in about 5 hours. Then, the evaporated gas was transferred to the expansion volume through the heat exchanger. After evaporating 15 m$^3$ of liquid $D_2$ (about 2/3 of the whole amount), the gas was sampled at the sampling point. This procedure might mix gases from the liquid moderator and the expansion volume at the sample point.

Then, the sampling procedure on 23rd Dec was improved to avoid this failure. To prevent the gas mixture in the expansion volume, a valve between the expansion volume and cold moderator was closed. Then, gases in the gas pipe, cryostat and evaporated gas from the cold moderator were withdrawn to the hydride storage to make sure that the extracted sample gas was only from the liquid cold moderator. Before the sampling, the liquid $D_2$ enough to exclude all gas in the gas pipe and cryostat was evaporated to the hydride storage.

### 4.3.3 Results

The ortho fractions of the taken-out samples were measured by the Raman spectrometer. The Raman spectra were measured at the position of spectrometer of 3000 cm$^{-1}$, and it took 20 run of 600 sec. The ortho fractions were 0.700±0.002(stat)±0.004(sys) and 0.756±0.001±0.004(sys) for the sample of 4th Sep and 23rd Dec, respectively. The first errors are statistical errors, and the second ones are systematic errors due to the analysis associated with subtraction of the background.

The spectra were taken for about 3 hours long starting on average 16 h and 12 h after sampling for the Sep. and Dec. sampling, respectively. Since from the discussion in Sec4.2.2, the relaxation time for the Raman cell was 8.4 days, the correction for the relaxation effect is estimated to be 0.003±0.002 for the Sep. and 0.006±0.004 for Dec. sampling, respectively.

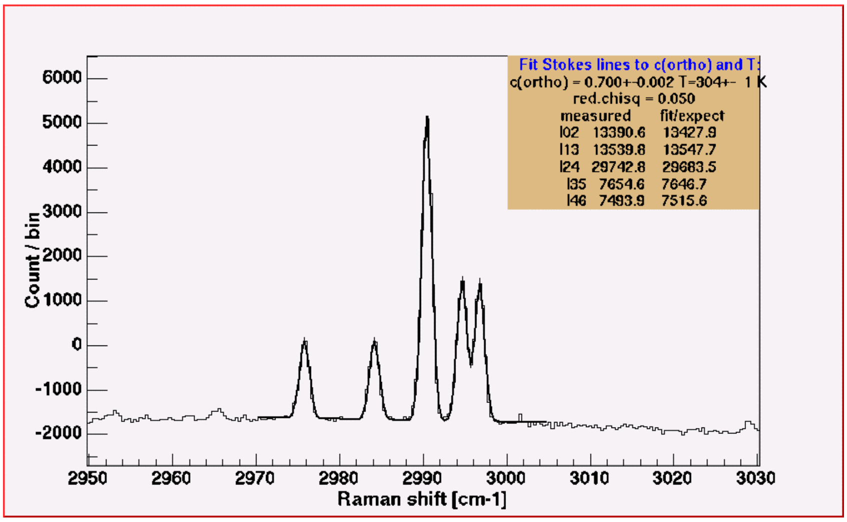

Fig. 4.27: Raman spectrum of $D_2$ taken from the SINQ at 4th.Sep.2002.

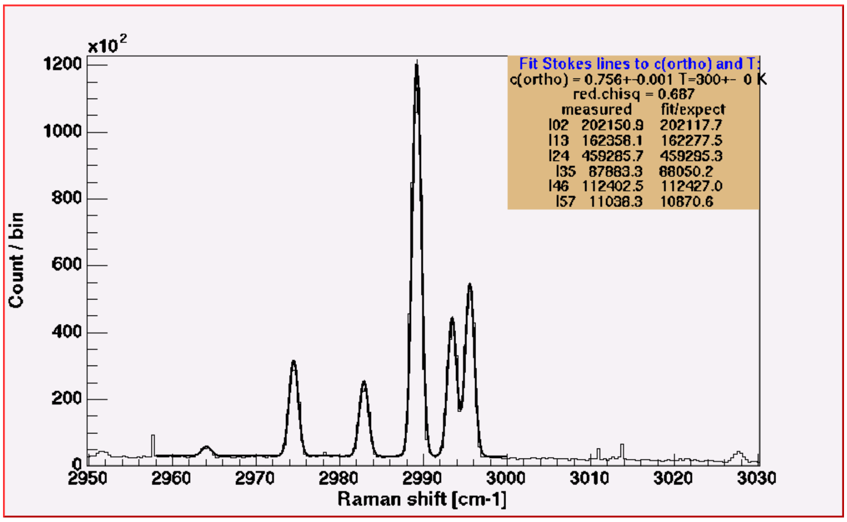

Fig. 4.28: Raman spectrum of $D_2$ taken from the SINQ at 23rd.Dec.2002.

Another systematic uncertainty may be induced from vapor pressure difference between liquid ortho-$D_2$ and para-$D_2$. According to ref.[22], the saturated vapor pressures of the ortho-$D_2$ and para-$D_2$ are given as 147.7 kPa and 143.5 kPa, respectively at T = 25 K. Therefore, first half of evaporated SINQ $D_2$ contained more ortho and last half contained more para in the gas than the liquid phase. The effects results 0±0.006 and 0±0.005 decrease for Sep. and Dec. samplings, respectively. This effect at gas-liquid equilibrium state will be discussed in Sec 5.3.1.3.

In conclusion, the ortho fractions in the liquid moderator were determined to be

$$c_o(4^{th}.\text{Sep})=0.703\pm0.002(\text{stat})\pm0.007(\text{sys}) \tag{4.23}$$

$$c_o(23^{rd}\ \text{Dec})= 0.762\pm0.001(\text{stat})\pm0.008(\text{sys}) \tag{4.24}$$

The increase of the ortho fraction from Sec. to Dec. cannot be explained by the difference of irradiation period. The small ortho fraction of 4th Sep. sampling might be due to the unexpected mixture of the $D_2$ gas in the expansion volume. The further interpretation of these results is discussed in Chapter 6.

# Chapter 5 Experiment at KURRI

The time differential measurement on the conversion from the ortho to para $D_2$ due to the irradiation is described in this chapter. This measurement was performed at the KURRI, Kyoto University by using a 33-MeV electron linac. The motivation of this study is to more reliably investigate an irradiation effect on the conversion of the ortho to para $D_2$ states in comparison with the measurement at the PSI where the time integrated measurement was done for liquid $D_2$ samples. To simulate the measurement at the PSI, liquid ortho $D_2$ samples produced by a catalyst, $CrO_3$ were also used at the KURRI. In order to obtain the reliable ortho/para ratio as a function of time we paid a particular attention on the measurement of the parameters sensitive to the ortho/para conversion, for example, the temperature rise of the sample cell, the species (neutron, gamma), and strength of the radiation, the thermal conversion rate, the conversion due to the wall of sample cell, and so on. The irradiated samples ($D_2$ gas) were transported to the Laser laboratory at Department of Physics, Kobe University and the ortho/para ratios were successfully measured by means of the Raman spectroscopy under a guide of Prof. Fukuda and Kohmoto.

For enabling the above investigation, we designed and constructed a cryostat to produce a liquid $D_2$, a target to generate the gamma rays, collimator, shield, etc.

In Sec. 5.1 and 5.2, the experimental apparatus and procedures are described respectively. The experimental results and their analysis are given in Sec. 5.3 and 5.4, respectively.

## 5.1 Apparatus

The measurement has been done at the Kyoto University Research Reactor Institute (KURRI). A 33-MeV electron beam from the electron linac was incident on a thick tantalum target. The maximum repetition rate of electron beam pulse is 100 Hz. Forward peaked strong gamma-rays mainly due to the Bremsstrahlung and relatively weak neutrons with a nearly isotropic angular distribution were produced from the tantalum target. These radiations were incident through a tungsten collimator on a liquid deuterium stored in a sample cell of a cryostat located close to the tantalum target. Before the liquid $D_2$ was exposed to the radiation, the purified ortho $D_2$ had been fabricated in advance. Then, the liquid $D_2$ was irradiated with a period of a few days for each sample. During a period of irradiation, the electron beam was interrupted several times within every 12~24 hours and the irradiated $D_2$ samples were extracted The sample extraction processes have been done as follows; the irradiated liquid $D_2$ sample was gasified, the gas sample was, then, collected by a stainless vessel.

The collected gas samples were measured by the Raman spectrometer at the Department of Physics, Kobe University. Meanwhile, radiation fluxes due mainly to gamma rays with some admixture of neutrons were measured by the activation analysis using Au and Ni foils. The evaluation of the total fluxes at the beam-on time was done by an independent measurement with a period of 30~60 min. in advance of the irradiation measurement.

The experimental layout of the experimental setup including the beam line, target, and cryostat is shown in Fig. 5.1. The further detail of the experimental apparatuses is described in the subsections.

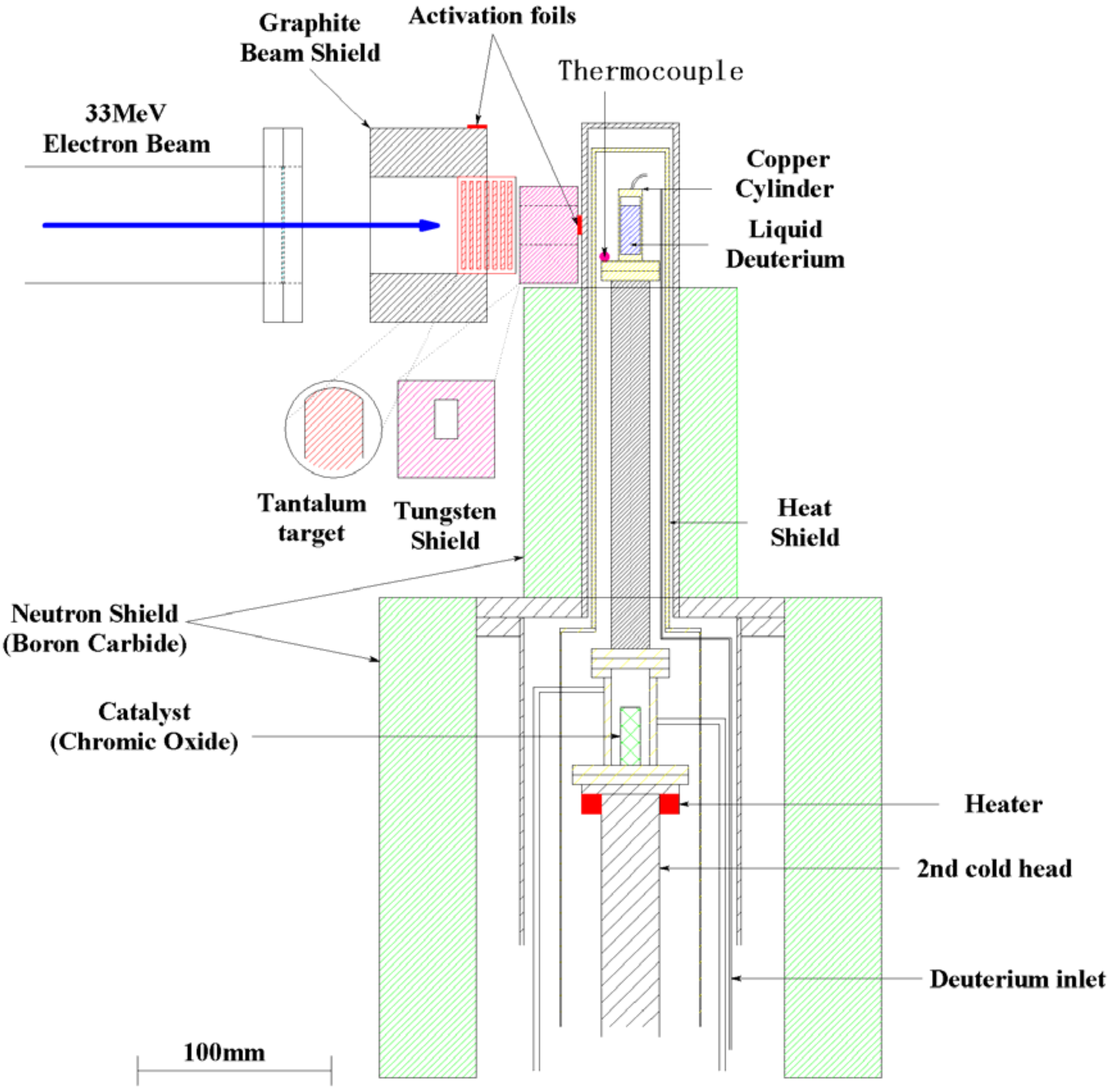

Fig. 5.1: Layout of the experimental setup

## 5.1.1 Electron Linac

The experiment has been done by using the linac in the KURRI. The characteristics of the electron beam are shown in Table 5.1. The beam spot size and the position on target were checked by observing transcribed spot shapes on a plastic sheet before the irradiation experiment was started. So that the beam position may be a flange center attached in the end of the beam tube. In fact, we could determine the beam position with an accuracy of 2 mm, and the spot size (spot diameter) was 12 mm with a 30-mm halo structure. An example of the beam spot transcribed in Fig. 5.2.

| Beam Energy | 33 MeV |
|---|---|
| Pulsed beam current | 0~500 mA |
| Pulse width | 10 nsec ~4 micro sec |
| Pulse period | 0~100 Hz |
| Average beam current | 0~200 micro A |
| Beam power | 0~6.2 kW |

Table 5.1 Characteristics of the electron beam from the Linac at the KURRI

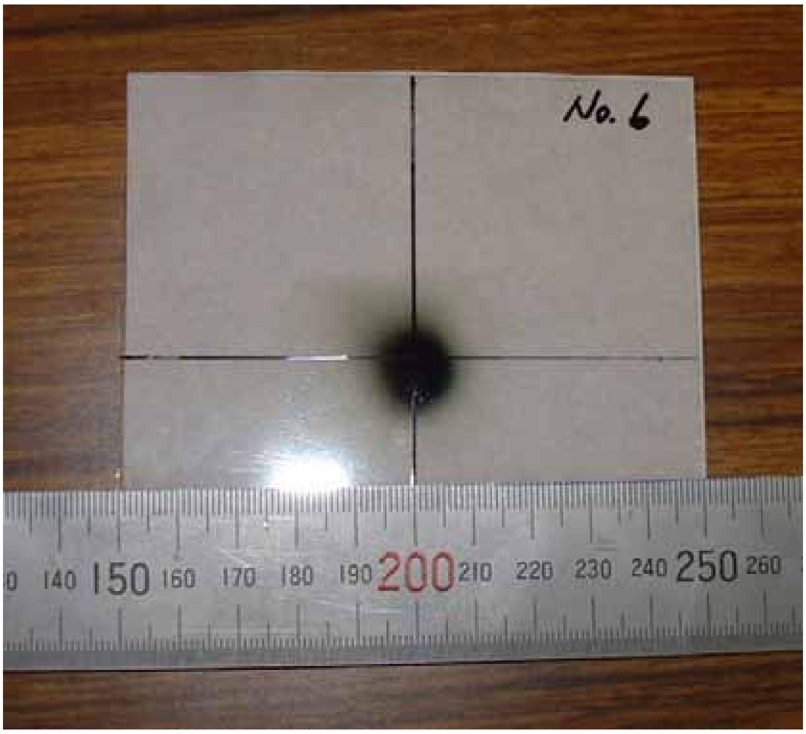

Fig. 5.2: Photograph of the electron beam spot at the position close to the tantalum target taken by an acrylic sheet. The beam spot had about 15 mm diameter.

On the other hand, the electron beam energy distribution was determined by measuring its momentum distribution using a bending magnet with a bending angle of 45°. Fig. 5.3 is a momentum spectrum of the 39 μA of electron beam measured by changing an electric current of the bending magnet, where the peak energy corresponds to 32.8 MeV. From this result, the energy spreading (FWHM) of the electron beam is about 1.6 MeV. The beam energy is known to decrease when beam current increases.

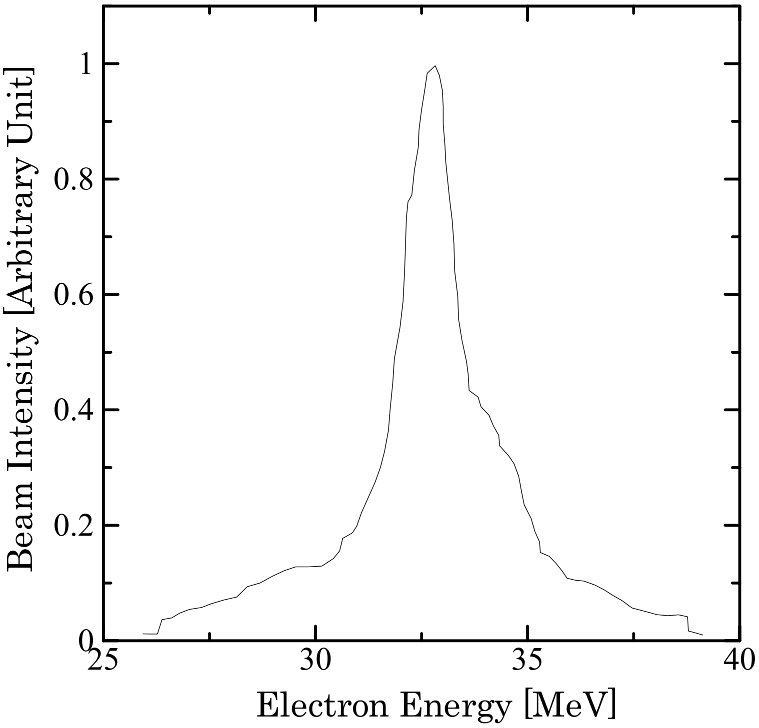

Fig. 5.3: Energy spectrum of the electron beam measured by a bending magnet.

### 5.1.2 Target, Collimator and Shield for irradiation

Generally speaking, a heavy element is suitable for production of gamma rays with a high intensity. On the other hand, as described in Table 5.1, an available maximum power of the electron beam is 6.2 kW. In conclusion, a tantalum (Ta) was employed as a suitable target material because of its high melting point, i.e., 2996 °C. Two targets were used in this experiment. One has the 29 mm thickness used in ref. [57], which is shown in Fig. 5.4, the other is new made target with 15 mm in order to optimize gamma arriving to the sample. The schematic setup of the 15mm tantalum target is shown in Fig. 5.5. The Ta target consists of 10 layers of tantalum sheets with each gap of 1.5 mm in order to avoid the local concentration of the heat load and to increase efficiency of water-cooling. Among the 10 Ta sheets, thicknesses of the former 5 Ta layers were 1mm, while thicknesses of the latter 5 layers were 2 mm because the electron beam with a higher energy produces a higher energy loss in the target at the electron beam energy region of 30 MeV. The target housing made of titanium (Ti) was designed and fabricated according as ref. [57].

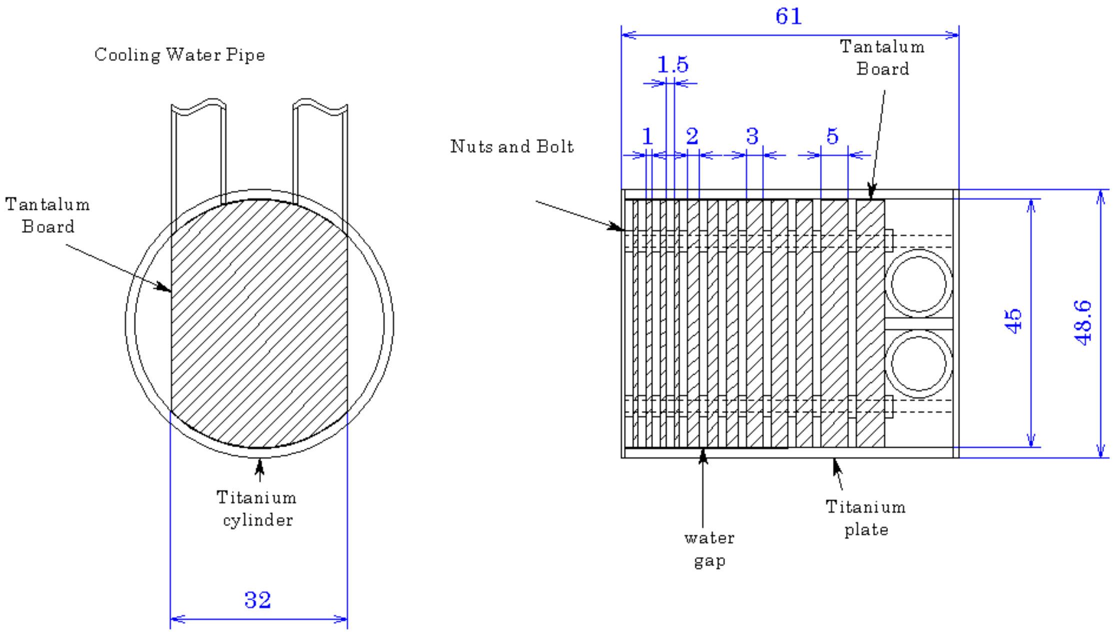

Fig. 5.4: Front and side view of Cross section of the 29 mm thick Ta target[57].

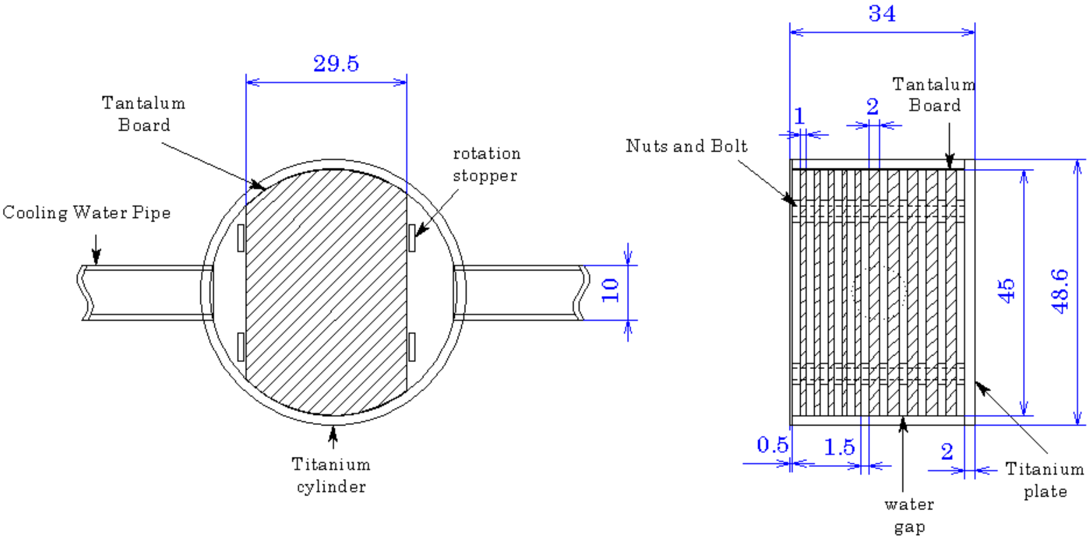

Fig. 5.5: Front and side view of Cross section of the Ta 15 mm thick target.

The gamma rays produced from the Ta target gives heat loads not only on the sample liquid $D_2$ but also on a peripheral part of the cryostat including the sample cell. In particular, an attainable lowest temperature is restricted by the heat deposit on the top end part of the cryostat including the sample cell itself. Therefore, in order to keep the cell temperature as low as possible, a tungsten-alloy collimator was inserted between the Ta target and the cryostat thus reducing unnecessary heat deposit on other parts of the cryostat except for the sample cell. The collimator design is illustrated in Fig. 5.6. The tungsten alloy is made of 94% tungsten, 4% nickel and 2% Cu in weight percent, and the density of the alloy was 17.9 g/cm$^3$. The collimator was constructed by assembling rectangular rods, and it had a 12×20 mm hole, through which the gamma rays could pass.

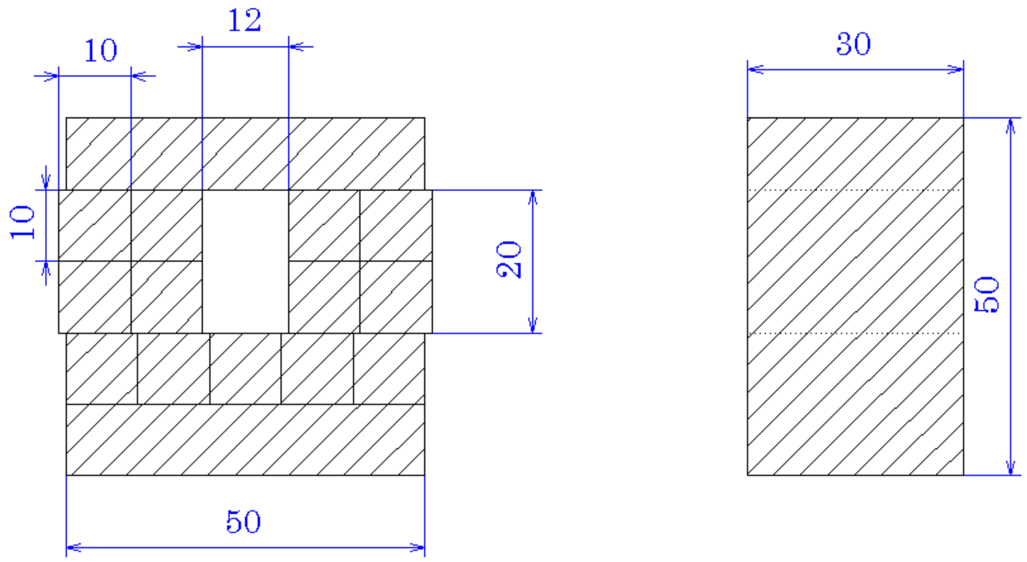

Fig. 5.6: Tungsten alloy collimator. Unit of the scale is mm. The gamma rays can pass through the central hole with 12×20 mm.

In order to avoid activation by the gamma rays and neutrons, lead blocks, polyethylene blocks, and Al bottles filled with $B_4C$, covered an entire body of the mechanical part of the cryostat and a upstream part of the cold heads and a cylindrical Al vacuum chamber with a thickness of 0.5 mm used for the gamma ray window as shown in Fig. 5.7 and Fig. 5.8. The detailed description of the cryostat will be discussed in the next section.

Fig. 5.7: Cryostat shielded by $B_4C$ and lead. In the center of the shield an Al window for the gamma rays is seen. Polyethylene blocks are removed.

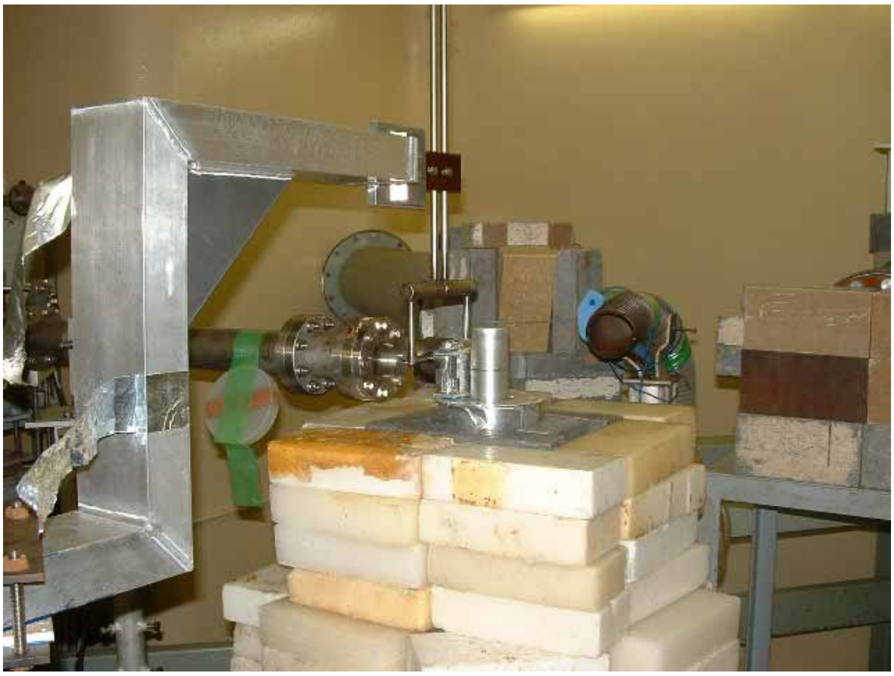

Fig. 5.8: Picture of a whole setup. Beam window, Ta target, tungsten alloy collimator, cryostat, and radiation shield are seen. The sample cell for liquid $D_2$ was set in the top part of the Al cylinder.

### 5.1.3 Cryostat and sample cell

A detail description of the cryostat system is shown in Fig. 5.9. A 2-stage Gifford-McMahon (GM) cryostat (Iwatani-D501) is used for this purpose. In a thermally insulated vacuum chamber, 2 copper cells are positioned on the 2nd stage of cold head. One cell is used to produce a purified ortho deuterium by means of a catalyst. An aluminum cell with a shape of cylinder shape is filled with a catalyst, Oxisorb®, consisting of silica grain coated with $CrO_3$. The grain size is about 50 μm. Another cell, sample cell for the liquid $D_2$ is exposed in the radiation atmosphere. The cell has ϕ10×30mm inner volume with 1mm wall thickness. To prevent the cryostat from activation, the sample cell is positioned 32cm apart from the catalyst cell, between which is thermally connected with a copper rod with a 15 mm diameter. A copper heat shield surrounding these cells prevents the black body radiation from the inner surface of the vacuum chamber at room temperature.

Two sets of thermometers consisting of a chromel-gold thermocouple are attached on each cell. The liquid nitrogen temperature was employed as a reference temperature of the thermocouples. The cryostat temperature is controlled by Chino DB1000 temperature controller with a heater with a specification of 30 W, and 30 Ohm. The temperature stability for both cells, thus obtained, was about 0.1 K. On the other hand, the temperature calibration of thermometers were done by comparing the deuterium pressure, since there was approximately 0.5 K deviation for the nominal values of the thermometers. The overall accuracy of the temperature measurement was about 0.2 K. Fig. 5.10 shows an experimental result of the temperature at the catalyst cell obtained by varying the cooling power.

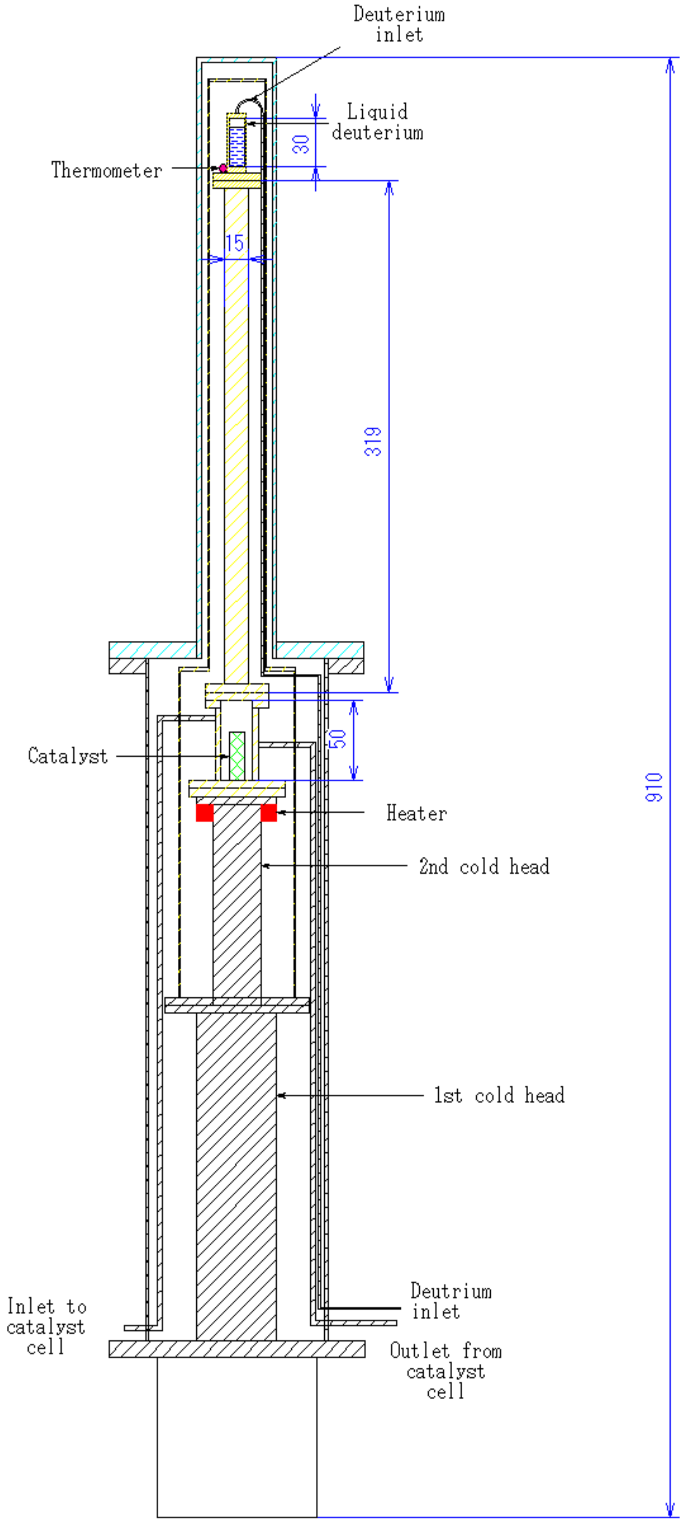

Fig. 5.9: Cross sectional drawing of the cryostat.

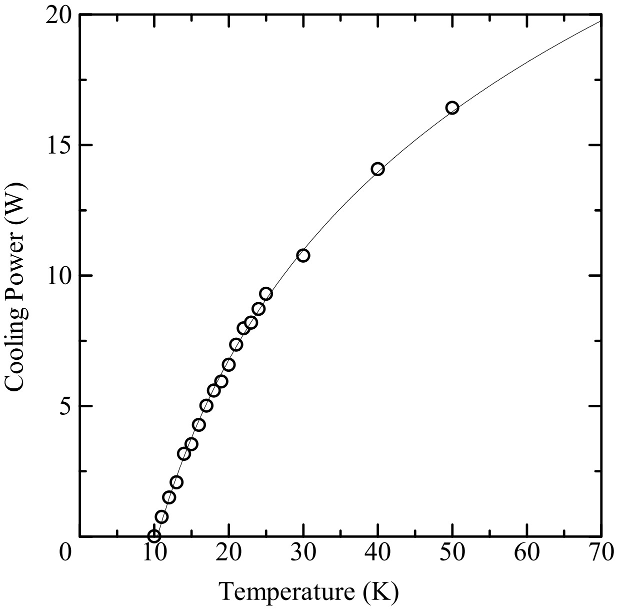

Fig. 5.10: Temperature at the catalyst cell vs. cooling power of the cryostat. The dotted curve is drawn only for eye guide.

### 5.1.4 Catalyst and gas line

The catalyst to convert ortho/para was insert in cell where is just top of 2nd stage of cryostat (catalyst cell). The catalyst (OXISORB®[48]) was fully stored in ϕ19×30 mm aluminum cylinder. The mass of catalyst was 3.6 g.

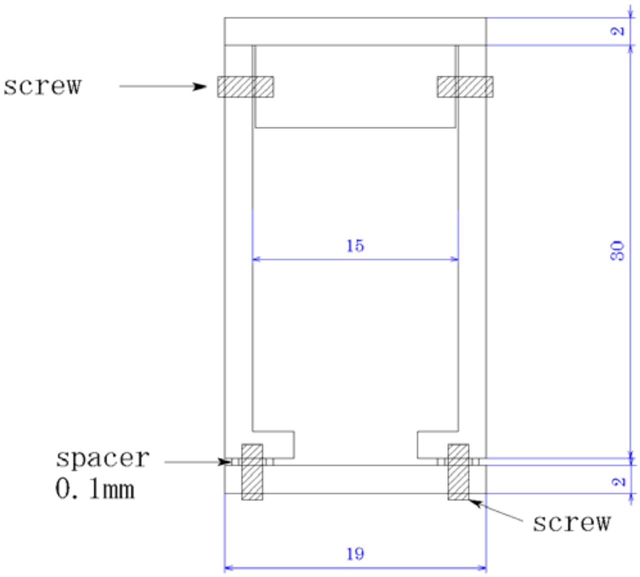

Fig. 5.11:The side view of catalyst cartridge.

A schematic view of the gas feed line is shown in Fig. 5.12. The cryostat itself was located in the experimental room, and it was connected to other equipments located in the counting room through the thick radiation protection wall. The gas line was made of stainless steel with swage swagelok®[58] connections. A major part of the gas line was made by 1/4” stainless pipes, while piping between the experimental room and counting room was done by 4mm stainless pipes. Bourdon gages measured gas pressures in a range of 0 to 400 kPa.

The connections to the gas line, sampling port, evacuation port, and gas inlet, were made by NW25 quick couplings. In case of sampling of $D_2$, a stainless bottle with 50 $cm^3$ was attached to a sampling port, and a sample gas was extracted to the bottle after evacuate the gas in the bottle up to $10^{-4}$ mbar. Two reservoir bottles with 1-liter volume were set in the counting room, and used to reserve gas.

2~3 liter STP $D_2$ gas was used in the course of the present experiment. The $D_2$ sample cell and the catalyst cell have relief valves between vacuum insulation and closest valves, and the relief valves were set to open at absolute pressure of 0.4 MPa. The vacuum insulation of the cryostat was evacuated to $10^{-5}$ mbar and the pressure decreased to $10^{-6}$ mbar at 20 K due to the cooling.

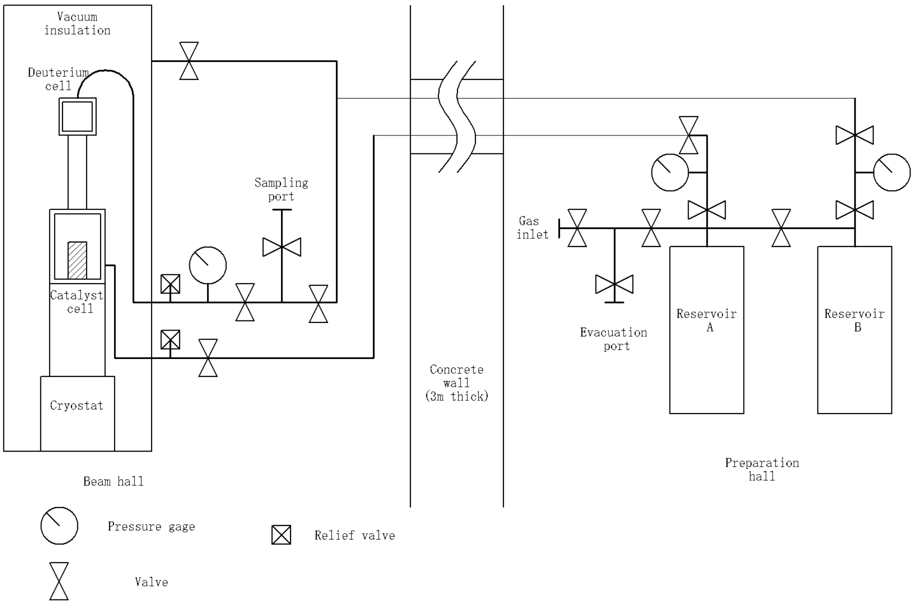

Fig. 5.12: Scheme of gas line. Gas lines drawn by a thick line corresponds to pipelines with an outer diameter of 1/4 inch, and thin lines correspond to pipelines with an outer diameter of 4 mm.

### 5.1.5 Raman spectroscopy

Setup of the Raman spectrometer at the Dept. of Physics, Kobe University is shown in Fig. 5.13. A couple of spectrometers were used as a double monochrometer to reduce the Rayleigh scattering.

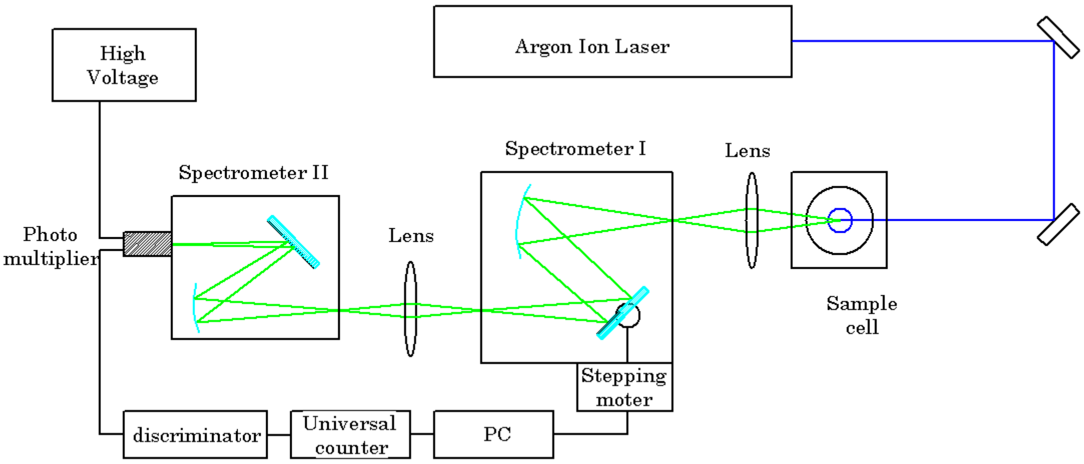

Fig. 5.13: Schematic top view of the Raman spectrometer at the Dept. of Physics, Kobe University.

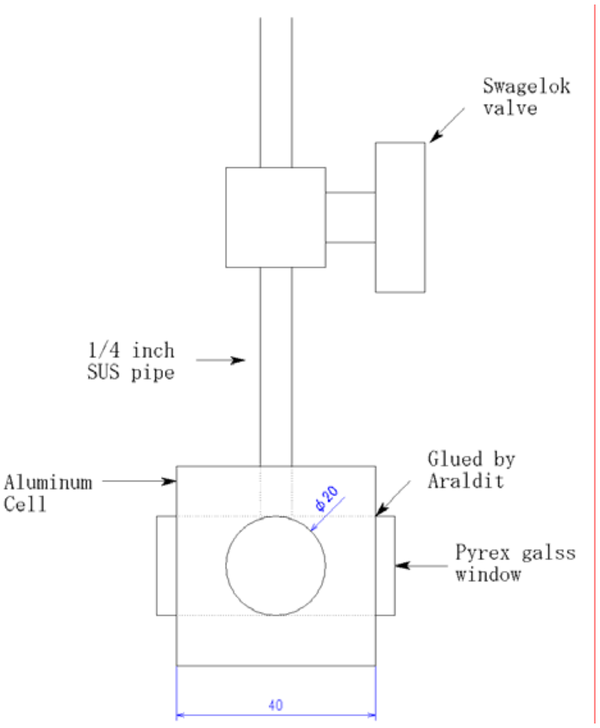

Fig. 5.14: Sample cell made of aluminum used for the Raman spectroscopy. The four windows are made of Pyrex glass. The inner volume is 21 cm$^3$.

| Laser | Ar ion laser (Cohelent innova300) |
|---|---|
| Laser wavelength | 514.5 nm |
| Laser power (single) | 5.7 W |
| Spectrometer I | Ritsu Oyo Kagaku MC25N grating monochrometer |
| Spectrometer II | Ritsu Oyo Kagaku MC10N grating monochrometer |
| Detector | Photomultiplier Hamamatsu R585S |
| Counter | Hewlett packard 53131A universal counter 225MHz |

Table 5.2: Specifications of Raman spectrometer.

An Argon ion laser having a maximum power of 9.8 W (all lines), was used in the present Raman spectroscopy. This laser shoot multi lines, whose wavelengths are mainly 488.0 nm and 514.5 nm with power ratio of 4 : 6 at the maximum power. 514.5 nm was selected for the present spectroscopy to avoid the Raman lines scattered by 488 nm overlapping the region of present interest.

The spectrometers are working as a double spectrometer facilitated in preventing the Rayleigh scattering. The light passing through the spectrometer I was focused onto the spectrometer II by a lens, and was led to a photoelectric surface on the photomultiplier used as a photon detector. The wavelength of the spectrometer I could be changed by changing a grating angle with a stepping motor controlled by the PC. However, the wavelength setting of the spectrometer II was fixed at the definite position, the wavelength acceptance was enough broad to accept major parts of the rotational bands for the $D_2$.

This spectrometer used in the present measurement is similar to one developed at the PSI (See Sec. 4.1) with a minor difference as discussed below. The primary difference is a used laser power. The laser power at the Dept. of Physics, Kobe University has over 100 times larger than the PSI's. The second difference is a detector; CCD at the PSI and photomultiplier at the Dept. of Physics, Kobe University. CCD allows a simultaneous measurement of the different wavelength. On the other hand, a merit of photomultiplier is as follows; a photomultiplier is free from the cosmic ray background because one cosmic ray makes only one count at most. The third difference is a light pass length. Since the Kobe's setup uses a shorter pass length, the resolution becomes worse than the PSI's. Note that the best resolution of the Kobe's spectrometer is 10 cm$^{-1}$. Because of this worse resolution, we used the rotational bands for the ortho/para states.

The Raman spectrum (rotational band) of normal $D_2$ at room temperature taken at the Dept. of Physics, Kobe University is shown in Fig. 5.15. This spectrum was obtained by measuring a $D_2$ gas reference sample, which contents 94kPa of normal $D_2$ gas in glass vessel. A small peak accompanied with the J0→2 peak, which might be caused reflection in the spectrometer. The small peak was subtracted by analysis.

Because of wavelength dependence of the reflection and detection efficiencies of spectrometer, the count rate for peaks of each rotational band should be calibrated. For this purpose, observation of the rotational band for $D_2$ at room temperature was performed, since the ortho/para ratio is exactly 2:1.

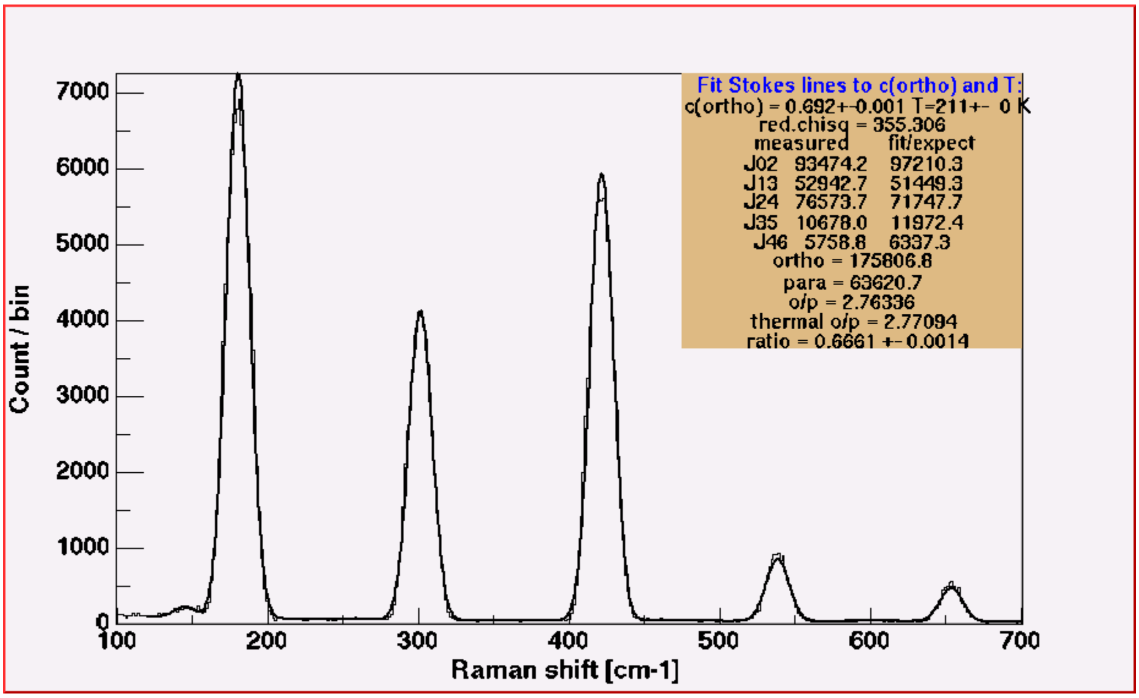

```
Fit Stokes lines to c(ortho) and T:
c(ortho) = 0.692+-0.001 T=211+-  0 K
red.chisq = 355.306
measured      fit/expect
J02  93474.2   97210.3
J13  52942.7   51449.3
J24  76573.7   71747.7
J35  10678.0   11972.4
J46   5758.8    6337.3
ortho = 175806.8
para = 63620.7
o/p = 2.76336
thermal o/p = 2.77094
ratio = 0.6661 +- 0.0014
```

Fig. 5.15: A typical Raman spectrum (rotational band) of normal $D_2$ at room temperature taken at the Dept. of Physics, Kobe University.

### 5.1.6 Activation analysis

For activation analysis, a germanium detector at the KURRI "Hotlab" was used to measure gamma rays. A whole setup of the detection system is shown in Fig. 5.16. A germanium detector GEM-30185 (ORTEC) was set in a 5cm lead shield that was covered by a 5mm oxygen free copper. Activation foils activated by the radiation were set 15 cm apart front the germanium detector to obtain favorable counting rates.

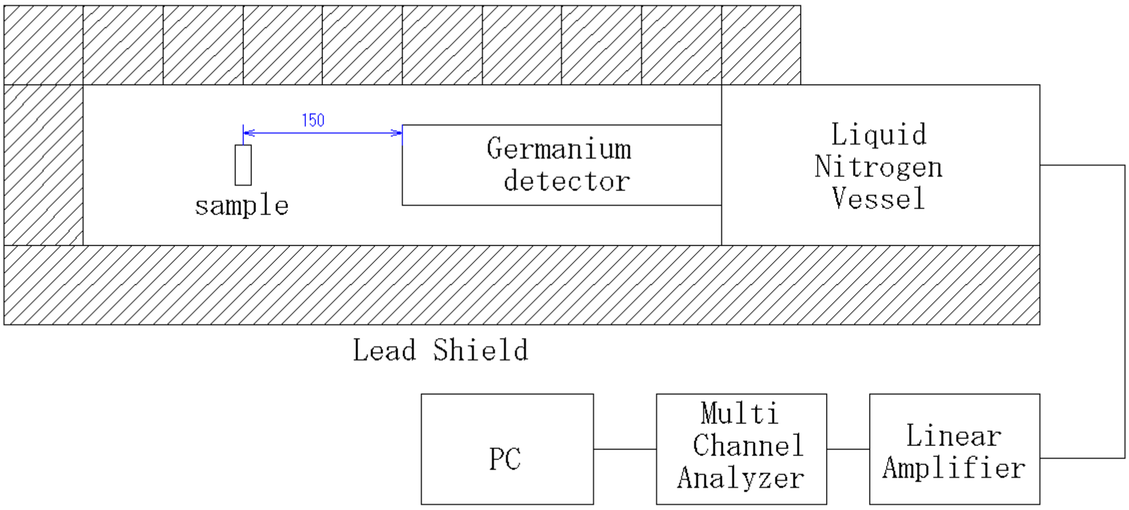

Fig. 5.16: Schematic layout of the activation analysis.

The detector efficiency had been determined with several radio-isotopes whose gamma-rays are known as reference sources, whose contents are shown in Table 5.3. The samples were set at 150 mm front of the detector. The reference of mixed isotopes is measured 20000 sec to determine efficiency of the detector before using activation analysis. The spectrum of reference source is shown in Fig. 5.17. The efficiencies can be fitted by a function of

$$f(E) = p_1 \times E^{p_2} \tag{5.1}$$

From the fitting, the parameters, $p_1$ and $p_2$, were deduced as 0.32±0.0087 and –0.82±0.0040, respectively. The energy resolution of the detector was about 3keV.

| Radionuclide | Gamma-ray energy [keV] | Half life [day] |
|---|---|---|
| $^{109}$Cd | 88.03 | 462.4 |
| $^{57}$Co | 122.1 | 271.79 |
| $^{139}$Ce | 165.9 | 137.64 |
| $^{203}$Hg | 279.2 | 46.612 |
| $^{113}$Sn | 391.7 | 115.09 |
| $^{85}$Sr | 514 | 64.84 |
| $^{137}$Cs | 661.6 | 10,983 |
| $^{88}$Y | 898 | 106.65 |
| $^{60}$Co | 1173 | 1,925 |
| $^{60}$Co | 1333 | 1,925 |
| $^{88}$Y | 1836 | 106.65 |

Table 5.3: The reference radionuclide used for the activation analysis

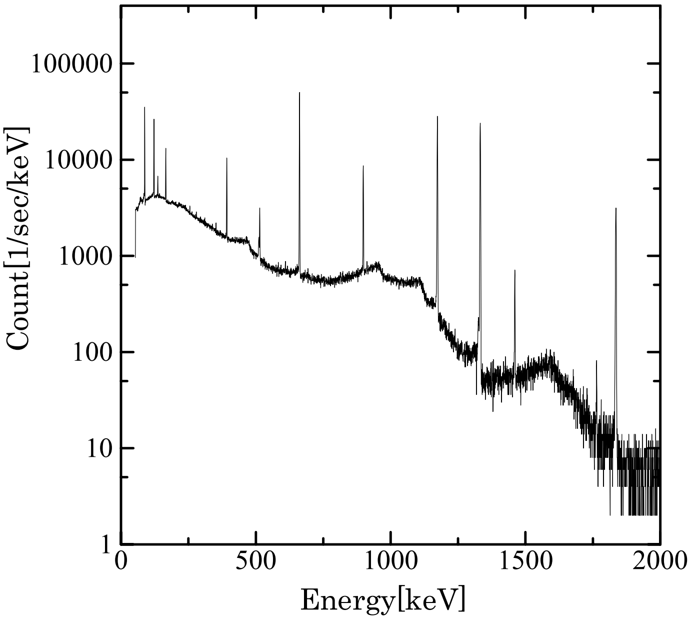

Fig. 5.17: Spectrum of the reference mixed gamma source. The measurement period was 20000 sec.

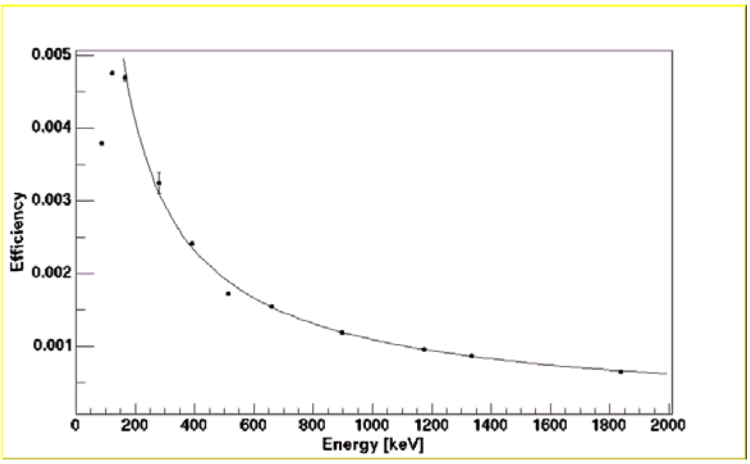

Fig. 5.18: Measured gamma ray efficiencies plotted against the gamma ray energy. The solid line is a fitting curve assuming a function described by eq. (5.1) in a gamma-ray energy range from 160 to 2000 keV.

## 5.2 Experimental procedure

In this experiment, about 2 cm$^3$ of liquid deuterium, which have been concentrated to 98% ortho by cooling with catalyst, was irradiated by radiations produced by exposure of 30 MeV electron beam to a tantalum target. In order to measure the ortho fraction in the liquid deuterium, about 70 cm$^3$ STP gas was extracted from the irradiated deuterium 1~2 times in a day. The extracted samples of irradiated $D_2$ were transported to the Dept. of Physics, Kobe University to measure ortho/para ratio by the Raman spectroscopy. For transportation and storage of the samples were kept in 50 cm$^3$ SUS bottles, and all Raman measurements have been done within 3days from extraction so that the conversion from the ortho to para $D_2$ due to the wall and molecular collisions is negligibly small. In fact, this condition was experimentally proven: the bottles were flushed by helium and deuterium 5 times each, then the relaxation times of deuterium were more than 170 days (immeasurably long).

### 5.2.1 Preparation of purified ortho $D_2$

Here we present a detailed description of the procedure on the experiment at the KURRI. Firstly, $D_2$ gas was charged from a $D_2$ cylinder (40 liter, 15MPa) to a reservoir bottle (1liter, 400 kPa). Charged $D_2$ volume was about 4 liter at STP. The gas purity is 99.5%, and a major part of the impurity is considered to be $H_2$. Next, $D_2$ gas was transferred from the reservoir bottle to the catalyst cell in cryostat that was cooled to 20 K. The $D_2$ was kept for 6~18 hours at 20 K to convert ortho rich $D_2$, where cooling time with 2 hours is enough to equilibrate the ortho/para ratio. A valve between the 1 liter reservoir and catalyst cell was opened. The pressure of reservoir was 30 kPa, which corresponds to the saturated vapor pressure of $D_2$ at 20 K[22]. The setting temperature 20 K and the equilibrium ortho fraction at 20 K from eq. (3.15) is 98.0%. The speed of catalyzing conversion is critically slower in solid phase than liquid phase because of decrease of the diffusion constant at solid phase. Therefore, the condition that the temperature is low but $D_2$ stays in liquid phase is favorable. This condition is realized at the triple point of D2, i.e., 18.7 K. In our work, we set the temperature at somewhat higher than the triple point, 20 K, in order to make sure that $D_2$ in the catalyst cell is completely in liquid phase. Another reason, though it is somehow trivial, why we set the temperature at 20 K is as follows; since we used an uncalibrated thermometer with an error of a few K, we should have set the temperature on the safety side, i.e., 20 K.

After cooling several hours, the equilibrated $D_2$ was extracted and stored in the reservoirs. For this purpose, liquid $D_2$ at 20 K in the catalyst cell was gasified. Since the temperature rise of the catalyst cell is accompanied with conversion of ortho to para $D_2$ the extraction process should be done in a short period. However, since according to the temperature rise, the vapor pressure was increasing slowly toward the saturation vapor pressure, the time needed for the pressure to get equilibrated was about 10 minutes.

Another problem occuring in the course of the gas extraction procedure is an adsorption to the catalyst. This effect works in reducing the ortho fraction of $D_2$ in the extraction process without careful gas handling. This is discussed below.

It is well known that the catalyst works as an adsorptive material of gases. As a matter of fact, we could extract only 1.5 liter of $D_2$ (76 kPa in the 2 liter reservoir) out of an initial 2.6 liter $D_2$ in our measurement. The deficit of of $D_2$ was considered to be adsorbed by the catalyst. When the temperature of the catalyst cell arose, most of the adsorbed $D_2$ gas was released at about 80 K. The ortho fraction of $D_2$

gas released from the catalyst was reduced to 71% because of high temperature catalytic effect. To reduce mixture of such high temperature component we collected only a component gasified at 24~25 K, which had the ortho fraction of 98%.

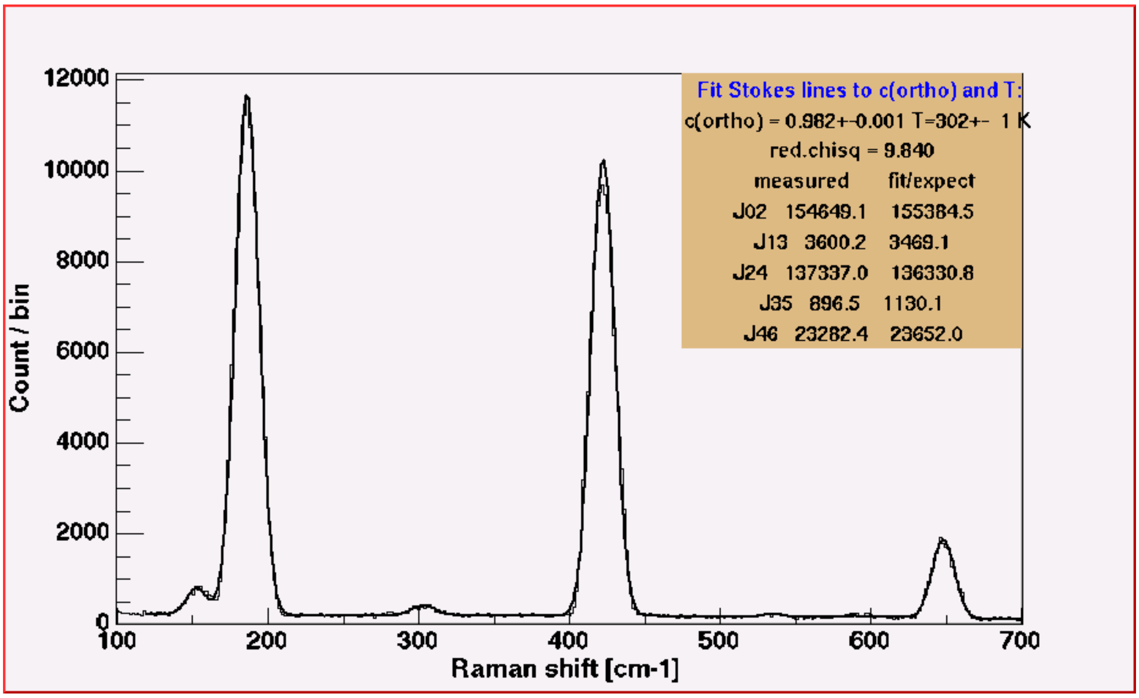

Fig. 5.19: Spectrum of the rotational band for the purified ortho $D_2$.

### 5.2.2 Irradiation

A whole experimental setup is shown in Fig. 5.1 and their pictures are shown in Fig. 5.7 and Fig. 5.8. The 33-MeV electron beam bombarded the tantalum target to generate the radiations mainly composing of the gamma rays and neutrons. A purified ortho deuterium (initially the purification is 98.0%, see Sec5.2.1) cooled at 20~25 K in the irradiation (sample) cell was exposed to the radiations from the Ta target. An amount of the deuterium in the irradiation (sample) cell was about few $cm^3$ as liquid. The conditions of all runs are shown in Table 5.4.

| Run Number | Irradiation period [day] | Total Charge [C] | Mean beam current [μA] |
|---|---|---|---|
| A | 1.46 | 21.2 | 168 |
| B | 3.88 | 11.6 | 34.6 |
| C | 2.36 | 7.3 | 35.8 |
| D | 2.14 | 10.4 | 56.2 |

| Run Number | Sampling number | Sample amount [liter STP] | Temperature [K] | Ta target Thickness |
|---|---|---|---|---|
| A | 2 (+2 after Irradiation) | 1.3 | 25.4±0.4 | 29mm |
| B | 5 | 2.2 | 24.9±0.4 | 15mm |
| C | 4 | 1.9 | 19.7±0.3 | 15mm |
| D | 5 (+1 after Irradiation) | 2.0 | 24.8±0.4 | 15mm |

Table 5.4: Irradiation conditions of all runs.

During the irradiation, the temperature of irradiation cell, the inside pressure, and the heat load were measured. The temperature was controlled at constant by controller module, but it varied about 0.4 K due to the temperature dependence of the module. The vapor pressure of liquid $D_2$ followed the temperature of irradiation cell. In the experiment with the electron beam energy of 1.3 kW (run B), an electric heater wound around the 2nd stage decreased from 7.6 W to 5.0 W, which means that the heat load of 2.6 W on the cryostat.

The exposed deuterium sample was gasified and extracted to the 50 $cm^3$ SUS304L bottle. Only in case of run C, the temperature was increased from 22 K to 25 K to increase the pressure of sample gas; the sample pressure was about 150 kPa. To remove the gas remaining in the extraction tube (the volume less than 10 $cm^3$), a first 20 $cm^3$ was evacuated. Extraction has been done 1 hour after stopping the electron beam due to the radiation protection for the sampling procedure. In run A and D, 1 or 2 sample were taken after the end of the irradiations to check the “beam off” process. At most, 6 samples were taken with the pressure of 150 kPa. It corresponds about 20% of whole amount.

### 5.2.3 Evaluation of the irradiated dose

Irradiated doses (due to mainly gamma-rays with small mixture of neutrons ) for liquid $D_2$ samples are important parameters in the present work. These parameters were determined by the measurement using the method of foil activation analysis in association with the gamma-ray energy spectra calculated by the Monte Carlo simulation code, Geant4.5[59].

The yield, $Y_0$ measured by the Ge detector for a specific gamma-ray transition in the activated foil is expressed in terms of the excitation cross section and irradiation fluxes for the gamma-rays and neutrons as

$$Y_0 = \int N_{Foil} \sigma(E) \frac{d\phi(E)}{dE} dE \tag{5.2}$$

where $N_{Foil}$ is the number of nucleus in the target foil, $\sigma(E)$ and $\phi(E)$ are cross section and flux with energy E, respectively.

Two kind of foils, Au and Ni with natural enrichment, were used for our activation analysis, where Au foil was used for the measurement of gamma ray flux with the $^{197}$Au($\gamma$,n)$^{196}$Au reaction and Ni foil for the measurement of neutron flux by with the $^{58}$Ni(n,p)$^{58}$Co reaction. The foils employed had a shape of disc with a diameter of 10 mm and their weights were 70 and 460 mg (measured by an electronic balance with a precision of 0.1%) for Au and Ni, respectively.

The $^{197}$Au($\gamma$,n)$^{196}$Au cross section is referred from ref.[60]. For the $^{58}$Ni(n,p)$^{58}$Co cross section, the tabulated values of the cross section data JENDL-3.2 were used[62]. These cross sections are summarized in Fig. 5.20 and Fig. 5.21. Note that the cross sections in Fig. 5.20 include not only the $^{197}$Au($\gamma$,n)$^{196}$Au, but also the $^{197}$Au($\gamma$,np)$^{196}$Au reaction, where the latter reaction contributes to the evaluation of the gamma-ray flux.

In our work, we did not measure the energy spectra of gamma-rays produced by the electron beam incident on the Ta target. Instead, we obtained them by the calculation based on the Monte Carlo simulation as discussed in Sec. 5.3.2.

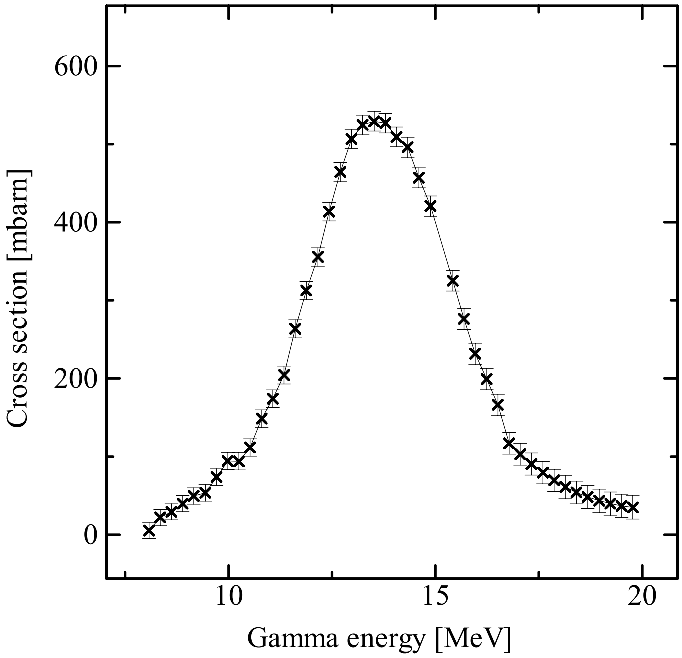

Fig. 5.20: The total Cross section for $^{197}$Au(g, n)+ $^{197}$Au(g, np) reactions[60].

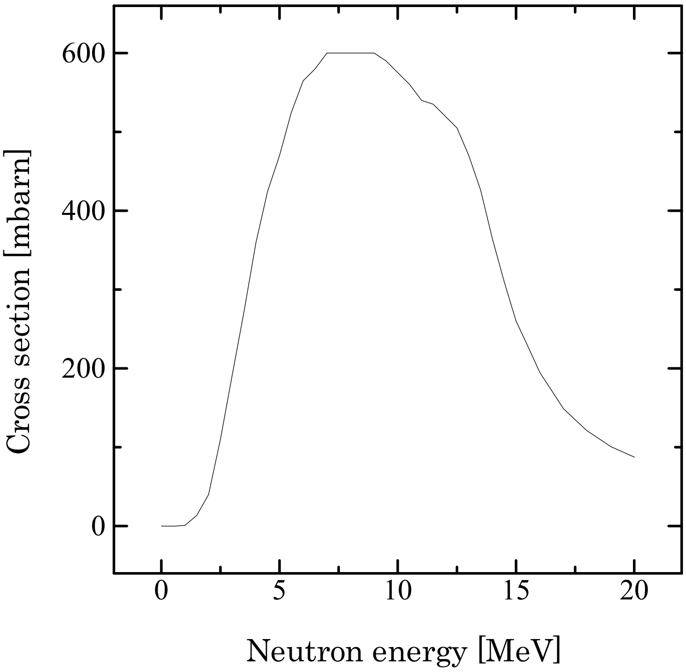

Fig. 5.21: Total Cross section for $^{58}$Ni(n,p)$^{58}$Co reaction[62].

The gamma-ray measurement for the irradiated foils were done by the Ge detector at the Hotlab. of KURRI as described in Sec. 5.1.6. The decay schemes for nuclei, $^{196}$Au and $^{58}$Co, are shown in Fig. 5.22 and Fig. 5.23. The 335.7 and 810.8

keV gamma-rays, which are generated after the strongest β decay branch, were used to obtain yield of $^{196}$Au and $^{58}$Co, respectively. The gamma-ray intensity following the β decay can be written in terms of the half life of β decay and braching ratio as

$$\frac{dI}{dt} = \varepsilon(E_\gamma) R_{Branch} Y(t) \frac{\ln(2)}{\tau_{1/2}} \tag{5.3}$$

where ε(E$_\gamma$) is an efficiency of the Ge detector for a gamma-ray with an energy E$_\gamma$, $\tau_{1/2}$ is a half life of the active product, and R$_{\text{Branch}}$ is a mean number of the gamma-ray production per one decay. Since Y(t) is a number of active product at the time, t measured from irradiation time, it is given in terms of the yield at irradiation, Y$_0$ as,

$$Y(t) = Y_0 \left(\frac{1}{2}\right)^{t/\tau_{1/2}} \tag{5.4}$$

From eq. (5.4) we can determine Y$_0$. This Y0 is put in eq. (5.2) and finally one can deduce the irradiation flux. The further analysis is discussed in Sec. 5.3.2.

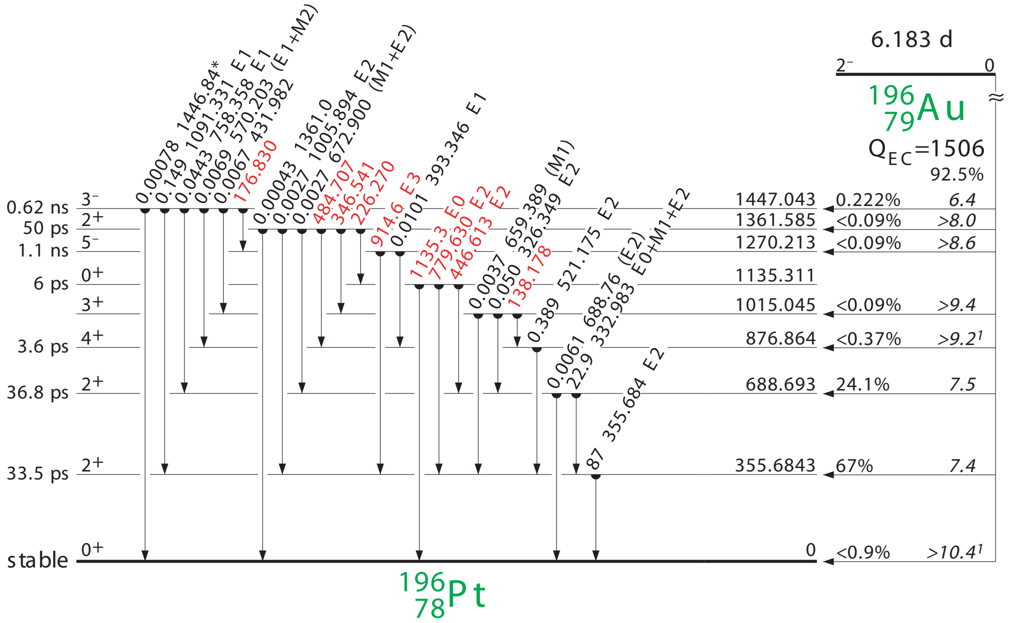

Fig. 5.22: Decay scheme drawing of $^{196}$Au[54].

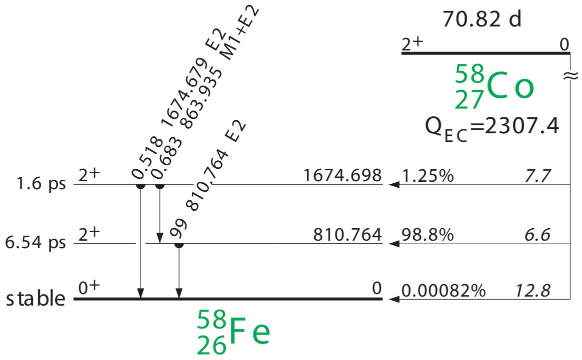

Fig. 5.23: Decay scheme drawing of $^{58}$Co[54].

The irradiation of foils were done in the beginning of the run A, B, and D as summarized in Table 5.4. The foils were located at positions as indicated in Fig. 5.24. They were irradiated for 30~60 minutes. Since the beam profile was not significantly changed run by run, the fluxes deduced represent approximately the irradiation fluxed during the measurement of ortho/para conversion. Profiles of the employed foils are listed in Table 5.5.

| Run Number (Foils) | Au foil | Ni foil |
|---|---|---|
| Beginning of run A | B and C | B and C |
| Beginning of run B | A, B and C | A, and B |
| Beginning of run D | B, D, and E | A |

Table 5.5: Profiles of foil irradiations for activation analysis.

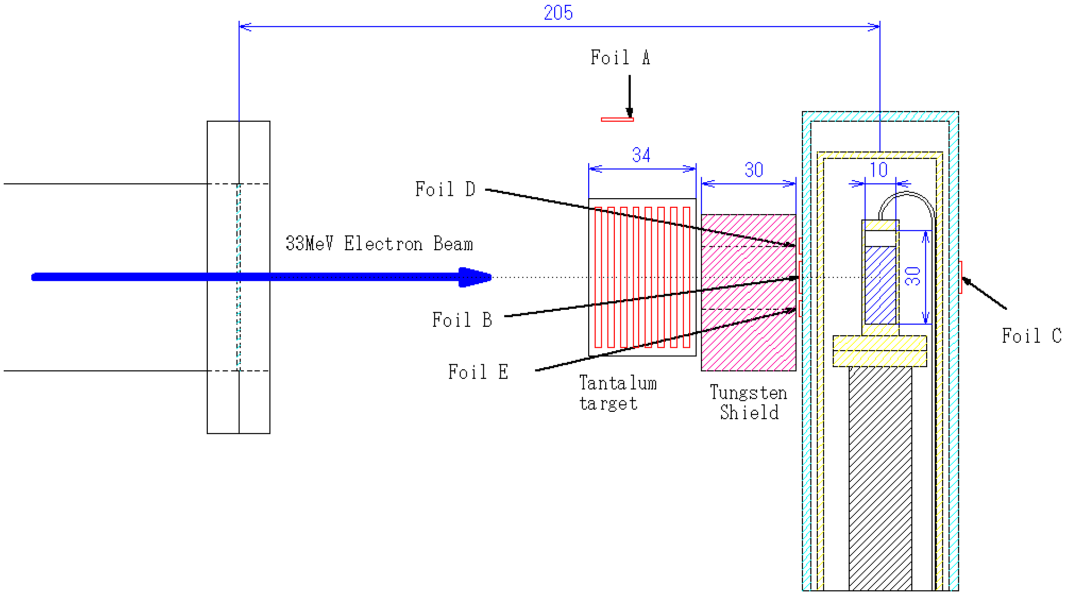

Fig. 5.24: Locations of foils used for the foil activation analysis.

The gamma-ray measurement on Au foils were done within 2 days after irradiation. The measurement time was 1000 sec in live time. In case of $^{58}$Co, because its half life is relatively long and the decay rate of gamma-rays is small, the measurement was done 10 days after irradiation, thus reducing the background caused by the fast decay components. The measurement time, in this case, was 20000 sec. The further detail of experimental results will be described in Sec. 5.3.

### 5.2.4 Measurement of ortho fraction by Raman spectroscopy

Procedures of measurement of the Raman spectroscopy at the Dept. of Physics, Kobe University is follows; the sample gas carried from KURRI by 50 cm$^3$ stainless bottle (transfer bottle) was transferred to the Raman cell evacuated up to $10^{-2}$ Pa before using as shown in Fig. 5.14.

The gas pressure of the Raman cell became about 2/3 of the initial pressure of the transfer bottle. The monochrometer scanned in a region from 20 cm$^{-1}$ to 750

$cm^{-1}$ with a scanning time of 1000 sec. The measurement was repeated 2 or 3 times in order to reduce the systematic errors. The constancy of laser intensity was checked by a power meter by in the beginning and at the end of the Raman measurement. It was found that laser intensity was stable better than 0.2% instability, which was enough for the present purpose. In the beginning and at the end of the Raman measurement, a normal $D_2$ gas sample at room temperature whose ortho/para fractions are known was used for checking the monochrometer efficiency.

The procedure to obtain ortho fraction from the Raman spectra were almost same as that performed at PSI. Therefore, visit Chapter 4, in particular Sec. 4.1.5.1 and 4.1.5.3 for the detail of the Raman spectroscopy. The only difference between PSI and KURRI, though it is minor, is concerned with the data analysis, i.e., S(J) was determined, in the former case, assuming the Gaussian peaks for each line, while, it was determined, in the present case, by summing up the peak area because the peak shape deviated from the Gaussian shape.

## 5.3 Experimental results

In this section, the experimental results of the measurements on the ortho fraction and irradiated doses for liquid $D_2$ are discussed.

### 5.3.1 Ortho fraction by irradiation

As described in the experimental procedure in Sec. 5.2.2 and 5.2.4, the determination of ortho fraction for irradiated liquid $D_2$ was done by analyzing the Raman spectra. A typical Raman spectrum in the region of pure rotational bands for irradiated $D_2$ is shown in Fig. 5.25. Comparing to the spectrum before irradiation (see Fig. 5.19), the ortho fraction obviously decreased. The statistical errors of our Raman spectroscopy were less than 0.2% for all of runs. On the other hand, the systematic errors mainly decided by fluctuation of the normal $D_2$ gas reference, were 0.2%. In Fig. 5.27, Fig. 5.28, Fig. 5.29, and Fig. 5.30, the ortho fractions measured by the Raman spectroscopy for the run A, B, C, and D are described together with the beam current against the irradiation time. The ortho fractions seem to decrease in proportion to the elapsed time as a general trend. In run A and D, few samples are taken after the end of irradiation experiment. These samples indicated no difference with the last irradiated sample. This means the conversion effect was caused by only the irradiation.

However, in case of the run C, the 2nd sample showed strange behavior; it showed a minimum ortho fraction in the series of samples. This might be due to decrease of the ortho fraction by air leakage which was caused by mis-handling during the sampling.

Consequently, we discarded this data from the analysis below. In Fig. 5.31, the ortho fractions are summarized as a function of the accumulated beam charge. The run B and D seem to decrease linearly approximately with the same gradient. The difference of behavior between the above two cases (B,D) and A may be caused by the fact that the Ta target used for the run B and D was different from that used for the run A.

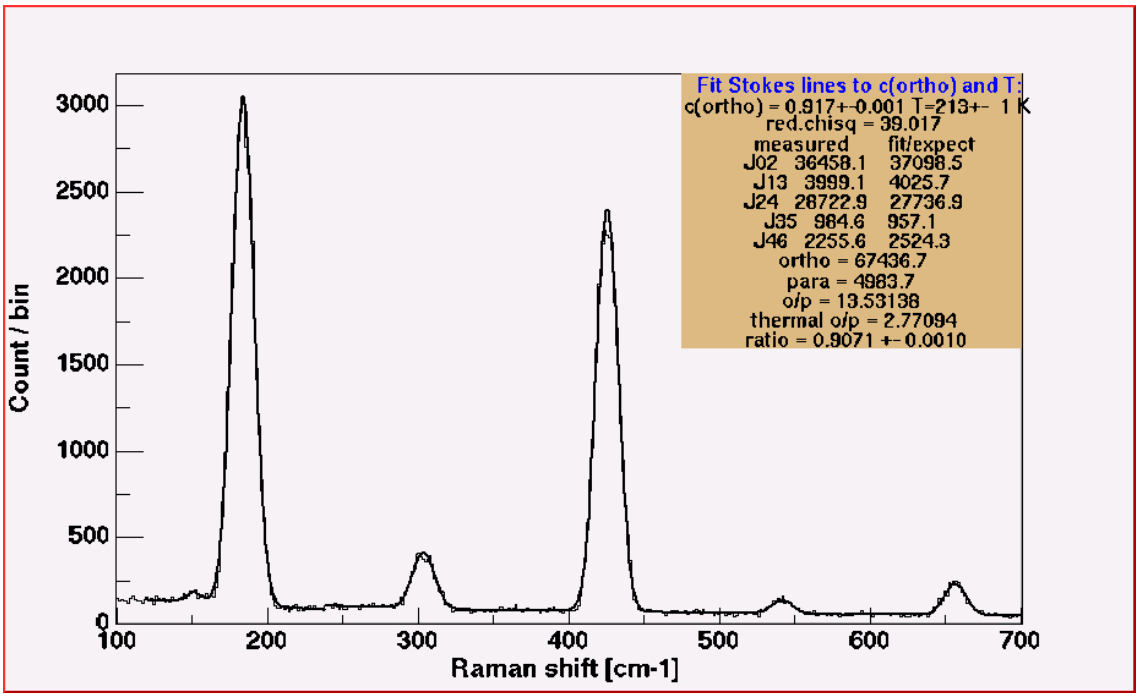

```
c(ortho) = 0.917+-0.001 T=213+-  1 K
red.chisq = 39.017
measured      fit/expect
J02   36458.1    37098.5
J13   3999.1     4025.7
J24   28722.9    27736.9
J35   984.6      957.1
J46   2255.6     2524.3
ortho = 67436.7
para = 4983.7
o/p = 13.53138
thermal o/p = 2.77094
ratio = 0.9071 +- 0.0010
```

Fig. 5.25: Raman spectrum of irradiated $D_2$ (5th sample of the run B). The ortho fraction decreases comparing to the case before irradiation.

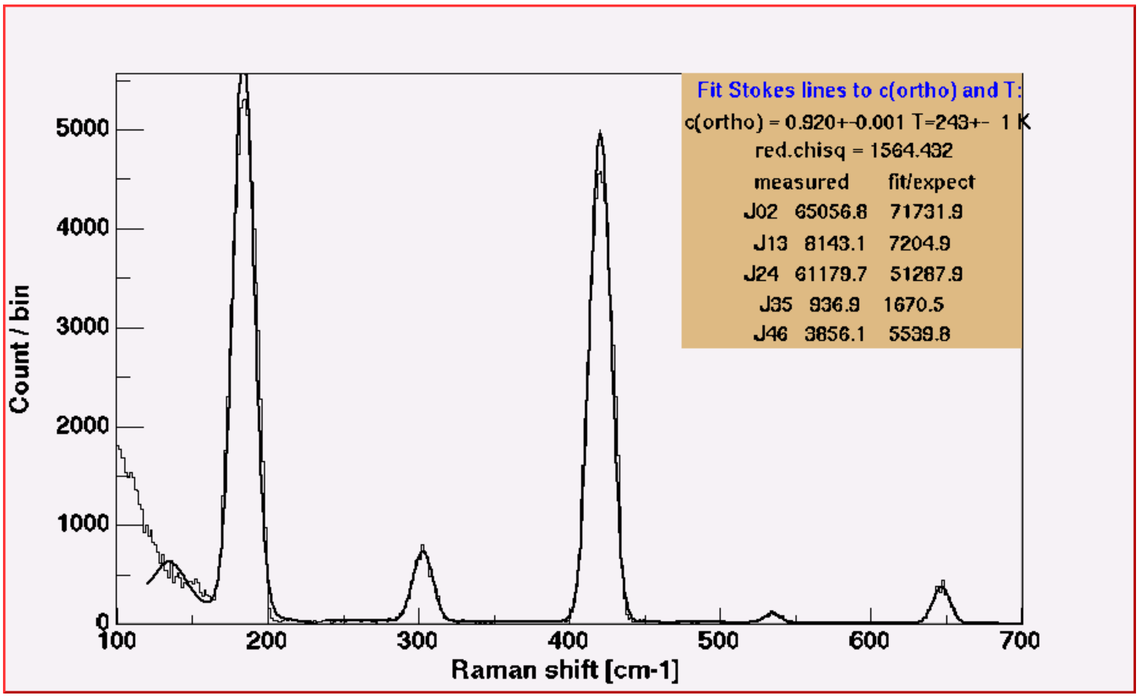

Fig. 5.26: Raman spectrum of irradiated $D_2$ (2nd sample of run C). The peak in 100 $cm^{-1}$ was caused by $N_2$ and $O_2$ contamination.

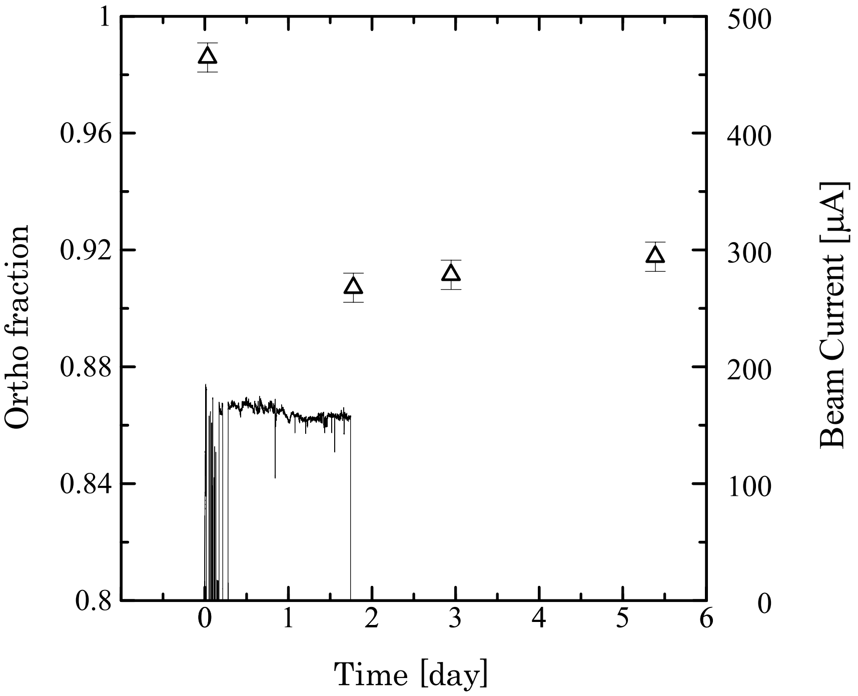

Fig. 5.27: Ortho fraction plotted as a function of irradiation time for the Run A.

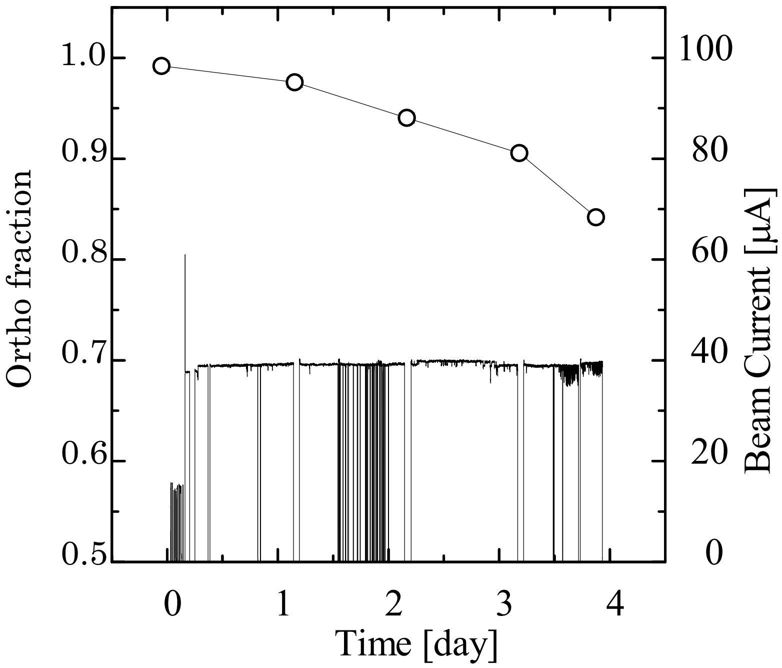

Fig. 5.28: Ortho fraction plotted as a function of irradiation time for the Run B.

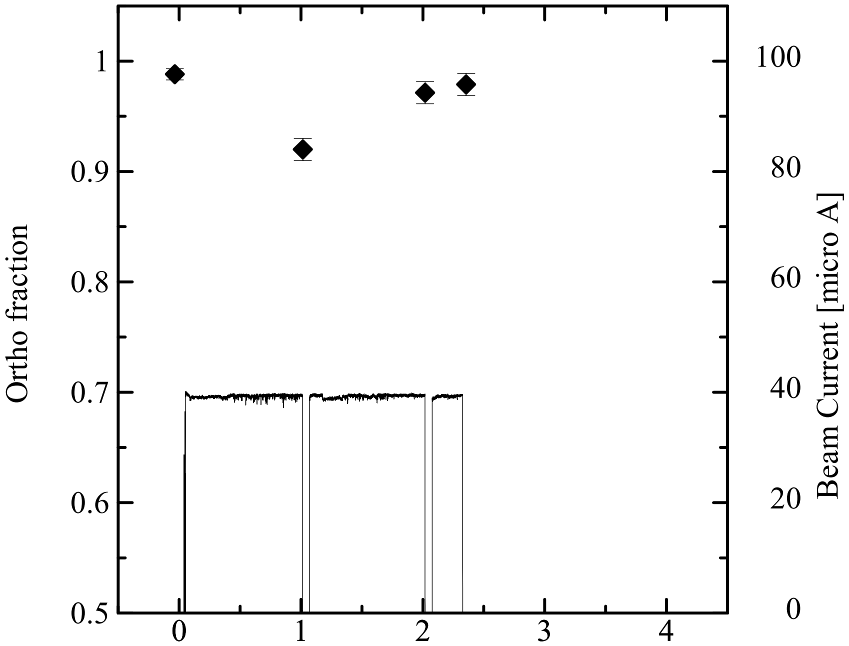

Fig. 5.29: Ortho fraction plotted as a function of irradiation time for the Run C.

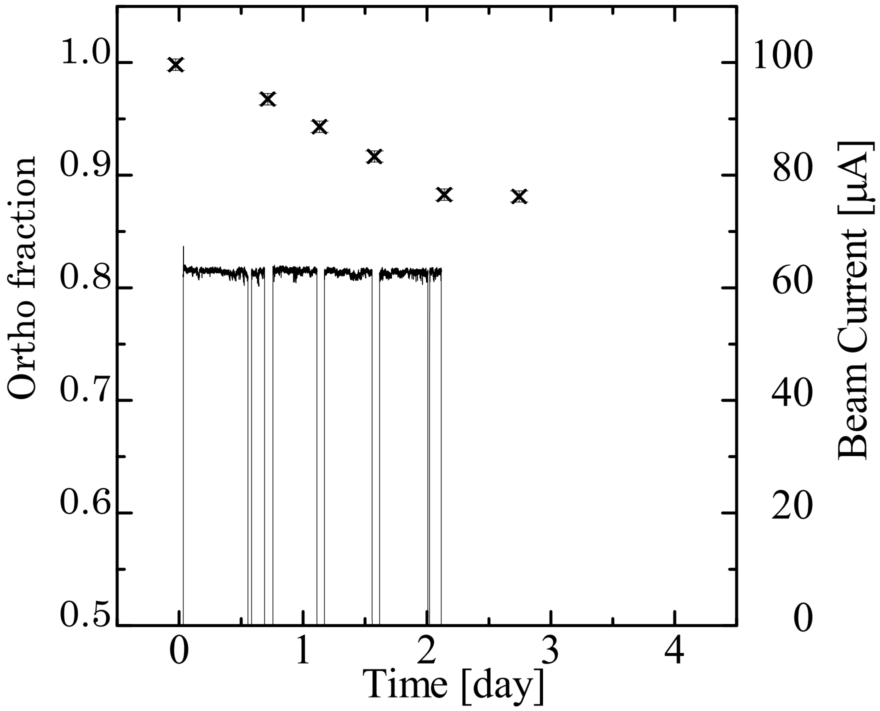

Fig. 5.30: Ortho fraction plotted as a function of irradiation time for the run D.

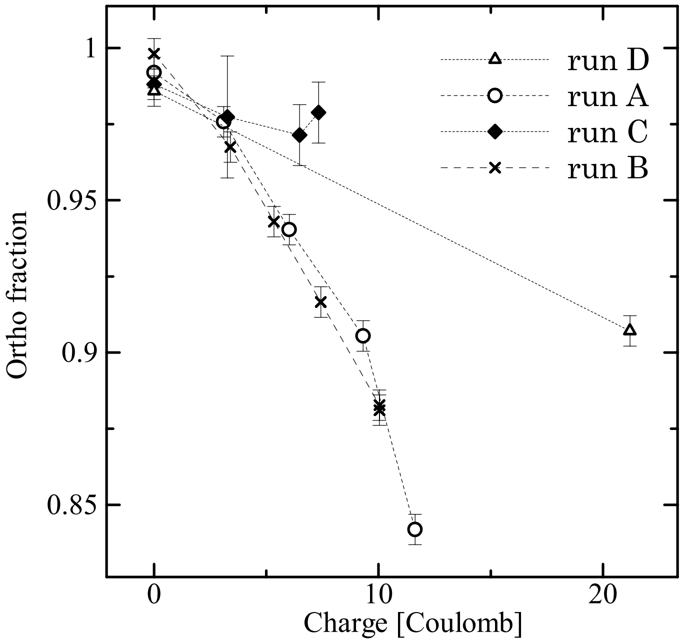

Fig. 5.31: Summary of the data on the ortho fractions measured by Raman spectroscopy (raw data) plotted as a function of integrated beam currents. The markers, triangle, circle, diamond, and cross correspond to the run A, B, C, and D, respectively.

#### 5.3.1.1 Correction of instrumental errors caused by universal counter

In the course of the irradiation experiment of the run B, C, and D we met a rather serious problem that there was nonlinearity between the laser intensity and counting rate. It was found that this nonlinearity was due to miss-operation of the universal counter (see Fig. 5.12) in particular when the counting rate was small. Though all data on the Raman spectra were taken with this miss-operating universal counter, such nonlinearity was successfully corrected by using the counting rates of the Raman spectra taken for the normal $D_2$ reference. In this subsection, we describe outline of the method to correct the nonlinearity.

The nonlinearity is clearly seen in the change of Raman spectra for the normal $D_2$ reference taken by changing the laser power as shown in Fig. 5.32. If the counting system works correctly, each peak height must be proportional to the laser power, in other words, the Raman peaks divided by the laser power must be constant. However, as shown in Fig. 5.32, the low counting peaks are much suppressed compared with the high counting peaks with respect to the change of laser power. Such nonlinearity was found to be caused by a channel defect of the universal counter.

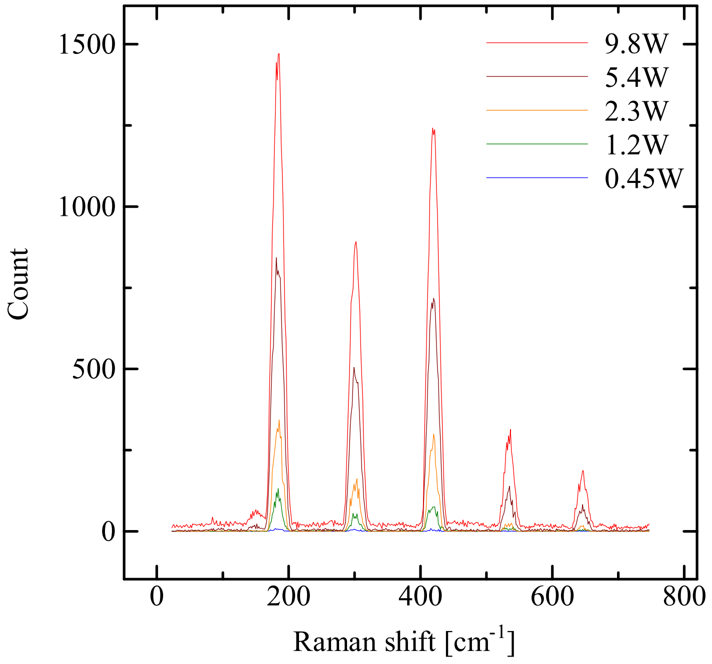

Fig. 5.32: The Raman spectra of the normal $D_2$ reference with varying the laser power. It is seen that the counts for small peaks were less than expected.

To see the nonlinearity effect more quantitatively, the Raman spectra for the reference sample (normal-$D_2$) was measured with the laser power of 9.8, 5.4, 2.3, 1.2, and 0.45 W. The peak counts for the 5 sample peaks in the Raman spectra are compared with those for the same sample peaks measured by a correct channel of the universal counter. A series of measurements were done twice, i.e., on 30th May 2003 and on 20th June 2003. The results are plotted in Fig. 5.33 and Fig. 5.34, respectively. The statistical errors of the measurement were small enough to influence the discussion below.

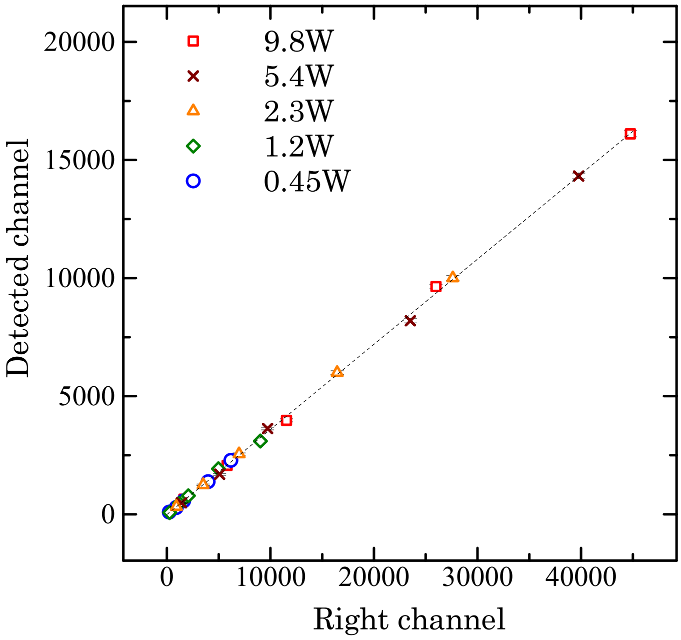

Fig. 5.33: The peak counts measured by right channel (x-axis) and defected channel (y-axis). This measurement was done on 30th May 2003. The dashed line is a fitting curve assuming eq.(5.5)

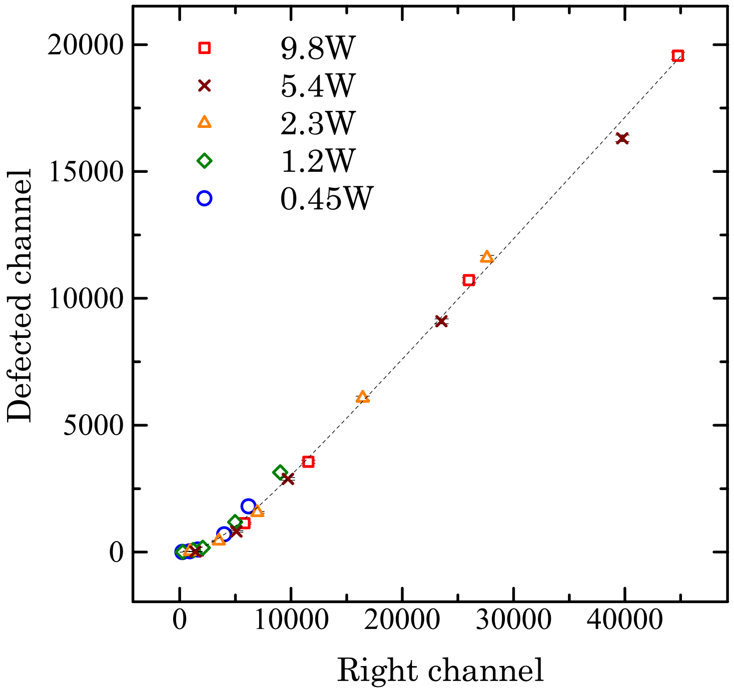

Fig. 5.34: The peak counts measured by right channel (x-axis) and defected channel (y-axis). This measurement was done on 20th June 2003. The dashed line is a fitting curve assuming eq. (5.5)

The results in the former day and those in the latter day are not same each other. only the data on 20th Jun 2003 shows the nonlinear behavior. The results on 20th Jun 2003 has characteristics that the function approximately follows a parabolic function in a low counting region, and asymptotically becomes a linear function at a high count region. Therefore, a hyperbola function expressed by

$$f(x) = \left( \frac{-1+\sqrt{1+a^2x^2}}{a} \right) b \tag{5.5}$$

can be a good fitting fitting function as the response function because f(x) forms $f(x) \cong \frac{b}{2}(ax)^2$ for $x << a$, and $f(x) \cong bx$ for $x >> a$. The dashed lines in Fig. 5.33 and Fig. 5.34 are the results of the $\chi^2$ fitting by using the response function of eq. (5.5). The deduced numerical values are tabulated in Table 5.6.

| Measured date | a | b | Reduced $\chi^2$ |
|---|---|---|---|
| 30th May 2003 | $3.97\times10^{-2}$ | 0.361 | 0.96 |
| 20th Jun 2003 | $2.06\times10^{-4}$ | 0.484 | 3.96 |

Table 5.6: The results of fitting for Fig. 5.33 and Fig. 5.34.

In eq. (5.5), the parameter "b" is just a normalization parameter, and parameter "a" gives more characteristic behavior of the response function; if "a" is increased, a region of curved area shrinks and the response function is expressed by a linear function.

Then, the experimental data taken for the irradiated $D_2$ samples are corrected by using the above response functions. Since the nonlinearity effects change somehow depending on the measurement time as shown in Table 5.6, all the experimental data should be corrected by their own response function. In our measurement it is known that the ortho fractions may vary from 0.67 to 1.0. Taking this point into account, we introduced the ortho fraction, $c_o$ as an additional free parameter in eq. (5.5) to be determined by the $\chi^2$ fitting method. Firstly, the $i^{th}$ peak counts of the experimental data (ortho fraction=$c_o$) and the reference data (ortho fraction=0.667) are defined as y[i] and x[i], respectively. y[i] and normalized x[i] are compared in a similar way to deduce Fig. 5.33 or Fig. 5.34. In this case, $\chi^2$ is given by

$$\chi^2 = \sum_{ortho}\left(\frac{y[i] - f\left(\frac{c_o}{0.667}x[i]\right)}{\sigma_i}\right)^2 + \sum_{para}\left(\frac{y[i] - f\left(\frac{(1-c_o)}{0.333}x[i]\right)}{\sigma_i}\right)^2 \tag{5.6}$$

By searching for the $\chi^2$ minimum, the most probable values of the parameters, a, b, and $c_o$ were deduced. Here, $\sigma_i$ is a statistical error of y[i] defined by

$$\sigma_i = \sqrt{y[i]} \tag{5.7}$$

For example, correction of the 4th sample of the run B is shown in Fig. 5.35. The raw peak counts (open circles) are corrected and consequently shift to the normalized points (cross points) by the above procedure. Then, the parameters, a, b, and $c_o$ were determined from the $\chi^2$ minimum. The errors of about 0.5% were mostly determined by the fitting procedure. The deduced small value for “a” is associated with the large distortion of the response function, and consequently gives a larger error for a high ortho fraction. Especially, the 1st sample of the run D gave error more than 2%.

The corrected ortho fractions, thus obtained are summarized in Fig. 5.36. The 2nd sample of the run B (air contaminated sample) is discarded from the plot. It is found that the corrections work to make the ortho fractions about 2% reduced, while the gradient of $c_0$ against the beam charge doesn't change.

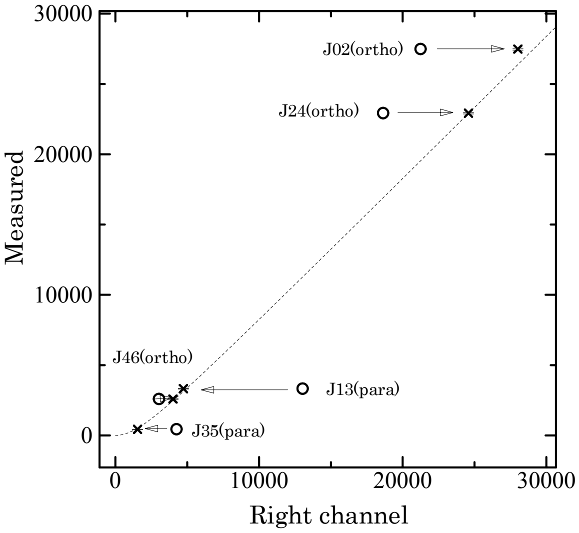

Fig. 5.35: The measured peak counts vs reference peak counts. The raw peak counts (open circles) move to the normalized points (cross points). The dashed line is a fitting function.

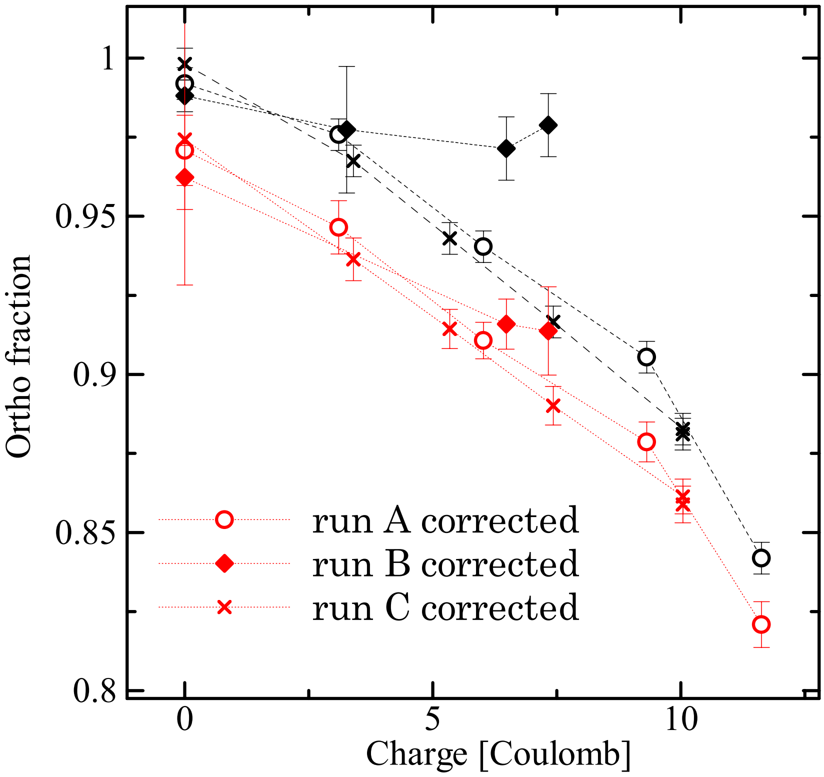

Fig. 5.36: Ortho fractions corrected from Fig. 5.31. Black markers are the raw data and red markers are the corrected data. See the text for further detail.

#### 5.3.1.2 Corrections of ortho fraction due to relaxation time

The sample gas filled in a 50 cm$^3$ SUS304L bottle was transported from KURRI to Kobe University for the Raman spectroscopy. The maximum storage time of the gas in the bottle is 3.6 days. The gas was, then, transferred to a Raman cell made of aluminum which was used for taking Raman spectra as described in Fig. 5.14. The time needed to measure the Raman spectrum was equal to or less than 3000 sec. In the course of the above procedures after sampling irradiated liquid $D_2$, the ortho state of sample $D_2$ gas is relaxing to the para state and the ortho fraction is going toward the thermal equilibrium value, 0.667. Therefore, this relaxation effect must be considered for correctly evaluating the time dependence of the ortho fraction due to irradiation. The relaxation times of the ortho state in the Raman cell and the SUS bottle were measured before and after the Raman measurement.

The relaxation time of the Raman cell was 23±0.5 days. As described in Sec. 4.2.2, the ortho fraction obeys exponential function;

$$c_o = p_1 \exp(-p_2 t) + \frac{2}{3} \tag{5.8}$$

Since in case of the Raman cell, less than $10^{-4}$ of the ortho fraction has changed during the Raman measurement, the relaxation effect in the Raman cell is negligible small. On the other hand, in case of the SUS bottle, the relaxation time was varied from 177 to 4400 days depending on the run number. In the present experiment, 5 SUS bottles were used for the transportation. Because the same bottle gave the different relaxation time, the relaxation in the SUS bottle might be caused not by the wall effect, but by the gas contamination. To obtain a reliable value of relaxation time we averaged the relaxation time extracted from the 6 measurements. As result, the $p_2$ in eq. (5.3) was given as $2.4 \pm 2.2 \times 10^{-3}$ $s^{-1}$, which corresponded to the relaxation time of 409 days. This value was used to the correction of our present measurement. The largest correction of the effect was 0.2%.

#### 5.3.1.3 Correction of ortho fraction due to vapor pressure difference between ortho and para $D_2$

It is known that the vapor pressure of liquid $D_2$ is different each other in the ortho and para state. This needs a further correction of the ortho fraction because the vapor pressure difference may cause the change of the ortho fraction in the gas extraction process. The vapor pressures of liquid $D_2$ at 23.57 K with the ortho fraction of 97.8% and 66.67% are, respectively, 101.3 kPa and 102.7 kPa[55]. According to the Raoult's law, the vapor pressure, P, of mixed liquid, A and B, can be written as.

$$\begin{aligned} \mathrm{P_A} &= X_A P_{A0} \\ P_B &= X_B P_{B0} \end{aligned} \tag{5.9}$$

where $X_A$ and $X_B$ are the molar fraction of A and B in liquid. $P_{A0}$ and $P_{B0}$ are the vapor pressure in a pure liquid, and $P_A$ and $P_B$ are the partial vapor pressures of A and B. Thus, molar fraction in liquid $X_A$ can be written as

$$\mathrm{X_A} = \frac{1}{\frac{P_{A0}}{P_{B0}}\frac{(1-C_A)}{C_A}+1} \tag{5.10}$$

where

$$\mathrm{C_A} = \frac{P_A}{P_A + P_B} \tag{5.11}$$

The ref.[22] enables an extrapolation of the vapor pressure data at 23.5 K to that at 25 K and the calculated results are 147.6 kPa and146.3 kPa for 97.8 % and 66.7 % of the ortho fraction, respectively. From the discussion of the preceding paragraph, the vapor pressures of the pure ortho and para-$D_2$ are given as 147.7 and 143.5 kPa at 25 K.

Here, the measured ortho fraction of gas sample, $c_o$, gives us the information of

$$\mathrm{c_o} = \frac{P_o}{P_o + P_p} \tag{5.12}$$

where $P_o$ and $P_p$ are the partial vapor pressure of the ortho and para-$D_2$. By using eq.(5.10), the ortho fraction in liquid, $X_o$, can be written as

$$\mathrm{X_o} = \frac{1}{\frac{P_{o0}}{P_{p0}}\frac{(1-c_o)}{c_o}+1} \tag{5.13}$$

where

$$\frac{P_{o0}}{P_{p0}} = 1.046 \tag{5.14}$$

This must be applied for correction of the ortho fraction of the gas sample. In other word, the measured ortho fraction for the sampled gas is always higher than that in the liquid phase. For example, if we measured 70.0% of ortho fraction for the sample gas, the true ortho fraction in the liquid phase is 69.0%.

#### 5.3.1.4 Natural relaxation of ortho $D_2$ in irradiation cell

As described already, the irradiation cell is made of copper. Natural conversion of liquid $D_2$ due to the copper surface must be corrected for the measured irradiation effect. Therefore, the relaxation time was measured. The experiment on the natural conversion has been done after irradiation experiment at KURRI, keeping liquid $D_2$ temperature at 25 K (thermal equilibrium ortho fraction is 95.2%). In this case, we chose two conditions for the ortho fraction as a starting condition; either a high ortho fraction, 98.5%, or a low ortho fraction, 83%. The measurement was done with a period of a week. Sample gases were extracted every 2~3 days, where the extraction processes were same as those employed in the irradiation experiment. The natural conversion time was about 20 days for both cases of the starting conditions, whose results are shown in Fig. 5.37. It is noted that this value was 6 times short as expected value, 129 days, from the discussion in Sec 3.3.1.

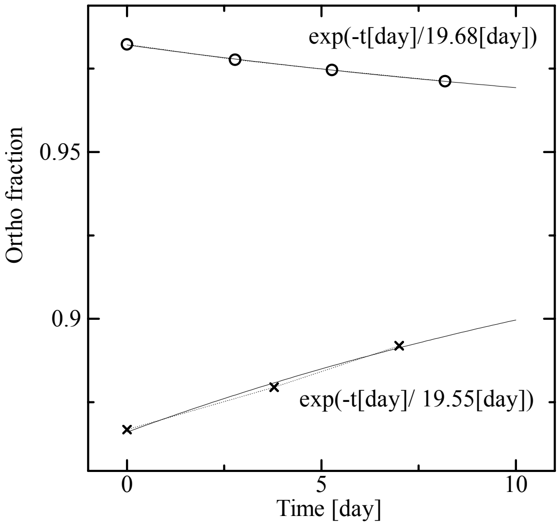

Fig. 5.37: Ortho fraction plotted as a function of time (day). These data have been measured after irradiation experiment.

A catalyzing effect of the copper surface of the irradiation cell is expected to be $6\times10^{-8}$ mol/m$^2$/s[22]. Because the catalyzing effect of the surface is calculated to be order of $10^{11}$ sec, this effect is negligibly small compared to the natural conversion. On the other hand, there is a possibility that the natural conversion can be enhanced by the $O_2$ contamination. As described in Sec 3.3.2, $O_2$ works as a catalyst, e.g., 1ppm contamination makes catalyzing conversion time of 13 days. Since our device allows mixture of about 0.8 ppm $O_2$ contamination, the observed relaxation time, 20 days are reasonably reproduced by the $O_2$ contamination. The relaxation time, 20 days are enough long compared with the irradiation time, 4 at most 4 days. In conclusion, we use this value in the discussion given in Sec5.4.

### 5.3.1.5 Contamination in deuterium

The purity of deuterium was experimentally examined by means of the gas chromatography. The gas chromatography allows the measurement of oxygen and nitrogen. 1-liter deuterium at 1 atm whose ortho fraction was concentrated by the catalyst was mixed with a helium gas four times larger volume than the deuterium gas to increase the pressure up to the value valid for the gas chromatography. Thus, the mixed sample with pressure 500 kPa was devoted to the gas chromatography. The contamination levels for $O_2$ and $N_2$ were determined in comparison with a standard sample. The contamination levels for $O_2$ and $N_2$ in the deuterium sample were unexpectedly high, i.e., 11.7 and 36.3 ppm respectively. However, these high contamination levels might be air due to mistreating the gas chromatography, e.g., air leak of the connector between the reservoir and apparatus of the gas chromatography.

## 5.3.2 Radiation dose in $D_2$ observed by means of the foil activation analysis

One of the important subjects in our work is to determine the radiation dose given to the liquid $D_2$. For this purpose, the radiation flux measurement is of primary importance. This was done by the foil activation method in combination with gamma-ray energy spectra calculated by means of the Monte Carlo simulation code, Geant4. The flux thus obtained was compared with the results of Geant4 again to check the overall consistency. Using the radiation fluxes established by the above procedure, the radiation dose was evaluated and compared with the experimental data on the heat deposit.

### 5.3.2.1 Foil activation analysis

From the results of the gamma-ray measurement for irradiated foils as shown in Table 5.5, the number of activated nuclei per unit beam charge can be evaluated. One of the energy spectra for the β delayed gamma-rays from $^{196}$Au measured by the apparatus described in Sec.5.1.6 is shown in Fig. 5.38. Similarly to the procedure of Sec.5.1.6, the peak counts for 355.7 keV gamma-rays was obtained assuming that the peak follows the Gaussian shape.

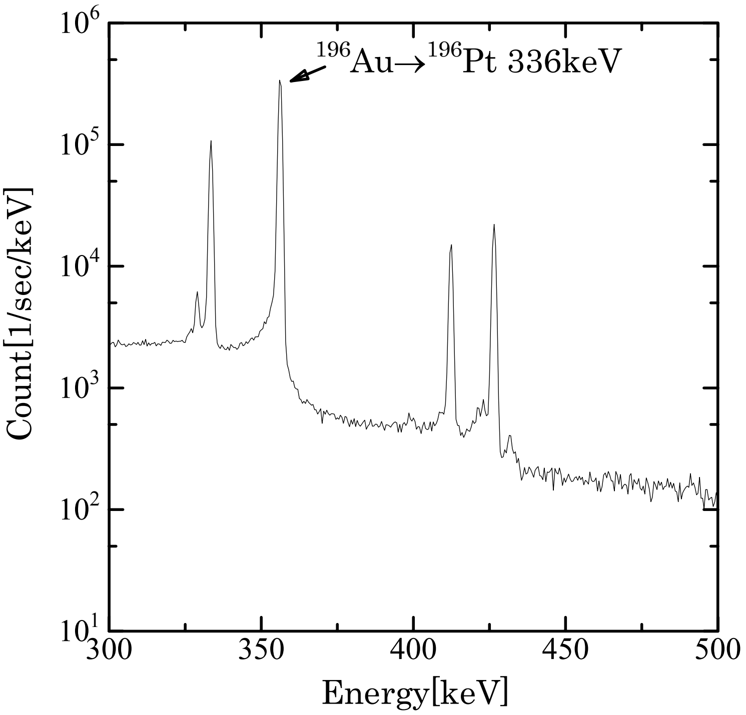

Fig. 5.38: Energy spectrum of β delayed gamma-ray of $^{196}$Au.

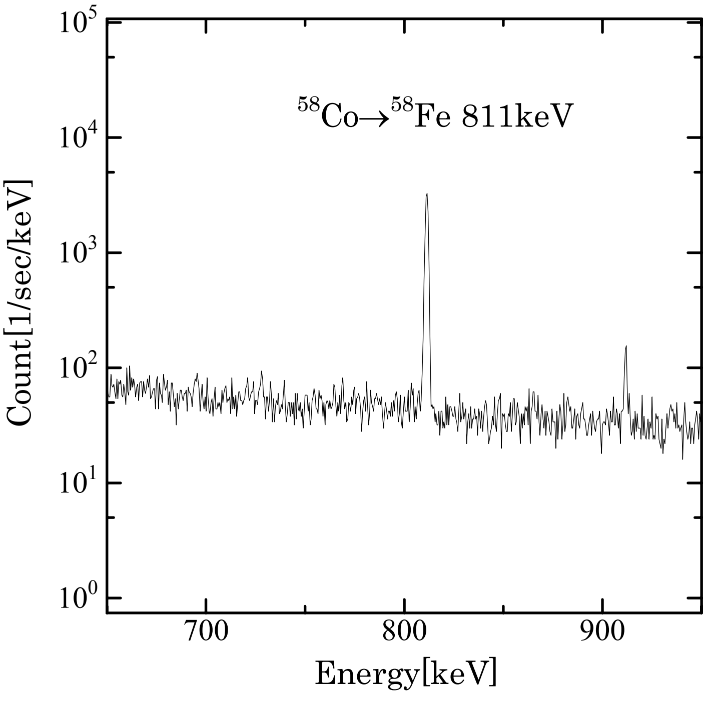

Fig. 5.39: Energy spectrum of β delayed gamma-ray of $^{58}$Co.

According to eq.(5.3) and eq.(5.4), the irradiation induced yield, $Y_0$, can be deduced from the count rate of the Ge detector by using the known decay times and branching ratios in ref. [54] (see Fig. 5.22 and Fig. 5.23). Here, we can estimate that the radiation flux is proportional to the beam current, thus, the produced activation per unit beam charge give us the information of the radiation flux. In order to deduce the radiation fluxes from eq.(5.2), we need the ratio of number of produced activity, Y, and the number of irradiated atoms. The ratios for each foil in Table 5.5 are shown in Table 5.7 for Au and Table 5.8 for Ni. According to eq.(5.2),

$$\int \sigma(E) \frac{d\Phi(E)}{dE} dE = \frac{Y_0}{N_{Foil}} \tag{5.15}$$

can be deduced. The cross sections, σ(E), are known as Fig. 5.20 and Fig. 5.21. Then the energy spectrum of the radiation flux induces the total intensity of radiation. The errors are statistically less than 1%, and systematically 3%, which was caused error of detector efficiency.

| Run Number | Au foil position | Activation ratio per charge (1/Coulomb) |
|---|---|---|
| Run A | B | $1.52\times10^{-09}$ |
| | C | $7.14\times10^{-10}$ |
| Run B | A | $1.12\times10^{-10}$ |
| | B | $7.62\times10^{-09}$ |
| | C | $2.76\times10^{-09}$ |
| Run D | B | $6.61\times10^{-09}$ |
| | D | $5.79\times10^{-09}$ |
| | E | $2.14\times10^{-09}$ |

Table 5.7: The production ratio of activated nucleus ($^{196}$Au) per μC for of Au foils.

| Run Number | Ni foil position | Number of Active product (1/Coulomb) |
|---|---|---|
| Run A | B | $3.47\times10^{-12}$ |
|  | C | $1.21\times10^{-12}$ |
| Run B | A | $4.43\times10^{-12}$ |
|  | B | $2.69\times10^{-11}$ |
| Run D | A | $5.15\times10^{-12}$ |

Table 5.8: The number of activated product ($^{58}$Co) per μC for of Ni foils.

The energy spectrum of neutrons was measured for 29-mm thick Ta target[57] and shown in Fig. 5.40. The ref. [57] reported the angular distribution of the neutron flux was almost isotropic. In our work, this neutron energy spectrum was used.

Concerning the gamma-ray flux, the electron Bremsstrahlung has been well studied and the reliable calculation code was established. In our work, the gamma-ray energy spectra calculated by the Monte Carlo simulation code "Geant4.5" was used. The discussion on it will be done in the next section.

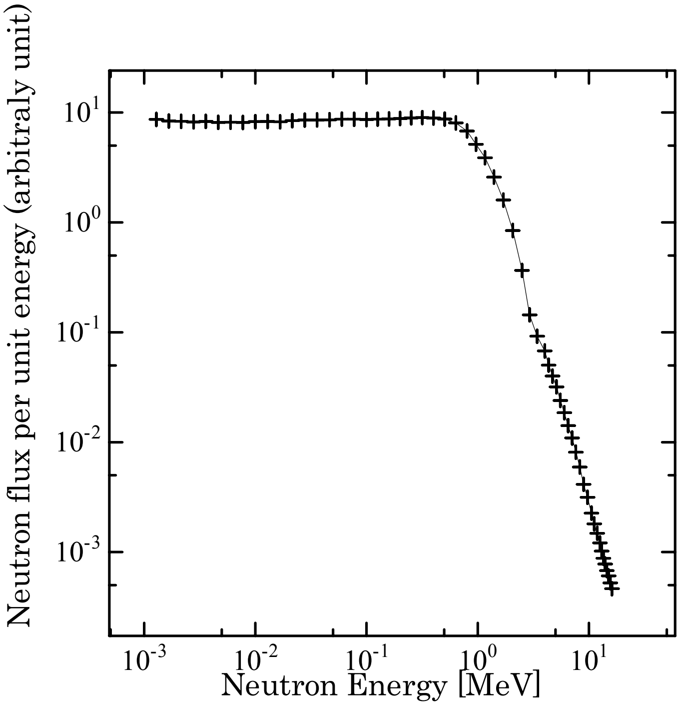

Fig. 5.40: The neutron energy spectrum for a 29 mm thick Ta target [57].

### 5.3.2.2 Monte Carlo Simulation with "Geant4.5"

The Monte Carlo simulation code, "Geant4.5" was used to obtain the radiation dose in this experiment. This simulation code was used for the following two purposes, the first purpose is to obtain the gamma-ray energy spectrum introduced in former section, and the second purpose is to determine the radiation dose using the deduced radiation fluxes.

Firstly, we discuss the calculation of the energy spectrum of the electron-induced gamma-ray. A schematic view of the experimental setup is shown in Fig. 5.40 and each dimension was taken as an input parameter of the computer code. Then, the calculation was executed for the $10^7$ electrons with the energy spectrum shown in Fig. 5.3. The gamma-ray fluxes incident on the foils for activation analysis are shown in Fig. 5.42. Four calculations have been done with a 15-mm thick Ta target: at the position B (red) and C (orange), and with a 29-mm thick Ta target: at the position B (green) and C (blue). The numerical values for summed gamma-ray are given in Table 5.9.

In these calculations, only the electromagnetic effect, especially photoelectric effect, Compton effect, and pair creation effect was calculated down to 1keV. The nuclear effect was ignored in this calculation.

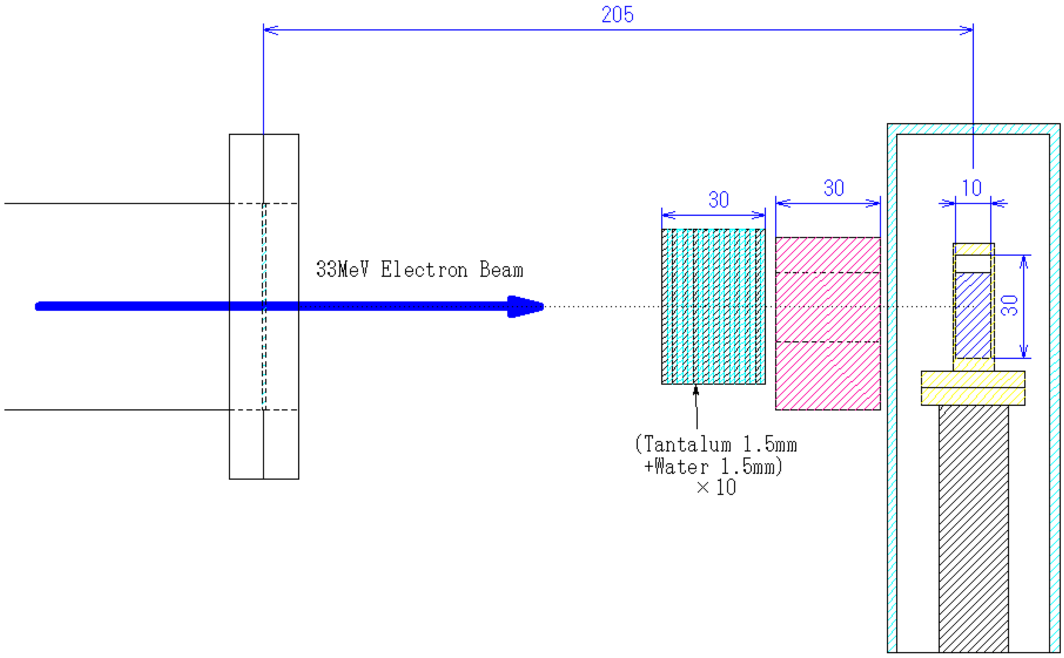

Fig. 5.41: Input geometry used for the input parameters of the Geant4.5 computer code. The Ta target, W shield, Al chamber, Cu irradiation cell, and $D_2$ are included in the geometry.

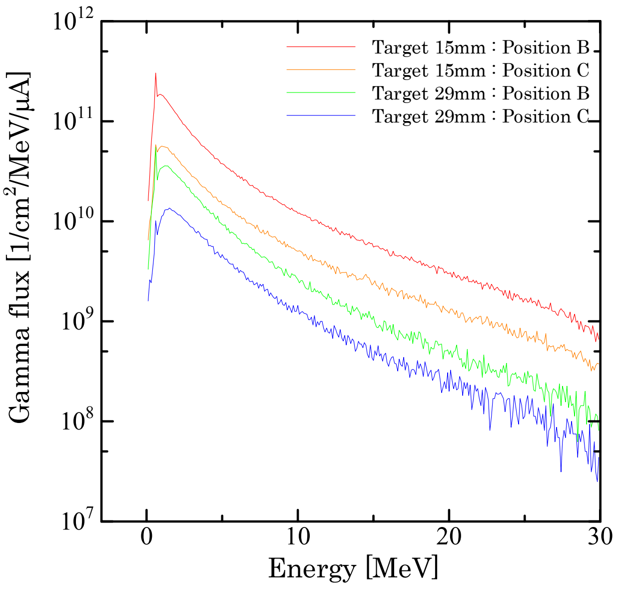

Fig. 5.42: Calculated energy spectra for the gamma fluxes per 1μA. Four fluxes, with a 15-mm and 29-mm thick Ta targets and the position of observation shown in Fig. 5.24 were taken into calculation. See the text for further detail.

| Target thickness | Detect (Foil) position | Gamma flux (/cm²/μA) |
|---|---|---|
| 15mm | B | $6.66\times10^{11}$ |
| 15mm | C | $2.38\times10^{11}$ |
| 29mm | B | $1.47\times10^{11}$ |
| 29mm | C | $6.06\times10^{10}$ |

Table 5.9: The calculated total fluxes per μA for the gamma-rays shown in Fig. 5.42

The calculated results of the heat load in $D_2$ are summarized in Table 5.10 and Table 5.11 for 29mm and 15mm Ta target, respectively. Statistical errors for figures indicated in this table are less than 1%. The heat load on the deuterium caused by the copper cell is evaluated in comparison with those calculated for the following two cases; one is the calculated result with the presence of copper cell, and the other one is the calculated result with the copper cell removed. It was found that one can conclude about 1/2 of the heat load on the deuterium is due to the copper cell. The total heat load on 2nd state of cryostat was also calculated and this value will be compared to the heat load in the experiment.

| Geometry | Total heat load (mW/μA) | Dose (W/g/μA) |
|---|---|---|
| Deuterium | 0.352 (0.220 from Cu cell) | 0.935 (0.548 from Cu cell) |
| Copper cell | 8.73 | 0.534 |
| Cryostat (total) | 25.5 | - |

Table 5.10: Heat loads caused electromagnetic effect calculated by the Monte Carlo simulation with the Geant4 for the 29-mm thick target.

| Geometry | Total heat load (mW/μA) | Dose (mW/g/μA) |
|---|---|---|
| Deuterium | 1.66 (1.00 from Cu cell) | 4.41 (2.67 from Cu cell) |
| Copper cell | 39.2 | 2.40 |

| | | |
|---|---|---|
| Cryostat (total) | 72.9 | - |

Table 5.11: Heat loads caused electromagnetic effect calculated by the Monte Carlo simulation with the Geant4 for the 15-mm thick Ta target.

This simulation code can also calculate the heat load by the neutrons. Producing neutron from center of the Ta target isotropically with the energy spectrum of Fig. 5.3, the heat load caused by the neutrons was calculated. The heat load in $D_2$ and in other parts are listed in Table 5.12. In this case, the component of the heat load in Copper cell is negligible small.

| Geometry | Total heat load (mW/$10^{16}$neutron) | Dose (mW/g/$10^{16}$ neutron) |
|---|---|---|
| Deuterium | 0.396 | 1.05 |
| Copper cell | 0.085 | 0.022 |
| Cryostat (total) | 0.679 | - |

Table 5.12: Heat loads caused neutron calculated by the Monte Carlo simulation with the Geant4 per $10^{16}$ neutron production.

### 5.3.2.3 Radiation flux

Using the calculated energy spectra of gamma-rays shown in Fig. 5.42, the total flux can be evaluated from eq.(5.15) and from Table 5.7. For example, the energy spectrum of yield for $^{196}$Au can be calculated by multiplying the gamma-ray energy spectrum calculated by the Monte Carlo simulation and the excitation function of the cross section for $^{197}$Au($\gamma$,n)$^{196}$Aul. This is shown by the black curve in Fig. 5.40. The integration of this curve over the gamma-ray energy gives the total yield for the $^{196}$Au production rate (measured by the foil activation analysis) per incidence of one gamma-ray. Consequently, one can determine the absolute value of the gamma-ray flux, where the relative spectrum is based on the calculation. In a similar way, the neutron flux per was also obtained. The deduced results are tabulated in Table 5.13 and Table 5.14.

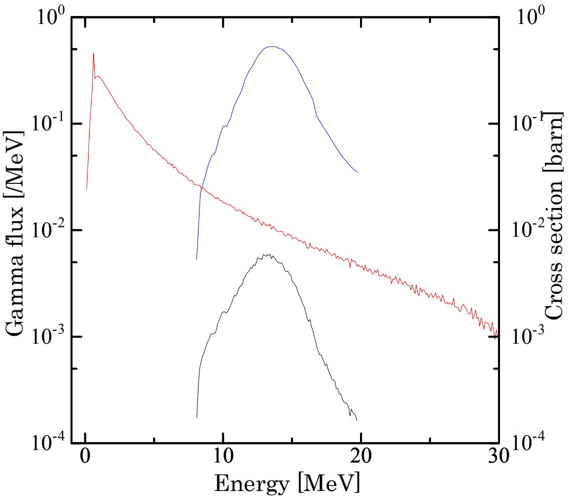

Fig. 5.43: The energy spectrum of yields for $^{196}$Au (black). Here, the red curve is the energy spectrum of gamma-ray flux Φ(E) calculated by the Monte Carlo simulation, and the blue curve is the excitation function of the cross section for $^{197}$Au(γ,n)$^{196}$Au. In evaluating the gamma-ray flux by the Monte Carlo simulation we assume that the Ta target thickness is 15 mm and the position of observation is the position B.

| Run Number | Au foil position | Gamma flux per current at foil position (1/cm$^2$/μA) |
|---|---|---|
| Run A | B | $6.52\times10^{10}$ |
|  | C | $2.61\times10^{10}$ |
| Run B | A | $4.15\times10^{9}$ |
|  | B | $2.82\times10^{11}$ |
|  | C | $8.81\times10^{10}$ |
| Run D | B | $2.45\times10^{11}$ |
|  | D | $2.14\times10^{11}$ |
|  | E | $7.93\times10^{10}$ |

Table 5.13: The gamma flux per 1μC. The energy spectrum of the gamma-ray is Fig. 5.42.

| Run Number | Ni foil position | Neutron flux per current at foil position (1/cm$^2$/μA) |
|---|---|---|
| Run A | B | $2.45\times10^8$ |
|  | C | $8.51\times10^7$ |
| Run B | A | $3.56\times10^8$ |
|  | B | $1.90\times10^9$ |
| Run D | A | $3.55\times10^8$ |

Table 5.14: The neutron fluxes per 1μC. The energy spectrum of the gamma-ray is referred to Fig. 5.40.

In case of the gamma flux in Table 5.13, the values at the position A was 70 times smaller than that at the position B (run B). This is a simple consequence that the Bremsstrahlung gamma-rays show a strongly forward-peaked angular distribution. The gamma flux shows a position dependence in the vertical direction as shown by the variation for the foils positions, B, D, and E in the run D, where the foil D and E were set at 10mm up and down with respect to the foil B. The experimental results on the relative ratio $\Phi_D/\Phi_B$ and $\Phi_E/\Phi_B$ were 0.873 and 0.324, respectively, while the Monte Carlo simulation predicted 0.540 and 0.543. This discrepancy may be caused by a small miss-alignment of the foils with respect to the beam spot. For instance, if the foils were lower than 5mm with respect to the beam spot, the above discrepancy can be removed.

On the other hand, the observed position ratios, B/C, are 3.20 and 2.49, while the calculated results are 2.80 and 2.49, respectively. From this result, it is concluded that the difference between the calculation and activation analysis is less than 15% as far as the relative intensity is concerned. The Ta target thicknesses, with 15 mm and 29 mm can also be compared to check the validity of the calculation; the flux ratios, 15 mm/29 mm were 4.33 and 3.37, for the position B and C, while the calculation predicted 4.53 and 3.92, respectively. This result also ensures that the calculation properly reproduce the experimental results within 15% accuracy.

On the contrary, concerning the absolute fluxes there seems still discrepancy with a factor 2 between the calculation and activation analysis as exemplified by the ratio $\Phi_{exp}/\Phi_{calc}$ was 0.423 in case of the position B of runB. This entanglement was solved in terms of the correction of the $^{197}$Au(γ,n)$^{196}$Au cross section as follows. Though we used the $^{197}$Au(γ,n)$^{196}$Au cross section (Fig. 5.20) in the activation analysis assuming that the competing $^{197}$Au(γ,np) $^{195}$Pt cross section is negligible. However, if this assumption does not hold, and sizable amount of the cross section is present for the $^{197}$Au(γ,np)$^{195}$Pt reaction, we must modify the calculation of $\Phi_{exp}$, i.e., use of smaller cross section for the $^{197}$Au(γ,n)$^{196}$Au reaction hopefully makes $\Phi_{exp}$ reduced, thus $\Phi_{exp}/\Phi_{calc}$ will be closing to unity. Since the reaction threshold energy of the $^{197}$Au(γ,np)$^{195}$Pt reaction is 13.7 MeV[54], a considerable part of the $^{197}$Au(γ,np)$^{195}$Pt must contribute to the sum cross section of the $^{197}$Au(γ,n)$^{196}$Au + $^{197}$Au(γ,np)$^{195}$Pt reaction shown as the black curve in Fig. 5.19. The authors of ref.[63] reported on the experiment similar to ours. They measured the $^{197}$Au(γ,n)$^{196}$Au reaction from the yields of $^{196}$Au by using the Bremsstrahlung gamma-rays produced by the 30 MeV electron on the iron target with 23.8 mm thickness and they deduced the ratio between the experiment and calculation, $\Phi_{exp}/\Phi_{calc}$ to be 0.476. They criticized that the effect caused $^{197}$Au(γ,np)$^{195}$Pt should be taken into account. Taking into account the $\Phi_{exp}/\Phi_{calc}$ value of ref.[63], we obtained the improved value 0.889 for $\Phi_{exp}/\Phi_{calc}$ for position B of run B. As the results, the gamma flux from activation analysis and simulation agreed within 30% for all measurement. The gamma fluxes, before correction, corrected $^{197}$Au(γ,np)$^{195}$Pt, and obtained by simulation are listed in Table 5.15.

| Run Number | Au foil position | Gamma flux (1/cm$^2$/μA) | Corrected Gamma flux (1/cm$^2$/μA) | Simulation (1/cm$^2$/μA) |
|---|---|---|---|---|
| Run A | B | $6.52\times10^{10}$ | $1.37\times10^{11}$ | $1.47\times10^{11}$ |
|  | C | $2.61\times10^{10}$ | $5.49\times10^{10}$ | $6.06\times10^{10}$ |
| Run B | B | $2.82\times10^{11}$ | $5.93\times10^{11}$ | $6.66\times10^{11}$ |
|  | C | $8.81\times10^{10}$ | $1.85\times10^{11}$ | $2.38\times10^{11}$ |
| Run D | B | $2.45\times10^{11}$ | $5.14\times10^{11}$ | $6.66\times10^{11}$ |

Table 5.15: The gamma flux per 1μC. The energy spectra are assumed as Fig. 5.42.

Table 5.14 shows the neutron fluxes deduced from the activation analysis. The neutron fluxes are about 100 times smaller than the gamma flux.

Attention should be paid on the deduction of neutron flux, because strong gamma-rays can produce $^{58}$Co via the $^{60}$Ni(γ,np)$^{58}$Co reaction though the reaction threshold is high, 20.0 MeV. This may cause some ambiguity in the neutron flux. It should be stressed that the measurement at the position A, where the strong gamma-rays do not reach hopefully gives better accuracy for the neutron flux.

### 5.3.2.4 Radiation dose (Heat load)

The deposited energies due to the radiations are calculated according to the discussion in the preceding section. The procedure to deduce the radiation dose is as follows: In the preceding section, we obtained the gamma flux as cited in Table 5.9, and the radiation doses as cited in Table 5.10 and Table 5.11. On the other hand, we have a relation between the flux and radiation dose as written by

$$D_{\mathrm{exp}} = \Phi_{\mathrm{exp}} \frac{D_{calc}}{\Phi_{calc}} \tag{5.16}$$

where $D_{\mathrm{exp}}$ is the radiation dose per unit beam current, and $\Phi_{\mathrm{calc}}$ is the total gamma flux, $D_{\mathrm{calc}}$ is the calculated radiation dose per unit beam current, and $\Phi_{\mathrm{exp}}$ is the gamma flux obtained by the activation analysis as cited in Table 5.15.

Since the gamma flux measured by the activation analysis is cited in Table 5.15, the radiation doses can be determined comparing these result. Here, we adopted corrected $\Phi_{\mathrm{exp}}$ by the factor given by ref.[63]. The validity of the above procedure can be checked by comparing the observed heat load on the cryostat.

The dose induced by the neutrons is also calculated by using the Monte Carlo simulation and the results are cited in Table 5.12. To avoid the influence of the $^{60}$Ni(γ,np)$^{58}$Co reaction, the neutron flux measured by the Ni foil positioned at the position A were used for evaluation of $\Phi_{\mathrm{exp}}$. Through the Monte Carlo simulation, the neutron flux at the position A, $\Phi_{\mathrm{nA}}$ is deduced by using the neutron production from the target center, $P_{\mathrm{n}}$, as

$$\Phi_{nA} = 3.30 \times 10^{-3} P_n \tag{5.17}$$

Using $\Phi_{\mathrm{nA}}$ in Table 5.14, the radiation dose can be obtained. The produced total neutron at the target is approximately $5.76\times10^{11}$ n/μA which corresponds to the radiation dose of $6.01\times10^{-5}$ mW/g/μA on $D_2$. In fact, this value is negligibly small. From these results, it is concluded that almost all the dose component was caused by not the neutrons but the gamma-rays. The radiation doses on $D_2$ caused by gamma ray are tabulated in Table 5.16.

| Run Number | Au foil position | Dose from raw gamma flux (mW/g/μA) | Dose from corrected gamma flux (mW/g/μA) | Dose from Simulation (mW/g/μA) |
|---|---|---|---|---|
| Run A | B | 0.416 | 0.874 | 0.935 |
|  | C | 0.403 | 0.846 | 0.935 |
| Run B | B | 1.87 | 3.94 | 4.41 |
|  | C | 1.63 | 3.43 | 4.41 |
| Run D | B | 1.63 | 3.40 | 4.41 |

Table 5.16: Deduced Dose on $D_2$ by the gamma-rays per 1μC.

The comparison of the observed heat loads with the calculated ones for the 2nd stage cryostat allows the validity check on the radiation doses in Table 5.16. The calculated heat loads are shown in Table 5.10 and Table 5.11. On the other hand, the heat loads can be experimentally decided by comparing the heater power attached to the cold finger of the cryostat with irradiation and that without irradiation. Since during each run, these powers have been recorded, the heat loads on the cryostat could be deduced as listed in Table 5.17.

It is found that the heat loads calculated based on the original gamma flux, i.e. no correction due to the $^{197}Au(\gamma,np)^{195}Pt$ reaction was applied, gave about 2 times smaller value than the measured one. However, it one uses the improved gamma flux, the calculated heat load shows a good agreement with the measured one. Thus, we could conclude that overall consistency exists between the measurement and the Monte Carlo simulation.

| Run Number | Beam current at measured point (μA) | Heat load on cryostat (W) | Heat load from Raw gamma (W) | Heat load from corrected gamma (W) | Heat load from simulation (W) |
|---|---|---|---|---|---|
| Run A | 170 | 4.9 | 1.92 | 4.04 | 4.34 |
| Run B | 39 | 2.6 | 1.38 | 2.53 | 2.84 |
| Run D | 63 | 3.9 | 1.69 | 3.55 | 4.60 |

Table 5.17: The heat load on cryostat obtained by decrease of heater power.

As the result, we adopt the heat load from corrected gamma of run B shown in Table 5.16. The errors are determined as 30% as difference between the calculation and experiment.

## 5.4 Change of ortho fraction caused by radiation dose

As shown in the result of Sec5.3, the ortho fraction is measured as a function of the radiation dose in $D_2$. This is shown in Fig. 5.44. The data seem to decrease linearly against the dose and there seem no beam power dependence. This behavior strongly suggests that the catalyzing effect is less important. Thus, the linear fitting of run A, B and D gives

$$k=1.37\pm0.44\times10^{-5}P \text{ g/J} \quad (5.18)$$

where P is a radiation dose in unit of W/g. It is remarkable that k value was 4.7 times larger than that calculated by eq. (3.26), $0.289\pm0.20\times10^{-5}P$ (g/J).

The gradients were 4 times larger than the expected value in eq.(3.26). This result is discussed in Chapter 6.

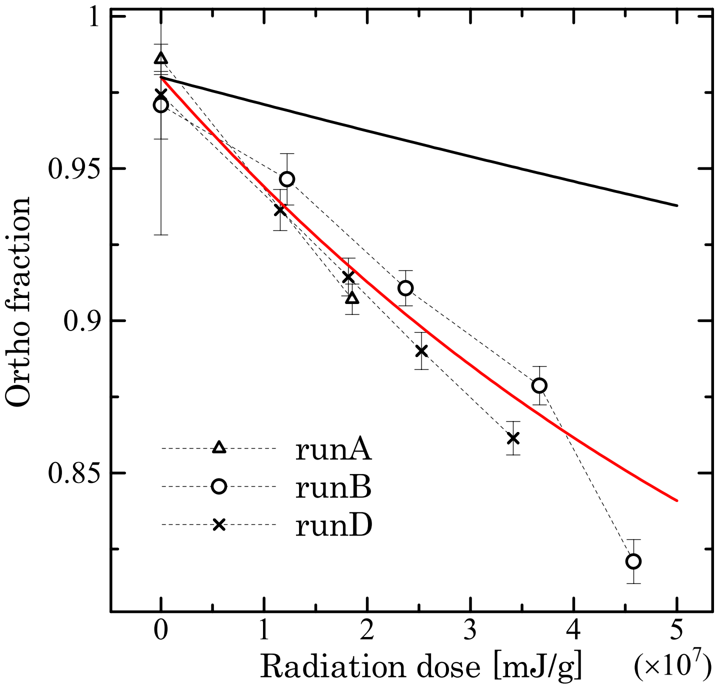

Fig. 5.44: The ortho fractions are plotted against the radiation dose. The red curve is the theoretical curve (eq.(3.38)) obtained so that the curve fits the experimental data. The black curve is the theoretical curve (eq. (3.38)) using k value measured by the tritium gas[22][31].

The results of this experiment can deduce not only the k value but also $\beta^*$ by fitting of eq.(3.42) though it is not precise value due to shorter measurement time. The plots of ortho fraction against irradiation time are shown in Fig. 5.45 and Fig. 5.46 for runB and runD, respectively. In case of runB, the 5th data point showed lower ortho fraction whose reason cannot be understood. Thus two fitting, using the 5th data and ignoring the data, have been done for runB. The most probable $\beta^*$s obtained by fitting are $\beta^*=0$ $s^{-1/2}$ for all analysis. These errors of fittings are $8.42\times10^{-5}$, $4.14\times10^{-4}$, and $4.53\times10^{-4}$ $s^{-1/2}$, for analysis of runB using 5th data, not using 5th data, and runD respectively. The latter two values are consistent with the value deduced by ref.[13].

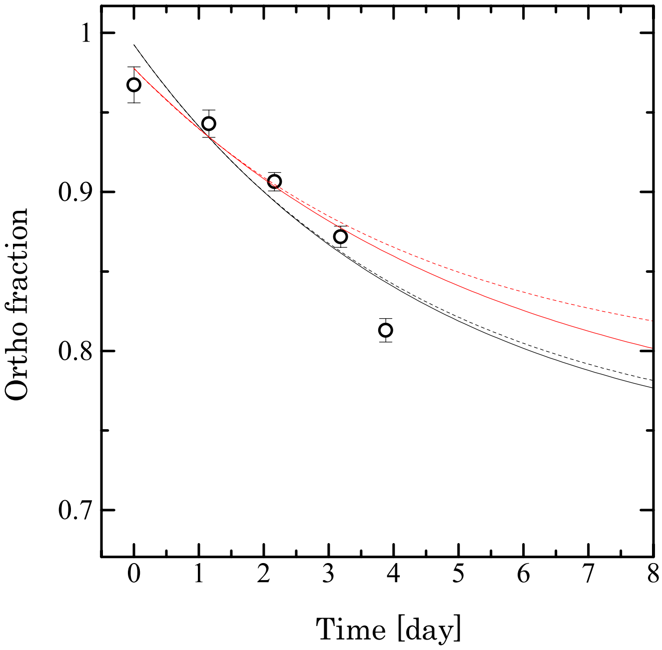

Fig. 5.45: Fitting of runB using eq.(3.42). The black lines are fitting curve of most probable (solid) and one sigma error (dot) using 5th data point. The red lines are analysis ignoring the 5th data point.

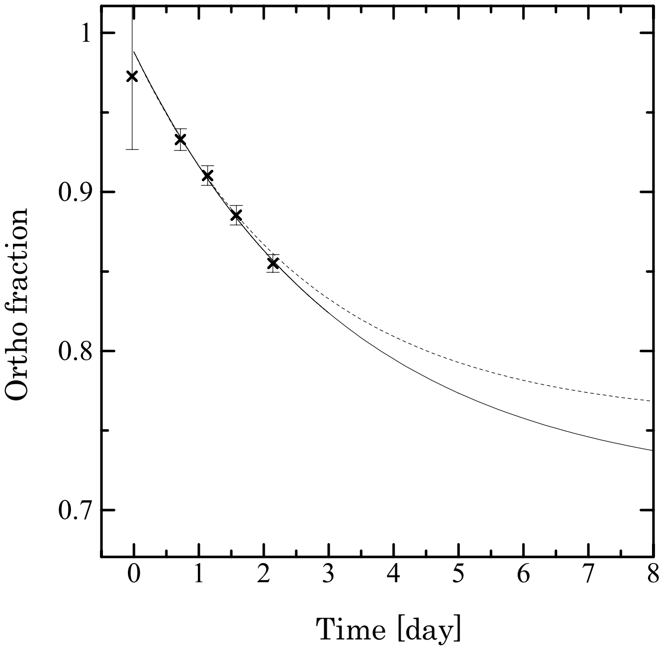

Fig. 5.46: Fitting of runB using eq.(3.42). The lines are fitting curve of most probable (solid) and one sigma error (dot).

# Chapter 6 Discussion

In Sec. 6.1, the possible mechanisms of the irradiation effect on the ortho/para conversion are discussed on the basis of the experimental results presented in the preceding chapters in terms of the model proposed so far. It is found that seriously large discrepancies exist between the old model and our experimental results. Therefore, in Sec. 6.2 and Sec. 6.3, we propose a novel model to disentangle the above inconsistency.

Finally, Sec. 6.4 is devoted to the discussion on the estimated values of the practical UCN density expected for the PSI UCN source on the basis of our model.

## 6.1 Evaluation of the experimental data

We have measured the ortho/para radiation-induced conversion of $D_2$, either time integratedly at PSI, or time differentially at KURRI. In Sec.3.3.3 we presented a model accepted so far for the ortho/para conversion due to the irradiation. According to this model, the fraction of ortho $D_2$ is given by eq. (3.42). This is rewritten as follows;

$$c_o(t) = \left(c_o(t=0) - A\right)\exp\left(-t/\tau\right) + A \tag{6.1}$$

As the experimental results at KURRI in Sec5.4 demonstrate, the time devoted to the measurement was so short (at most less than a week) that the steady state might not be realized. Consequently, the KURRI experiment gave information only on the conversion time $\tau$ of the ortho to para $D_2$. On the other hand, from the PSI experiment, information only on the steady state could be extracted because the measurement time was enough long (over few months) to realize the steady state, while no data on the time dependence, $c_0(t)$, was taken in the PSI experiment. Thus, combining above two results (PSI, KURRI), variables in eq. (6.1), i.e., $\tau$ and A can be determined.

Meanwhile, as eqs. (3.39) and (3.40) demonstrate, $\tau$ and A are, respectively, expressed by the further parameters, i.e., k, $\beta^*$,$\beta_{nat}[D_2]$ as

$$\tau = \frac{1}{k + \beta^* \sqrt{k} + \beta_{nat}[D_2]} \tag{6.2}$$

and

$$A = \tau \left( c_o^{eq}(T) \left( \beta^* \sqrt{k} + \beta_{nat}[D_2] \right) + \frac{2}{3} k \right) \tag{6.3}$$

As discussed in Sec.5.4, the breakup rate for the molecule k could be approximated by the inverse of $\tau$ because of smallness of other terms in eq. (6.2). Then, the value of k obtained from the radiation dose by using eq.(5.18) was 4.0 times larger in comparison with the expected value from eq. (3.39). The reason of the discrepancy is discussed in Sec.6.2.

On the other hand, the results of the PSI experiment provide an ortho fraction at steady state which is sensitive to the catalyzing effect according to eq.(4.24). To see it more closely, we show the relation between k and other terms sensitive to the catalyzing effect by solving the simultaneous equations (3.39) and (3.40). The result is shown by

$$\beta^* \sqrt{k} = \beta_{rad}[D] = \frac{(A - 2/3)k}{c_o^{eq}(T) - A} - \beta_{nat}[D_2] = 1.44 \pm 0.48 \times 10^{-6}\ s^{-1} \tag{6.4}$$

where the $\beta_{nat}[D_2]$ was used to be $0.9\times10^{-7}\ s^{-1}$ given by the discussion in Sec. 3.3.1.

Meanwhile, according to the discussion of ref. [13], $\beta_{rad}[D]$ was deduced as

$$\beta_{rad}[D]=2.36\pm0.64\times10^{-7}\ s^{-1} \tag{6.5}$$

by evaluating eq. (3.40) using k of eq. (3.26).

On the other hand, $\beta_{rad}[D]$ deduced from eq.(6.4) was 5.1 times larger than that deduced from eq. (6.5). If the PSI-SINQ $D_2$ moderator contains a catalyzing contamination such as oxygen, the $\beta_{rad}[D]$ should be larger. In Fig. 6.1 and Fig. 6.2, we show the re-calculated results of ortho fraction for the PSI-SINQ $D_2$ moderator plotted as a function of time. The dependences of ortho fraction on the radiation dose for the steady state are also re-calculated and shown in Fig. 6.2.

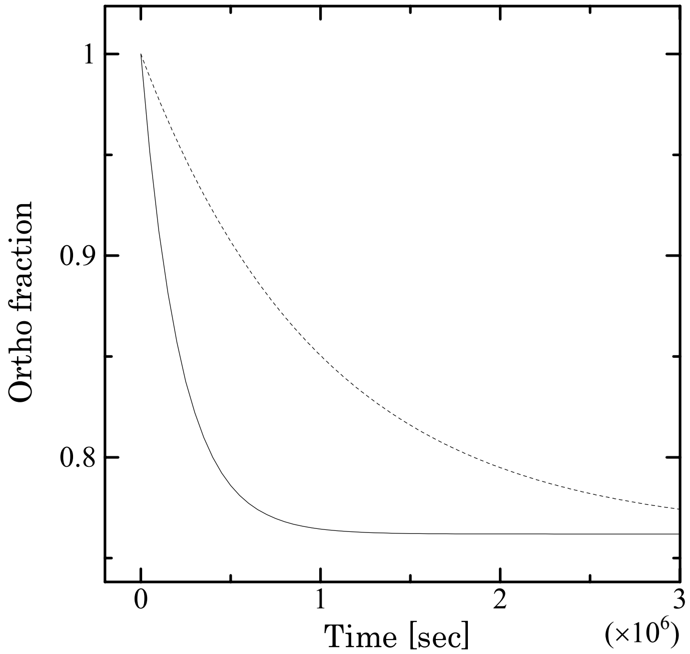

Fig. 6.1: The time dependence of the ortho fraction in PSI-SINQ moderator. The solid line is the calculation used k measured in KURRI, and the dashed line is the calculation used by expected value in ref.[13]

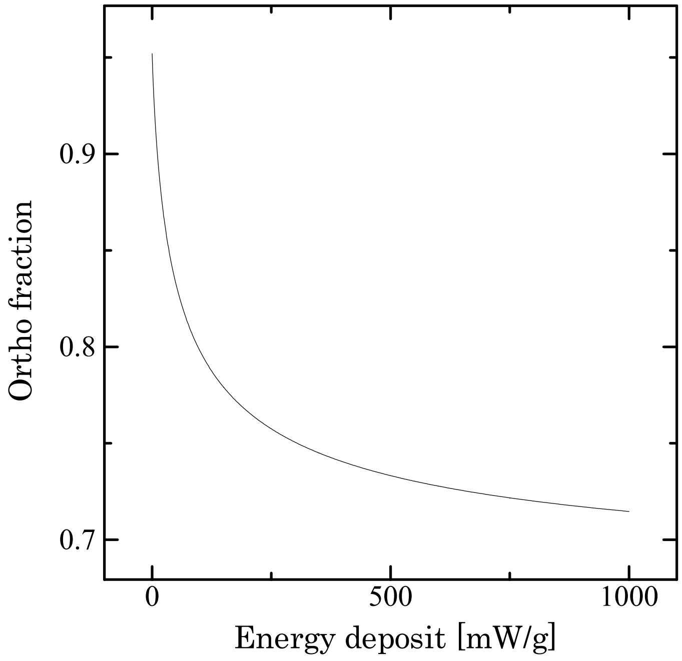

Fig. 6.2: The radiation dose dependence of the ortho fraction in PSI-SINQ moderator at 25K.

## 6.2 Microscopic description of ortho/para conversion mechanism

A large discrepancy has been observed for the molecular breakup rate, k. The given in eq.(3.26) must be temperature independent because the reaction described in eq.(3.25) is a high energy process which is not affected by the surrounding molecules. Though in principle the neutron scattering can change the nuclear state (ortho/para) directly, the neutron fluxes, as measured by the activation analysis, were estimated to be negligibly small, e.g., ~$10^{10}$ n/cm$^2$/sec. Therefore, the neutron effect on k was only an order of $10^{-13}$ s$^{-1}$ (c.f. k~$10^{-7}$ s$^{-1}$ at 100mW/g) even if one assume that the neutrons induce the ortho/para conversion with 100% probability.

The failure of the model in Sec.3.3.3, which was introduced in order to reproduce the present experimental results, strongly suggests insufficiency of the above model and needs for revised models underlying the correct physical basis. In the next paragraph, a new model to disentangle the above phenomena is presented.

Before going to the main issue, we must look back on the assumptions employed in the former model. The former model assumed that the ortho/para conversion was induced by the recombination of atoms after the molecular breakup following the irradiation. On the basis of the microscopic model discussed in Chap. 19 of ref. [22], the above expression is rewritten in a microscopic description as follows. The energy deposited by the radiations like gamma-rays or neutrons, is consumed mainly in the electron dissociation. The produced free electrons are known to make a number of ion pairs proportional to the electron energy, whose aspect is valid for the electron kinetic energy down to 100 eV[22]. A typical kinetic energy of the dissociated electron is more than 100 keV, the number ion pairs amounts a considerable number as indicated below.

Until now, the discussion is concerned with the radiation processes for $H_2$. However, the above characteristic behavior holds also on $D_2$. According to the calculation of ref. [22], possible processes and associated numbers of ion pairs induced by the 100 keV electron beam are, respectively, given by

$$
\begin{array}{lc}
\textit{process} & \textit{number of event} \\
H_2 \rightarrow H_2^{\;+} + e^- & 2377 \\
H_2 \rightarrow H^+ + H + e^- & 341 \\
H_2 \rightarrow 2H^+ + 2e^- & 14
\end{array}
\qquad (6.6)
$$

The number of events per unit energy asymptotically increases with the initial electron energy, and the energy needed for production of one ion pair is known to be 36.6 eV/ion at[32][33]. It is also known that in addition to the processes in eq. (6.7), $H_2$ has a sizable probability of excitation and the excited $H_2$, i.e., $H_2^*$ obeys the following disintegration processes.

$$
\begin{array}{lc}
\textit{process} & \textit{number of event} \\
H_2^{\;*} \rightarrow H_2 + h\nu & 1788 \\
H_2^{\;*} \rightarrow 2H & 740 \\
H_2^{\;*} \rightarrow H^* + H & 614 \\
H_2^{\;*} \rightarrow 2H^* & 28
\end{array}
\qquad (6.7)
$$

for incidence of 100 keV electron.

The hydrogen ions, $H^+$ and $H_2^+$, produced in the process of eq. (6.6) react with $H_2$ as

$$H_2^{\;+} + H_2 \rightarrow H_3^{\;+} + H \qquad (6.8)$$

and

$$H^+ + 2H_2 \rightarrow H_3^{\;+} + H_2 \qquad (6.9)$$

Above reactions should not be the binary but three body reaction due to the energy and momentum conservations. This may change the ortho/para of the third body by exchanging hydrogen. In the final stage, the produced $H_3^+$ ion dissociates to the 3H atoms followed by the electron capture

$$H_3^{\;+} + e^- \rightarrow H_2^{\;*} + H \rightarrow 3H \qquad (6.10)$$

In summary, a 100 keV electron is estimated to totally produce the $1.37\times10^4$ H atoms. This number agrees well with the experimental result, $1.39\pm0.08\times10^4$ H/ 100keV which is cited in ref. [31].

On the basis of the above scenario, we will think about the catalyzing effect of $H_3^+$ atom. A possible catalyzing reaction by $H_3^+$ is considered to be

$$H_3^+ + ortho - H_2 \rightarrow H_3^+ + para - H_2 \quad (6.11)$$

No one so far has pointed out his possibility in liquid or solid. In case of gas, the enhancement of conversion has been reported in ref.[64], in which they reported that from the irradiation effect by the gamma rays with $1.6\times10^5$ Gy on the para-$H_2$ gas especially for the 15 MPa sample a conversion enhancement was observed. This is shown in Table 6.1. The enhancement in the third column means the conversion effect compared with eq. (3.26).

| Temperature | Increased ortho fraction | Enhancement compared with eq. (3.26) |
|---|---|---|
| 77 K | 0.14 ± 0.24% | 2.2 ± 3.7 |
| 195 K | 41.5 ± 14.6% | $1.7 \pm 0.6\times10^3$ |
| 293 K | 51.9 ± 14.9% | $2.5 \pm 0.7\times10^3$ |

Table 6.1: The results of gamma irradiation referred from ref.[64] for 15 MPa. The irradiated dose was $1.6\times10^5$ Gy.

Remarkable enhancements of the conversion rate at 293 and 195 K can be explained by the hydrogen exchange reaction of $D_3^+$. According to ref.[22], $D_3^+$ induces a reaction

$$D_3^+ + T_2 \rightarrow D_2T^+ + DT \quad (6.12)$$

as a chain reaction occurring in $D_2$-$T_2$ gas, and it is known that one $D_3^+$ ion induces 2000 exchange reactions at room temperature. This number qualitatively corresponds to the enhancement factors in Table 6.1.

On the contrary, the enhancement seems to disappear at the lowest temperature, 77 K. Because the para to ortho conversion process for $H_2$ requires an energy of 172 K, the chain reaction cannot be induced at this lowest energy, which results in the reduction of enhancement factors.

When this discussion is applied to our case, i.e. $D_2$, it is found that the ortho to para conversion in $D_2$ in liquid and solid phases are energetically impossible since the conversion energy is 86 K.

However, the conversion due to $D_3^+$ produced by the reaction,

$$D_2^+ + D_2 \rightarrow D_3^+ + D \quad (6.13)$$

can be possible because the averaging reaction energy is 1.5 eV according to the calculation of [66][67]. In fact, the produced $D_3^+$ can convert the ortho-$D_2$ to para-$D_2$ until it is thermalized.

In addition, the dissociated atoms followed by the reaction,

$$\underline{D_3^+ + e^- \rightarrow D_2^* + D \rightarrow 3D} \quad (6.14)$$

may also contribute to the $D_2$ conversion because the reaction energy is 4.2 eV. It is assumed that the conversions caused by the above mentioned reactions must be temperature independent as far as it is concerned with the low temperature region of the present interest.

As the other candidate to explain the enhancement, we can think the larger atom creation rate than used value in our model, 5.1/ion pair. The authors of ref. [68] estimated that the $H_2$ k value was 3.6 times larger than that of $D_2$ based on ref. [69]. In ref.[69], the deduced ortho/para conversion rate was $2.59\times10^{-6}$ mol/J, which is relatively closer with our result, $k=3.48\pm1.11\times10^{-6}$ mol/J.

For other possibility is the wall effect. Ref[70] reported irradiate $\gamma$-$Al_2O_3$ induce the $H_2$-$D_2$ exchange. If this kind of process occurs at copper wall of irradiation cell, the ortho-$D_2$ can be changed to para-$D_2$ by $D_2$-$D_2$ exchange reaction. This effect is expected to decrease in larger volume because the volume increase as cube of diameter though the surface area increase only as square of the diameter.

These models are evaluated in next section.

## 6.3 Discussion about the models

In Sec. 6.2, we have discussed the microscopic mechanism based on the creation and annihilation of atoms, ions and electrons to explain unexpected enhancement of $D_2$ ortho/para conversion due to irradiation. In this subsection, we will continue the above discussion to establish a new concept to comprehensively reproduce data so far.

As discussed in the former section, we have three candidates to explain the unexpected enhancement of ortho to para conversion in liquid $D_2$ phase due to irradiation. They are;

1) exchange of $D_3^+$ or D atoms with $D_2$,
2) creation of D atoms more than estimated value
3) enhancement by wall effect

In the following each item will be treated individually.

1) Exchange of $D_3^+$ or D atoms with $D_2$

As discussed in Subsec.3.3.3 and Subsec.3.3.4, we assumed that the dominant reactions were those reactions expressed by eqs.(3.25),(3.27). We need additional reactions associated with $D_3^+$ and D which have not been considered so far,

$$D_3^+ + ortho - D_2 \to D_3^+ + para - D_2 \tag{6.15}$$

$$D + ortho - D_2 \to D + para - D_2 \tag{6.16}$$

For the sake of discussion below, we define a parameter, $\chi$ to represent the sum number of exchange reactions induced by $D_3^+$ and D, where we do not distinguish the reactions induced either by $D_3^+$ or D. It is experimentally verified that the $D_3^+$ produced by the reaction of eq.(6.13) conserves the initial spin statistics[71]. The effect of spin statistics is caused by the reactions given in eq.(6.13) and subsequent exchange reactions accompanying either with the deuteron hopping reaction,

$$\widetilde{D}_2 + D_3^+ \to +\widetilde{D}_2 D^+ + D_2^+ \tag{6.17}$$

or with the deuterium exchange reaction

$$\widetilde{D}_2 + D_3^+ \to D_2 \widetilde{D}^+ + D\widetilde{D} \tag{6.18}$$

The calculation of the spin statistics is given in ref.[72]. Here, we define the ortho molecule production ratio per one exchange reaction, $\varepsilon$. When the spins of the exchanged atoms are in a perfectly random distribution, the $\varepsilon$ is 2/3. If the exchange of $D_3^+$ are a dominant process, $\varepsilon$ takes a larger value than 2/3 due to the residuals of the spin statistics. $\varepsilon$ must be a function of $[D_2^o]$, but we fixed the $\varepsilon$ as 2/3 for simplification of the model.

By using the $\chi$, eq.(3.30) is modified as

$$\frac{d[D_2{}^o]}{dt} = -\left(k(\mathbf{1}+\boldsymbol{\chi}) + \beta_{rad}[D] + \beta_{nat}[D_2]\right)[D_2{}^o] + \frac{2}{3}\mathbf{k}\chi[D_2] \\ + c_o{}^{eq}(T)\left(\beta_{rad}[D] + \beta_{nat}[D_2]\right)[D_2] + \frac{2}{3}\alpha[D]^2 \tag{6.19}$$

where we follow the same parameters of eq.(3.30). We have to consider the catalyzing effect of $D_3^+$. The molar fraction $[D_3^+]$ can be written as

$$\frac{d[D_3{}^+]}{dt} = k[D_2] - \alpha_{D_3^+}[D_3{}^+][e^-] \cong k[D_2] - \alpha_{D_3^+}[D_3{}^+]^2 \tag{6.20}$$

where all ions are assumed to form $D_3^+$. However, the recombination rate of $D_3^+$, $\alpha_{D_3^+}$, is about $10^8$ times larger[22] at 20K, which means that [D] is $10^4$ times larger than $[D_3^+]$. The huge difference of recombination rate is due to the fact that the recombination process of D is the three body process such as

$$D + D + D_2 \rightarrow 2D_2 \tag{6.21}$$

Therefore, it is reasonable that we have neglected the $[D_3^+]$ in eq.(6.19).

The produced number of D is unchanged from the value given by eq.(3.30). Thus, using eq.(3.33), eq.(6.19) is given by

$$\frac{d[D_2{}^o]}{dt} = -\left((\mathbf{1}+\boldsymbol{\chi})k + \beta^*{}_1\sqrt{k} + \beta_{nat}[D_2]\right)[D_2{}^o] \\ + \left(c_o{}^{eq}(T)\left(\beta^*{}_1\sqrt{k} + \beta_{nat}[D_2]\right) + \frac{\mathbf{2}}{\mathbf{3}}(1+\boldsymbol{\chi})k\right)[D_2] \tag{6.22}$$

This differential equation is solved as

$$c_{o1}(t) = \left(c_o(t=0) - A\right)\exp\left(-t/\tau_1\right) + A_1 \tag{6.23}$$

where

$$\tau_1 = \frac{1}{k(1+\chi) + \beta^*{}_1\sqrt{k} + \beta_{nat}[D_2]} \tag{6.24}$$

and

$$A_1 = \tau_1\left(c_o{}^{eq}(T)\left(\beta^*{}_1\sqrt{k} + \beta_{nat}[D_2]\right) + \frac{2}{3}\left(1+\chi\right)k\right) \tag{6.25}$$

2) Creation of D atoms more than estimated value

Eq. (6.22) is almost same as eq.(3.30), except the large k value. In this respect, defining the new molecular breakup rate as $k_2$, the ortho fraction is given by

$$c_{o2}(t) = \left(c_o(t=0) - A_2\right)\exp\left(-t/\tau_2\right) + A_2 \tag{6.26}$$

where

$$\tau_2 = \frac{1}{k_2 + \beta^*{}_2\sqrt{k_2} + \beta_{nat}[D_2]} \tag{6.27}$$

and

$$A_2 = \tau_2\left( c_o^{eq}(T)\left(\beta^*{}_2\sqrt{k_2} + \beta_{nat}[D_2]\right) + \frac{2}{3}k_2 \right) \tag{6.28}$$

3) The enhance occurs by wall effect

The wall effect is expected to be proportional to surface area. Thus, the wall effect decrease as cube root of the volume. In case the SINQ, the volume of $D_2$ is about $10^4$ times larger than KURRI so that the wall effect is 1/20 times. The enhancement factor is 3.7 (4.7 minus 1) at KURRI, thus, the wall effect is less than 20% in SINQ. Therefore we can use almost same equation in theory of Sec.3.3.3.

According to the discussion in the preceding sections, we proposed three models to reproduce the unexpected enhanced ortho fraction. However, eqs. (6.23)~(6.28) show the same behavior as long as the time dependence is concerned. The difference of the models exists only in $\beta^*$. If we neglect the natural and catalyzing effects, the result of Sec.5.4 is rewritten by

$$k(1+\chi) = k_2 = 4.7\ k \tag{6.29}$$

Then, the parameter $\beta^*$ explaining the result of Sec.4.3.3 (76.2% as steady state with the energy deposit of 228 mW/g) can be deduced by eqs.(6.25), (6.28). $\beta^*$ for the case 1) , 2) and 3), i.e., $\beta^*_1$, $\beta^*_2$ and $\beta^*_3$, are, respectively, given by

$$\beta^*_1 = (1.77 \pm 4.48) \times 10^{-3}\ s^{-1/2} \tag{6.30}$$

$$\beta^*_2 = (8.15 \pm 2.24) \times 10^{-4}\ s^{-1/2} \tag{6.31}$$

$$\beta^*_3 = (2.91 \pm 0.55) \times 10^{-4}\ s^{-1/2} \tag{6.32}$$

These different $\beta$ give different [D] values each other by a factor 4.7. Using the extrapolated value from $\alpha$ in solid[37], $1.28\times10^{-13}$ cm$^3$/s, these [D] can be estimated from eqs. (6.3),(6.31). Using the molar density at 25 K, $2.4\times10^{22}$ /cm$^3$, [D] is deduced as

$$[D] = (1.30 \pm 0.23) \times 10^{-8} \text{ for case 1) and 3)} \tag{6.33}$$

$$[D] = (2.83 \pm 0.45) \times 10^{-8} \text{ for case 2)} \tag{6.34}$$

Assuming that the conversion is caused by the dipole-dipole interaction between unpaired elections and deuteron, the value of $\beta_{rad}$ in eq.(6.4) may be approximated by the oxygen catalyzing rate, $\beta_{ox}(D_2)$ of 0.791 $s^{-1}$ from eq.(3.24) at high temperature limit, where $O_2$ is known to be a paramagnetic molecule because its molecular orbital is the $^3\Sigma^-_g$ state. According to eq.(3.21), the conversion probability is proportional to a square of the product of electronic and nuclear magnetic moments, thus, the $\beta_{rad}$ can be deduced as

$$\beta_{rad} = 0.198 \text{ s}^{-1} \tag{6.35}$$

Then, the [D] for the PSI-SINQ moderator generated the irradiation of 228 mW/g at T=25 K is given by

$$[D] = 1.82 \pm 0.67 \times 10^{-6} \qquad \text{for 1) and 2)} \tag{6.36}$$

$$[D] = 2.99 \pm 1.10 \times 10^{-7} \qquad \text{for 3)} \tag{6.37}$$

The above value corresponds to 1.8 ppm in liquid $D_2$ moderator, which is relatively closer to the value of case 1) and 2). The model 3) shows best agreement, however, it is over an orders of magnitude larger than that estimated from eqs.(6.33),(6.34). This probably suggests that estimation of $\alpha$ or $\beta_{rad}$ is insufficient. Due to the large discrepancy exists between the results, we can not determine which model is better. The precise experiment on $\alpha$ or $\beta_{rad}$ makes it possible to answer this question.

## 6.4 Irradiation effect on PSI UCN source based on $sD_2$

The discussion so far has been concerned with irradiation effect of liquid $D_2$. However, the practical UCN source now planned such as at PSI will use not liquid $D_2$ but solid $D_2$, $sD_2$. Therefore, it is of particular importance to calculate the performance of UCN source extrapolating our results deduced from the liquid $D_2$ to the $sD_2$.

In this section, we speculate possible ortho fraction for the irradiated solid $D_2$ using the established model in the preceding sections. Here, we use the catalyzing conversion rate measured by the solid $D_2$-$T_2$[15]. For the $D_2$ under the radiation dose of 250mW/g, the conversion time was calculated to be 5.7±1.3 hour around 4 K. The minimum conversion time, 2.2 hours was found at 10K. The steady state of ortho fraction is given by eqs.(6.25),(6.28). At steady states, there is essentially no difference in the ortho fraction even if $\beta^*$ is different each other depending on the model. $\beta^*$ at low temperature can be deduced from this experiment as $2.86\pm0.78\times10^{-2}$ $s^{-1/2}$. By using the temperature independent k of eq.(5.18) (see Sec.6.2), the steady state of the ortho fraction, A, is given by

$$A(4.2K)=\tau\left(2.86\times10^{-2}[\sqrt{s}]\times\sqrt{1.37\times10^{-5}P[g/J]}+\frac{2}{3}\times1.37\times10^{-5}P[g/J]\right) \quad (6.38)$$

where τ is the time constant given by

$$\tau=\frac{1}{2.86\times10^{-2}[\sqrt{s}]\sqrt{1.37\times10^{-5}P[g/J]}+1.37\times10^{-5}P[g/J]} \quad (6.39)$$

Here, the $C_p^{eq}(4.2K)=2\times10^{-9}$ and the $\beta_{nat}=1.5\times10^{-7}$ $s^{-1}$ are neglected in these equations. The P is the radiation dose in unit of W/g. The A(4.2 K) and τ as the function of P is plotted in Fig. 6.3 and Fig. 6.4.

According to ref.[23], the radiation dose for the UCN source at PSI is estimated to be 72.7 mW/g for continuous operation. The radiation dose induces the conversion time of 9.38 hours and the ortho fraction of 0.988 at the steady state. In case the duty factor is 1/100, and the pulsed operation can be assumed not to make different effect with continuous run, the conversion time can be estimated as 4.03 days. Then, it result ortho fraction as 0.9987 (para fraction as $1.3\times10^{-3}$).

From the Fig. 2.3, this para fraction induce 1.4 sec by the up-scattering processes associated with the para to ortho conversion. This lifetime is enough small comparing to the neutron capture of deuteron, 146 msec. The total lifetime of UCN can be, then, expected to be 98 msec at 4.2 K. While it is 32 msec at 8.0 K due to the up-scattering of the ortho-$D_2$ itself. Using the production rate of eq. (2.33) and the lifetime of UCN at 4.2 K, the UCN density of the UCN source at PSI can be expected as

$$\rho_{UCN}=3.1\times10^4\ /cm^3 \quad (6.40)$$

in the solid $D_2$.

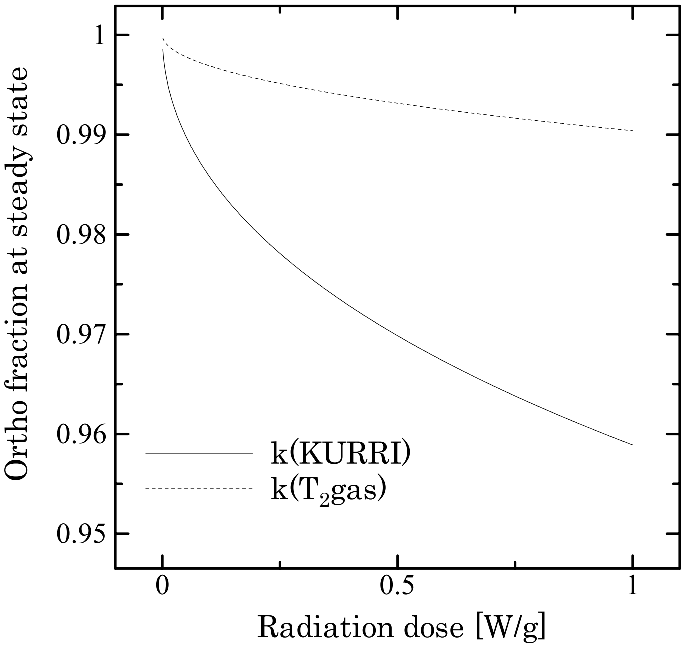

Fig. 6.3: The ortho fraction at steady state for 4.2 K solid $D_2$ plotted as a function of the radiation dose calculated based on eq.(6.38). The solid line is the calculation used the k value of eq.(5.18), and the dashed line is the calculation used eq. (3.26).

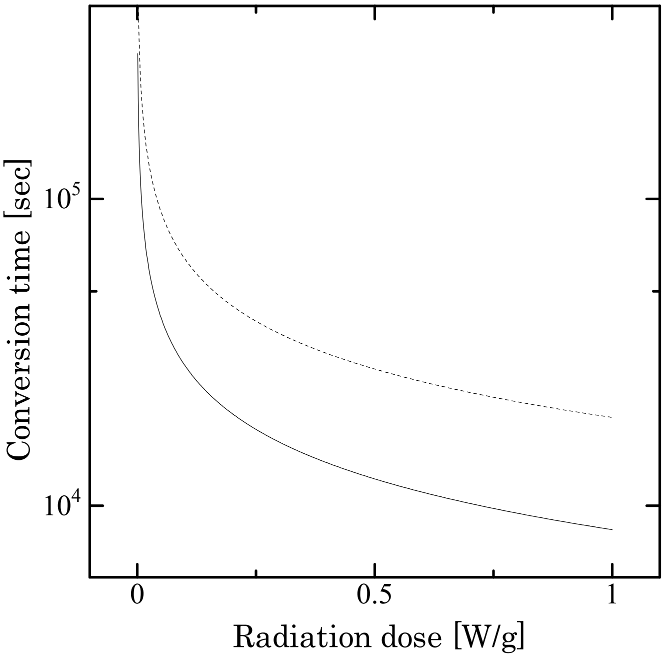

Fig. 6.4: The conversion time for 4.2K solid $D_2$ as a function of the radiation dose calculated based on eq.(6.39). The solid line is the calculation used the k value of eq.(5.18), and the dashed line is the calculation used eq. (3.26).

## 6.5 Suppression of ortho to para conversion and miscellaneous problems

The ortho fraction at the steady state indicates, as described in Fig. 6.2, that the radiation effect may be significant with the radiation field of 1 W/g. If this really happens, an oxygen doping may be one of the solution to suppress the increase of para-$D_2$. In fact, the oxygen is known to induce a large catalyzing effect[29],[73], and its estimated conversion rate $\beta_{ox}(D_2)$ is about 0.8 $s^{-1}$ above 8 K from eq.(3.24). Thus, for example, 1000ppm in mol fraction of oxygen doping may induce the conversion time of 1300 sec and bring up the steady state to 0.995. Note that the conversion rate $\beta_{ox}$ is exponentially decrease with temperature, and the value at 5 K is ~ $10^{-2}$ $s^{-1}$. On the other hand, we must pay attention on the neutron capture by oxygen. The neutron capture cross section of oxygen is 190 μbarn for thermal neutron, which is about 3 times less than deuteron so that the loss by neutron capture is negligible small. This can be a hopeful candidate for suppressing the conversion though there are still technological difficulties in doping and danger of explosion above 4% of admixture of oxygen in hydrogen.

The above discussion showed that the increase of para-$D_2$ is not a serious problem for the UCN source at PSI. However, the above discussion does not include the other radiation effect. As discussed in ref. [74], the atomic density of T in $T_2$ was 200 ppm at 4.0 K and 52 ppm at 8.1 K. By extrapolating these numbers to the UCN source at PSI, the expected atomic densities are 76.3 ppm at 4.0 K and 20 ppm at 8.1 K. These atoms, and produced radicals are known to make the other excitations[75]. The magnetic dipole moment of unpaired electron also interacts with the UCN. Though these effects were found in other UCN sources[10], these effects may induce further UCN loss.

# Chapter 7 Conclusion and future outlook

## 7.1 Conclusion of this work

For the construction of high intensity UCN source using the solid ortho $D_2$, the study on the radiation effect of ortho $D_2$ was essential. In order to study the radiation effect of the solid $D_2$ ($sD_2$) we used a liquid $D_2$, since the radiation effect of solid and liquid is considered to be same. Hence, we measured the radiation induced ortho/para conversion of liquid ortho-$D_2$ by both time integrated and time differential measurements for the first time. For this study, the ortho fractions were precisely measured using a newly developed Raman spectroscopy.

We found that the conversion rate is 4 times larger than the expected value from the molecular breakup rate. This strongly indicates existence of other processes inducing the ortho/para conversion.

In this article, we propose a novel microscopic model to comprehensively understand the large enhancement in the ortho/para conversion. This model was applied to estimate an expected performance of the ortho fraction of $sD_2$ for the UCN source planned at PSI. According to our model calculation, the expected ortho fraction amounts to 0.988 with a practical irradiation level of 72.7 mW/g radiation at PSI. Therefore, the present result indicates that the proposed UCN density at PSI, 2000 UCN/cm$^3$ is realizable.

## 7.2 Future outlook

UCN production with high intensity is awaited by the scientists in the world. Through the present work, importance of the study on the ortho/para conversion by irradiation was clarified for the high intensity UCN production. In the future, further study on the observation of possible differences in the irradiation effect between liquid and solid phases of $D_2$ using the newly developed metrology, Raman spectroscopy with high sensitivity.

# Appendix A Nuclear wave functions for homonuclear diatomic molecules

---

In this Appendix, we discuss the wave functions of the nuclear spin parts for the homonuclear diatomic molecule such as $H_2$ and $D_2$.

## A.1 Statistical weight of ortho and para states

The nuclear spin parts of the wave function for the homonuclear di-atomic molecule is expressed by

$$|\, jm\rangle = \sum_{m1,m2} C(j_1 j_2 j; m_1 m_2 m) \left| j_1 m_1, j_2 m_2 \right\rangle \tag{A.1}$$

where $|jm>$ is a total nuclear spin state and its z-component, $|j_1m_1>$, $|j_2m_2>$ are each nuclear spin and its z-component, and $C(j_1j_2j;m_1m_2m)$ is the Clebsh-Gordan coefficient (C-coefficient) [28]. The C-coefficient has a symmetry property for exchange of $j_1$ and $j_2$ as

$$C(j_1 j_2 j; m_1 m_2 m) = (-1)^{j_1+j_2-j} C(j_2 j_1 j; m_2 m_1 m) \tag{A.2}$$

Therefore, if the term of $(j_1+j_2-j)$, is even, the C-coefficient, and consequently $|jm>$ are symmetric ("**ortho**") for exchange of two nuclei. On the other hand, the C-coefficient, and consequently $|jm>$ are antisymmetric ("**para**") for odd $(j_1+j_2-j)$. In other words, the symmetry property for the two nuclear wave functions is determined by the parity P of $(j_1+j_2-j)$, where P is given by

$$P = (-1)^{j_1+j_2+j} \tag{A.3}$$

Each nuclear spin $j_1$, $j_2$, and the total spin j are either an integer or half-integer. For the homonuclear diatomic molecule such as $H_2$ and $D_2$, $j_1= j_2$, thus,

$$(j_1+j_2-j) =(2j_1+j) \tag{A.4}$$

Therefore, if each nucleus has an integer spin, the parity follows $(-1)^j$. In case that each nucleus has a half-integer spin, the parity is given by $(-1)^{j-1}$. Consequently, the above aspect is summarized by

$$\begin{aligned} P &= (-1)^{j} && \textit{Integral spin} \\ P &= (-1)^{j-1} && \textit{half} - \textit{Integral spin} \end{aligned} \qquad \text{(A.5)}$$

From eq. (A.5), it is found that the total spin of the ortho and para state for $H_2$ and $D_2$ is expressed by Table A.1.

| State<br>Molecule | Ortho | Para |
|---|---|---|
| $H_2$ | j = 1 | j = 0 |
| $D_2$ | j = 2, 0 | j = 1 |

Table A.1: The nuclear spins of molecules and ortho/para state.

The homonuclear diatomic molecule with each nucleus having a spin $j_1$ forms a total nuclear spin j=0,1,2,.......,$2j_1$. The number of the total nuclear spin state with j, g(j), is given by

$$g(j)=(2j+1) \qquad \text{(A.6)}$$

The total number of states Q for summing over all j can be written as

$$Q = \sum_{j=0}^{2j_1} g(j) = (2j_1+1)^2 \qquad \text{(A.7)}$$

Therefore, in case of the homonuclear diatomic molecule, each nucleus of which has an integer spin, the total number of the states with the positive parity (ortho), $Q_o$, and that with the negative parity (para), $Q_p$, are, respectively, given by

$$\begin{aligned} Q_o &= \sum_{even\ j}^{2j_1} g(j) = (j_1+1)(2j_1+1) \\ Q_p &= \sum_{odd\ j}^{2j_1-1} g(j) = (j_1)(2j_1+1) \end{aligned} \qquad \text{(A.8)}$$

by using the selection rule given by eq. (A.5).

On the other hand, $Q_o$ and $Q_p$ in case of a nucleus with a half-integer spin are given by

$$\begin{aligned} Q_o &= \sum_{odd\ j}^{2j_1} g(j) = (j_1+1)(2j_1+1) \\ Q_p &= \sum_{even\ j}^{2j_1-1} g(j) = (j_1)(2j_1+1) \end{aligned} \qquad \text{(A.9)}$$

According to (A.8) and (A.9), the ratio of the number of nuclear spin states can be written as

$$\frac{Q_o}{Q_p} = \frac{j_1 + 1}{j_1} \tag{A.10}$$

## A.2 The nuclear spin wave functions for $H_2$ and $D_2$

The nuclear spin wave functions |jm> for the $H_2$ molecule (two spin 1/2 nuclei) are expressed by eq. (A.1). More simply, they are expressed in terms of the matrix expressions as

$$\begin{array}{cccc}
|jm\rangle & & C-Matrix\ coefficient & |j_1m_1\rangle|j_2m_2\rangle \\
\begin{bmatrix} |1;1\rangle \\ |1;0\rangle \\ |0;0\rangle \\ |1;-1\rangle \end{bmatrix} & = & \left[\begin{array}{c|cc|c} 1 & & & \\ \hline & 1/\sqrt{2} & 1/\sqrt{2} & \\ & 1/\sqrt{2} & -1/\sqrt{2} & \\ \hline & & & 1 \end{array}\right] & \begin{bmatrix} |1/2;1/2\rangle|1/2;1/2\rangle \\ |1/2;1/2\rangle|1/2;-1/2\rangle \\ |1/2;-1/2\rangle|1/2;1/2\rangle \\ |1/2;-1/2\rangle|1/2;-1/2\rangle \end{bmatrix}
\end{array} \tag{A.11}$$

Using eq.(A.11), the explicit expressions for the ortho and para $H_2$ states are given by

$$\begin{aligned}
& j = 1 \quad (Symmetry) \\
& |1;+1\rangle = \left|\frac{1}{2};\frac{1}{2}\right\rangle\left|\frac{1}{2};\frac{1}{2}\right\rangle \\
& |1;\ 0\rangle = \frac{1}{\sqrt{2}}\left(\left|\frac{1}{2};\frac{1}{2}\right\rangle\left|\frac{1}{2};-\frac{1}{2}\right\rangle + \left|\frac{1}{2};-\frac{1}{2}\right\rangle\left|\frac{1}{2};\frac{1}{2}\right\rangle\right) \\
& |1;-1\rangle = \left|\frac{1}{2};-\frac{1}{2}\right\rangle\left|\frac{1}{2};-\frac{1}{2}\right\rangle \qquad (A.12) \\
& \\
& j = 0 \quad (AntiSymmetry) \\
& |0;\ 0\rangle = \frac{1}{\sqrt{2}}\left(\left|\frac{1}{2};-\frac{1}{2}\right\rangle\left|\frac{1}{2};\frac{1}{2}\right\rangle - \left|\frac{1}{2};\frac{1}{2}\right\rangle\left|\frac{1}{2};-\frac{1}{2}\right\rangle\right)
\end{aligned}$$

In a similar way, for the $D_2$ molecule (two spin 1 nuclei), eq. (A.1) is expressed by the matrix expression as

$$\begin{array}{cccc} |jm\rangle & & C-\mathit{Matrix\ coefficient} & |j_1m_1\rangle|j_2m_2\rangle \\ \begin{bmatrix} |2;2\rangle \\ |2;1\rangle \\ |1;1\rangle \\ |2;0\rangle \\ |1;0\rangle \\ |0;0\rangle \\ |2;-1\rangle \\ |1;-1\rangle \\ |2;-2\rangle \end{bmatrix} & = & \begin{bmatrix} 1 & & & & & & & & \\ & 1/\sqrt{2} & 1/\sqrt{2} & & & & & & \\ & 1/\sqrt{2} & -1/\sqrt{2} & & & & & & \\ & & & 1/\sqrt{6} & 1/2\sqrt{6} & 1/\sqrt{6} & & & \\ & & & 1/\sqrt{2} & 0 & -1/\sqrt{2} & & & \\ & & & 1/\sqrt{3} & -1/\sqrt{3} & 1/\sqrt{3} & & & \\ & & & & & & 1/\sqrt{2} & 1/\sqrt{2} & \\ & & & & & & 1/\sqrt{2} & -1/\sqrt{2} & \\ & & & & & & & & 1 \end{bmatrix} & \begin{bmatrix} |1;1\rangle|1;1\rangle \\ |1;1\rangle|1;0\rangle \\ |1;0\rangle|1;1\rangle \\ |1;1\rangle|1;-1\rangle \\ |1;0\rangle|1;0\rangle \\ |1;-1\rangle|1;1\rangle \\ |1;0\rangle|1;-1\rangle \\ |1;-1\rangle|1;0\rangle \\ |1;-1\rangle|1;-1\rangle \end{bmatrix} \end{array} \quad \text{(A.13)}$$

The explicit expressions for the ortho and para $D_2$ states are given by

$\underline{j = 2 \ \ (Ortho)}$

$$|2;+2\rangle = |1;1\rangle|1;1\rangle$$

$$|\,2;+1> = \frac{1}{\sqrt{2}}\left(|1;0\rangle|1;1\rangle + |1;1\rangle|1;0\rangle\right)$$

$$|\,2; \quad 0> = \frac{1}{\sqrt{6}}\left(|1;1\rangle|1;-1\rangle + 2|1;0\rangle|1;0\rangle + |1;-1\rangle|1;1\rangle\right)$$

$$|\,2;-1> = \frac{1}{\sqrt{2}}\left(|1;0\rangle|1;-1\rangle + |1;-1\rangle|1;0\rangle\right)$$

$$|\,2;-2> = |1;-1\rangle|1;-1\rangle$$

$\underline{j = 0 \ \ (Ortho)}$

$$|\,0; \quad 0> = \frac{1}{\sqrt{3}}\left(|1;1\rangle|1;-1\rangle - |1;0\rangle|1;0\rangle + |1;-1\rangle|1;1\rangle\right)$$

$\underline{j = 1 \ \ (Para)}$

$$|\,1;+1> = \frac{1}{\sqrt{2}}\left(|1;0\rangle|1;1\rangle - |1;1\rangle|1;0\rangle\right)$$

$$|\,1; \quad 0> = \frac{1}{\sqrt{2}}\left(|1;-1\rangle|1;1\rangle - |1;1\rangle|1;-1\rangle\right) \qquad \text{(A.14)}$$

$$|\,1;-1> = \frac{1}{\sqrt{2}}\left(|1;0\rangle|1;-1\rangle - |1;-1\rangle|1;0\rangle\right)$$

# Appendix B　Energy levels of diatomic molecules

---

In this chapter, we give formalisms on the energy levels for the diatomic molecules such as $H_2$, $D_2$ and HD.

## B.1 Energy levels

Energy levels of the diatomic molecule are given by

$$E_{total}(v,J) = E_{vib}(v) + E_{rot}(v,J) \tag{B.1}$$

where v is a principal quantum number of the vibrational state, J is the angular momentum of the rotational state.

The v^th^ vibration energy state is expressed by

$$E_{vib}(v) = h\left\{ v_e(v+\frac{1}{2}) - x_e(v+\frac{1}{2})^2 + y_e(v+\frac{1}{2})^3 \right\} \tag{B.2}$$

where $v_e$, $x_e$, and $y_e$ are tabulated in Table.B.1.

If v is equal to 0, E(vib) has a non-zero value and expressed by

$$E_{vib}(0) = h\left( \frac{1}{2}v_e - \frac{1}{4}x_e + \frac{1}{8}y_e \right) \tag{B.3}$$

The above energy is called a zero point energy of the vibration. For simplification, hereafter, we define $E_{vib}(v)$ as $E_{vib}(v)$- $E_{vib}(0)$.

| | $v_e$ (cm$^{-1}$) | $x_e$ (cm$^{-1}$) | $y_e$ (cm$^{-1}$) |
|---|---|---|---|
| $H_2$ | 4401.4 | 121.4 | 0.814 |
| HD | 3812.0 | 90.73 | 0.527 |
| $D_2$ | 3112.8 | 59.67 | 0.288 |

Table.B.1: Vibrational coefficients for the diatomic molecules ($H_2$,HD, and $D_2$)[22].

On the other hand, the rotational energy $E_{rot}(v,J)$ for the v^th^ vibrational is given by

$$E_{rot}(v,J) = B_v J(J+1) - D_v J^2 (J+1)^2 \tag{B.4}$$

where $B_v$ and $D_v$ are rotational and centrifugal distortion constant. Here, $B_v$ and $D_v$ depend on the principal quantum number of the vibration v, and they are given by

$$B_v = B_e - \alpha_e (v + \frac{1}{2}) \tag{B.5}$$

$$D_v = D_e + \beta_e (v + \frac{1}{2}) \tag{B.6}$$

where $B_e$, $D_e$, $\alpha_e$, and $\beta_e$ are tabulated in TableB.2.

| | $B_e$(cm$^{-1}$) | $D_e$(cm$^{-1}$) | $\alpha_e$(cm$^{-1}$) | $\beta_e$(cm$^{-1}$) |
|---|---|---|---|---|
| $H_2$ | 59.338 | $-4.62\times10^{-2}$ | 3.003 | $-3.62\times10^{-3}$ |
| HD | 44.673 | $-2.64\times10^{-2}$ | 1.928 | $-0.64\times10^{-3}$ |
| $D_2$ | 29.908 | $-1.11\times10^{-2}$ | 1.072 | $-0.12\times10^{-3}$ |

TableB.2: Rotational coefficients for each hydrogen atoms[79].

## B.2 Population

The fractional population of the diatomic molecule in an energy state E(v,J) is given by

$$P(v,J) = \frac{Q(J)(2J+1)\exp\left(\frac{-E(v,J)}{T}\right)}{Q} \tag{B.7}$$

where Q is the nomarization factor given by

$$Q = \sum_{v=0}^{\infty}\sum_{J=0}^{\infty} Q(J)(2J+1)\exp\left(\frac{-E(v,J)}{T}\right) \tag{B.8}$$

Here, Q(J) is the degeneracy of nuclear spins given in eq. (3.8) in the text.

TableB.3 shows the energy levels, the Raman shift of the Stokes line, the population, the relative intensity of the Raman scattering, and the parity of the normal (thermally equilibrated) $D_2$.

| v | J | E [cm$^{-1}$] | Raman Shift [cm$^{-1}$] | Population | Raman Scattering Intensity | Parity |
|---|---|---|---|---|---|---|
| 0 | 0 | 0 | 179.1 | 0.181 | 0.298 | Ortho |
| 0 | 1 | 59.8 | 297.6 | 0.204 | 0.201 | Para |
| 0 | 2 | 179.1 | 414.7 | 0.384 | 0.325 | Ortho |
| 0 | 3 | 357.3 | 529.8 | 0.114 | 0.0896 | Para |
| 0 | 4 | 593.7 | 642.5 | 0.0947 | 0.0707 | Ortho |
| 0 | 5 | 887.2 | 752.1 | 0.0142 | 0.0103 | Para |
| 0 | 6 | 1236.3 | 858.2 | 0.0063 | 0.0044 | Ortho |
| 0 | 7 | 1639.3 | 960.1 | $5.2\times10^{-4}$ | $3.7\times10^{-4}$ | Para |
| 0 | 8 | 2094.5 | 1057.4 | $1.3\times10^{-4}$ | $9.2\times10^{-5}$ | Ortho |
| 0 | 9 | 2599.5 | 1149.4 | $6.6\times10^{-6}$ | $4.5\times10^{-6}$ | Para |

TableB.3: Calculated parameters of the rotational band of $D_2$ in the normal condition for the angular momentum state from J=0 to J=9. See Appendix 7.1 for the calculation of Raman scattering intensity.

# Appendix C　Theory of the Raman spectroscopy

## C.1 Principle of the Raman spectroscopy

The Raman spectroscopy is one of the most powerful methods to measure the molecular structure by measuring inelastically scattered lights. When the molecule is exposed by the laser light, the molecule is populated to the excited states with a certain probability. The molecule in the exited states deexcite to the low lying excited states by the light emission. If the molecule returns to the initial ground state, the molecule emits a light with energy equal to the initial laser. This is called the Rayleigh scattering. On the other hand, if the molecule deexcites to the state different from initial states, the molecule emits a light with different energy. This is called the Raman scattering. The relationship between the energy level, photon absorptions, and emissions are illustrated in Fig. 7.1. Note that the contributing photon transitions are predominantly E1 (electric dipole) transition. As shown in Fig. 7.1, the Raman scattering produces a different energy light from the initial light which corresponds to the excited states of the molecule of interest. Thus, the measurement of the light following the Raman scattering gives information on the populations of the initial states of the molecule, and on the energy levels between the initial states and the final state. The Raman spectroscopy has been widely used not only for the study on the structure of the lightest molecules like $H_2$ but also on the complicated macromolecules and even the solid-state materials.

In the study of the Raman spectroscopy on the diatomic molecules such as $H_2$, $D_2$, or $N_2$ at room temperature which is the present experimental condition, the possible states associated with the Raman spectra are restricted to their rotational bands because the energy levels for the vibrational first excited state is too high to be excited by the room temperature energy as exemplified by 4278 K for the first exited state of the $D_2$ molecule.

Usually, a single mode laser light is used for the Raman spectroscopy to avoid the confusion in identifying the levels. The energy difference between the primary laser wave number and the Raman scattering wave number is called as the Raman shift. The Rayleigh scattering, in general, is $10^6$~$10^{14}$ times stronger than the Raman scattering [52]. When the photon energy due to the Raman scattering light is lower than that of the initial laser light, i.e., the initial light excites the molecular states to the higher energy states, we call it the Stokes line. On the other hand, when the energy of the Raman scattering light is higher than the initial laser light, we call it the anti-Stokes.

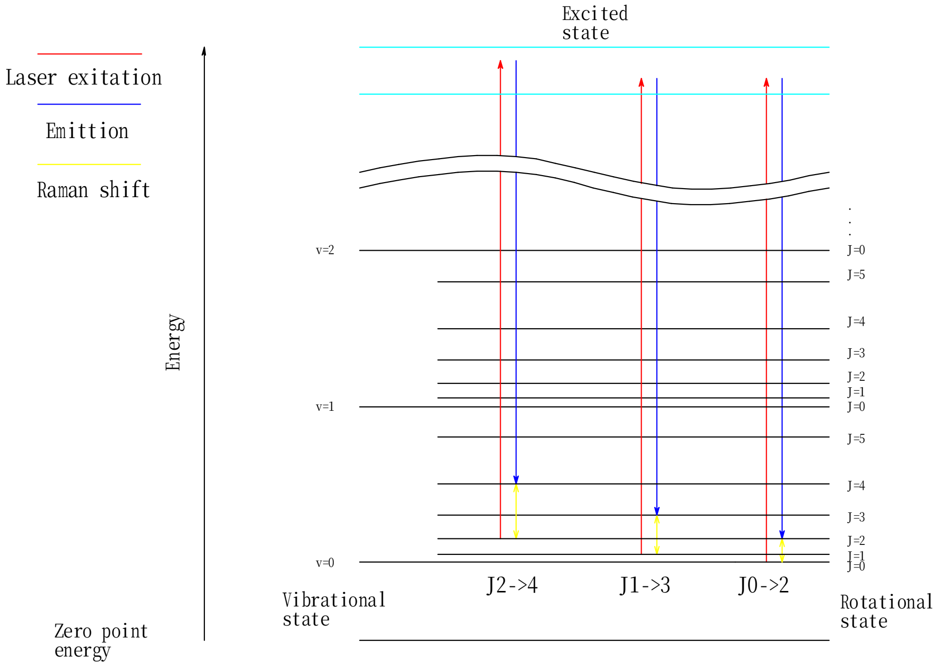

Fig 7.1: The scheme of Rayleigh scattering and Raman scattering for the vibrational and rotational bands of the hydrogen diatomic molecule. The molecules are exited by the laser light with an arbitrary wave length shown by the red lines and followed by photon emissions shown by the blue lines. The deexcitation to the ground state, i.e., elastic scattering is called as the Rayleigh scattering, and the deexcitations to the excited states are called as the Raman scattering. The Stokes, anti-Stokes lines correspond to the photon energies lower, and higher than the primary laser wave length, respectively.

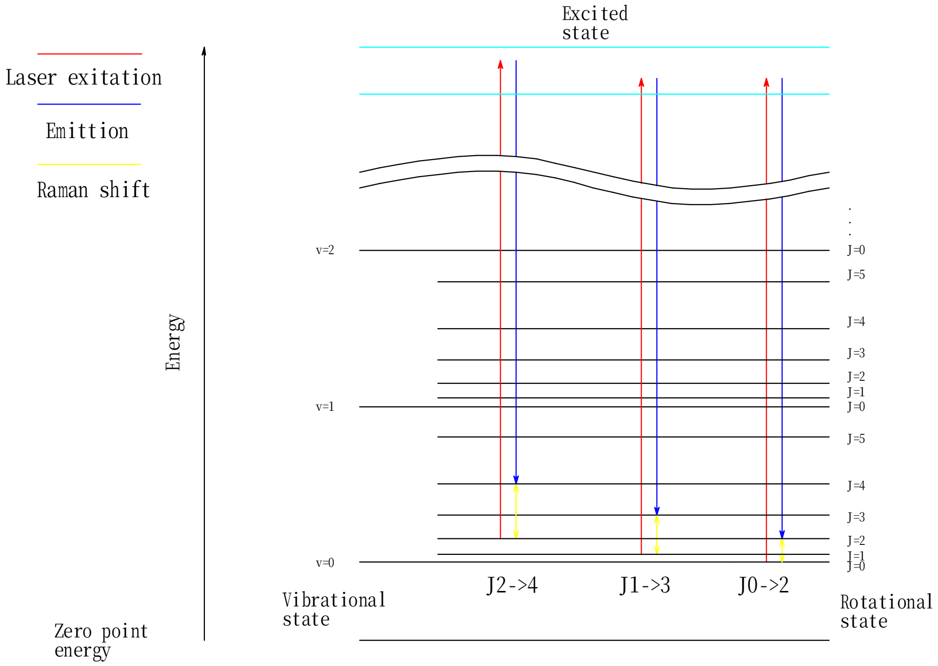

Fig 7.2: Raman scattering between the rotational states. The red lines correspond to the excitation by the primary laser lights and the blue lines correspond to the deexcitations. The yellow lines are the Raman shifts.

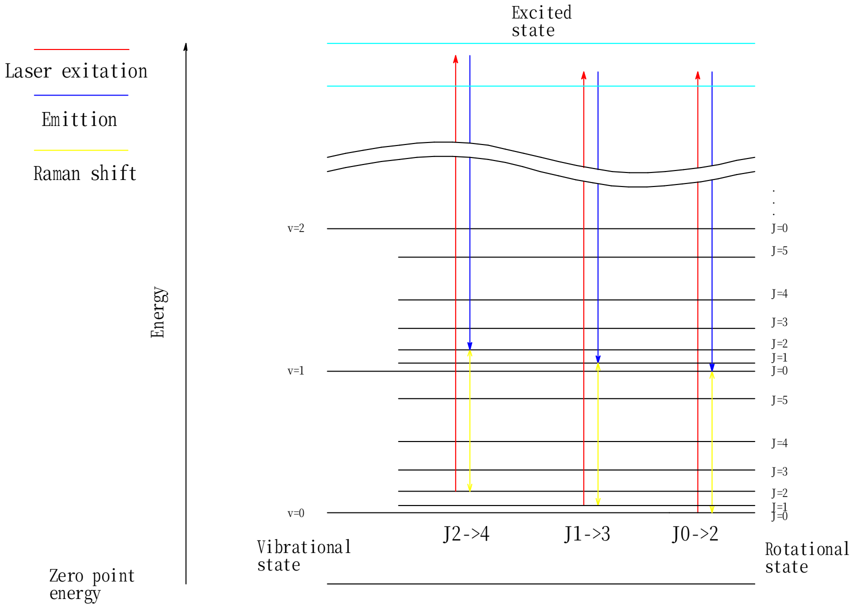

Fig 7.3: Raman spectrum for the vibrational states (Q-branch)

## C.2 Cross section of the Raman scattering

The time averaged photon intensity, I, per unit solid angle is considered in this section. We consider an intensity of the Raman transition whose transition is denoted by v,J->v',J'. Suppose that this transition is induced by the laser propagating to the z direction with the polarization in the y direction (Fig 7.4). Then, the intensity is given by the formula eqs. (C.1) and (C.2).

$$I_y(\mathrm{v},J \rightarrow \mathrm{v}',J') \propto \nu'^4(\mathrm{v}+1)\left[\alpha^2 + \frac{4}{45}B_{JJ'}\gamma^2\right]P(\mathrm{v},J) \qquad (C.1)$$

$$I_z(\mathrm{v},J \rightarrow \mathrm{v}',J') \propto \nu'^4(\mathrm{v}+1)\left[\frac{1}{15}B_{JJ'}\gamma^2\right]P(\mathrm{v},J) \qquad (C.2)$$

where $B_{JJ}$ is the Placzeck Teller coefficient and the explicit expressions for $B_{JJ'}$ are given in eqs.(C.3), (C.4), and (C.5) for each ΔJ=+2,J, and –2, respectively [76][77]. v' is frequency of the Raman scattering light whose energy corresponds to the sum of the initial laser energy and the Raman shift. α and γ mean the averaged polarizability and its anisotropy respectively. The numerical values of α and γ calculated for (v0,J->v0,J+2) and (v0,J->v1,J) of the $D_2$ molecule are tabulated in Table C.4 and Table C.5.

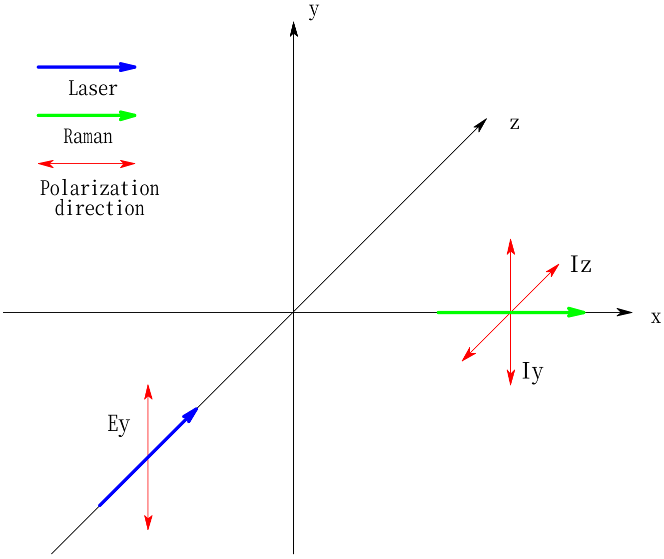

Fig 7.4: Scheme showing the laser polarization and the polarizability of the molecule

$$B_{j,j+2} = \frac{3(j+1)(j+2)}{2(2j+1)(2j+3)} \tag{C.3}$$

$$B_{j,j} = \frac{j(j+1)}{(2j-1)(2j+3)} \tag{C.4}$$

$$B_{j,j-2} = \frac{3(j-1)j}{2(2j-1)(2j+1)} \tag{C.5}$$

| J | $\alpha_{02}$ | $\gamma_{02}$ |
|---|---|---|
| 0 | 0 | 2.0732 |
| 1 | 0 | 2.0812 |
| 2 | 0 | 2.0933 |
| 3 | 0 | 2.1094 |

Table C.4: Numerical values of α and γ factor for (v0,J->v0,J+2) of $D_2$ for the 488nm Radiation[78].

| J | $\alpha_{10}$ | $\gamma_{10}$ |
|---|---|---|
| 0 | 0.6563 | 0.5413 |
| 1 | 0.6568 | 0.5422 |
| 2 | 0.6578 | 0.5439 |
| 3 | 0.6593 | 0.5464 |

Table C.5: Numerical values of α and γ factor for (v0,J->v1,J) of $D_2$ for the 488 nm Radiation[78].

## C.3 Theoretical calculation of the Raman spectra

In this section of appendix C, we demonstrate the calculated results of the Raman spectra for the $D_2$ molecule for easy understanding of the spectra experimentally observed. The calculations were done for the Raman spectra of both the rotational band on the ground state and the first excited state of the vibrational state, respectively.

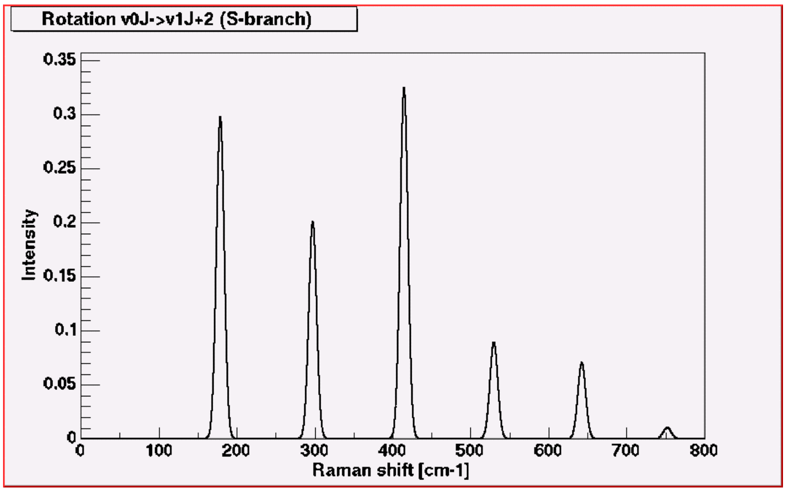

Fig 7.5: Theoretical Raman spectrum of the $D_2$ rotational band. Each peak has a Gaussian shape with a width of 5cm$^{-1}$. The peak heights are normalized so that their sum may be unity.

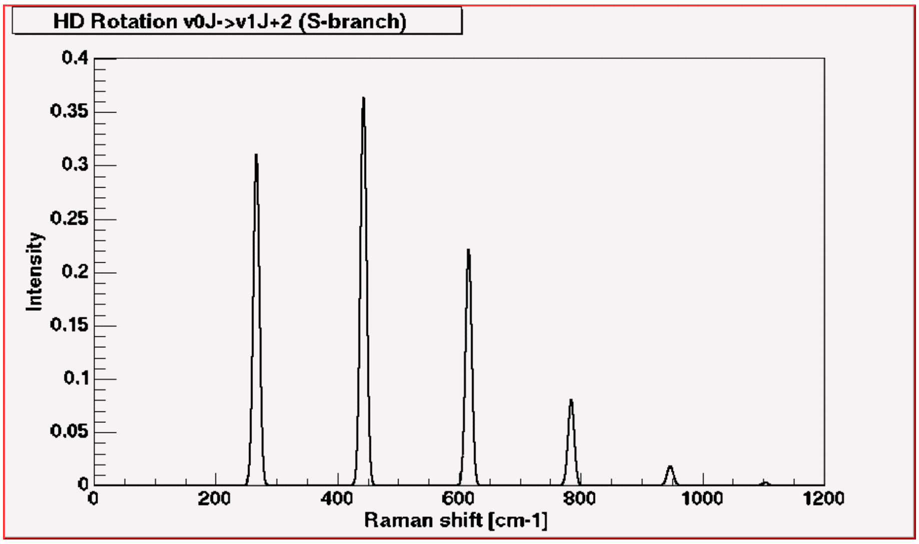

Fig 7.6: Theoretical Raman spectrum of the $D_2$ rotational band. Each peak has a Gaussian shape with a width of 5cm$^{-1}$. The peak heights are normalized so that their sum may be unity.

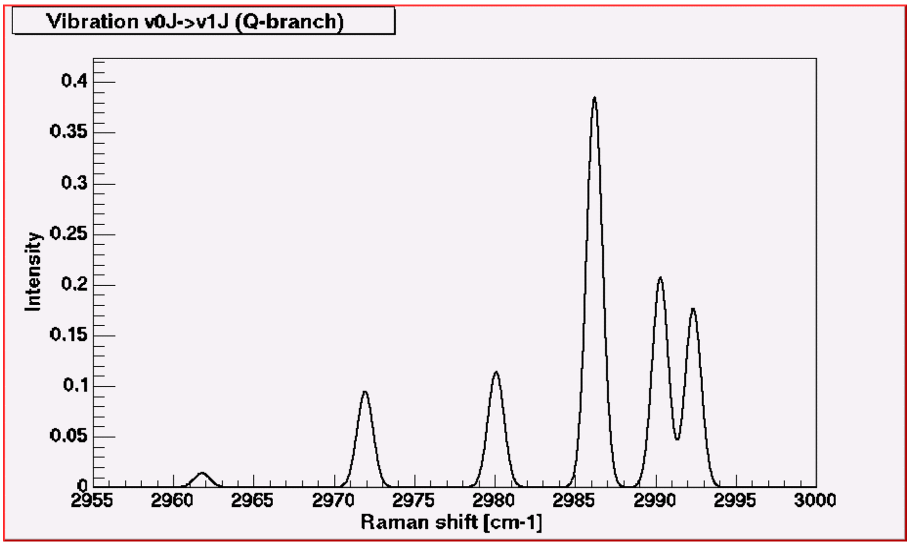

Fig 7.7: Theoretical Raman spectrum of the vibrational spectrum. Each peak has a Gaussian shape with a width of 0.5cm$^{-1}$ width. The peak heights are normalized so that their sum may be unity.

# References

---

[1] E.Fermi and L.Marshal, Phys.Rev.71, 666 (1947)

[2] P.G.Harris et.al., Phys.Rev.Lett. 82, 904 (1999)

[3] S.Arzumanov et.al., Phys.Lett. B483, 15 (2000)

[4] P.R.Huffman et.al., Nature 403, 62 (2000)

[5] V.V.Nesvizhevsky et.al., Nature 415, 297 (2002)

[6] S.Arumanov et.al. Phys.Lett. B483, 15 (2000)

[7] R.Golub, Phys.Lett. 38A, 177 (1972)

[8] R.Golub and J.M.Pendlebry, Phys.Lett. 53A, 133 (1975)

[9] R.Golub et.al., Z.Phys.B51, 187 (1983)

[10] C.L.Morris et.al. Phys.Rev.Lett. 89, 272501 (2002)

[11] SUNS in PSI, http://ucn.web.psi.ch

[12] C.-Y.Liu, A.R.Young, and S.K.Lamoreaux, Phys.Rev.B62, 3581 (2000)

[13] F.Atchison et.al., Physical review B68, 094114 (2003)

[14] LINAC in KURRI, http://www.rri.kyoto-u.ac.jp/LaFa/ela.htm

[15] G.W.Collins.et.al., Phys.Rev.B44, 6598 (1991)

[16] R.Golub, D.J.Richardson, and S.K.Lamoreaux, “Ultra cold neutron”, Adam Hilger, Bristol (1991)

[17] Dissertation of Chen-Yu Liu, “A Superthermal Ultra-Cold Neutron Source”, Princeton University, (2002)

[18] F.Reif “Fundamentals of statistical and thermal physics”, McGraw-Hill (1965)

[19] A.P.Serebrov et.al, Phys.Lett.A 309, 218 (2003)

[20] Z-Ch.Yu, S.S.Malik, and R.Golub, Z.Phys.B62, 137 (1986)

[21] M.Nielsen and H.B.Mϕller, Phys.Rev.B3, 4383 (1971)

[22] P.C.Souers “Hydrogen Properties for Fusion Energy”, University of Carifornia, Barkeley (1986)

[23] F. Atchison et.al., “Calculated values for heating, particle fluxes and activation in components of the UCN source, SUNS”, PSI technical memorandum, TM-14-02-02, Sept. 2002.

[24] F. Atchison, private communication

[25] J.T.Kummer, J.Phys,Chem. 66, 1715 (1962)

[26] I.F.Silvera, Rev.Mod.Phys.52, 393 (1980)

[27] Y.Y.Milenko et.al., Soviet j.low.temp.phys1, 382 (1975)

[28] K.Yagi, “Gensikaku Buturigaku”, Asakura Shoten (1990)

[29] V.Shevtsov et.al J.Low.Temp.Phys.114, 431(1999)

[30] D.W.Trainor, D.O.Ham, and F.aufman, J.Chem.Phys.58 4599 (1973)

[31] W.M.Jones and D.F.Dever, J.Chem.Phys. 60 2900(1974)

[32] G.N.Whyte, Radiat.Reseach.18, 265 (1963)

[33] D.Combecher, Radiat.Reseach.84, 189 (1980)

[34] J.R.Gaines, R.T.Tsugawa and P.C.Souers, Phys.Rev.Lett.42, 1717 (1979)

[35] J.D.Ster and J.R.Gaines et.al., Phys.Rev.B37, 1482 (1988)

[36] Y.Cao, J.R.Gains, P.A.Fedders, and P.C.Souers, Phys.Rev.B37, 1474 (1988)

[37] A.S.Iskovskikh, Sov.Phys.JETP 64, 1085 (1986)

[38] G.W.Collins, W.G.Unites, E.R.Mapoles, and T.P.Bernat, 102 Phys.Rev.B53, (1996)

[39] D.E.Jennings, A.Weber, and J.W.Brault, Applied Optics, 25, 284 (1986)

[40] M. Devoret, N.S.Sullivan, D.Esteve, and P. Deschamps, Rev.Sci.Inst.51(9), 1220, 1980

[41] A.Honig, M.Lewis, Z.-Z.Yu, and S.Yucel Phys.Rev.Lett.56, 1866 (1986)

[42] S.Yucel, N.Alexander, and A.honig Phys.Rev.B42, 820 (1990)

[43] V.Shevtsov, E.Ylinen, P.Malmi, and M.Punkkinen, Phys.Rev.B62, 12836(2000)

[44] Specification sheet of “UNIOHASE model 2013 Argon Ion Laser”

[45] Araldite®, http://www.araldite.com

[46] MOJO, http://www.phys.canterbury.ac.nz/mjuo/astronomy_mount_john.html

[47] ROOT, http://root.cern.ch

[48] OXISORB® is obtained from the MESSER company and in Switzerland distributed by Sauerstoffwerke Lenzburg AG.

[49] N.S. Sullivan, D. Zhou, and C.M. Edwards, Cryogenics 30, 734 (1990)

[50] Jan Van Kranendonk, "Solid Hydorogen", Pleum press, New York and London (1983)

[51] Y.Y.Milenko and R.M.Sibileva, Soviet journal of low temperature physics 1, 382 (1975)

[52] A.Compaan, A.Wagoner, and A.Aydinli, Am.J.Phys.62 (7) 639 (1994)

[53] Klaus Kirch, private communication

[54] Richard B. Firestone eighth edition, "Table of isotope", John Wiley & Sons, Bradford, (1996)

[55] W. Woolley, R. B. Scott, and F. G. Brickwedde, J. Res. Natl. Bureau. Stand. 41, 379 (1948)

[56] H.Spitzer, G.S.Bauer and T.Hifmann, Proc.Int.Workshop on Cold Moderators for Pulsed Neutron Sources, Argonne (1997)

[57] K.Kobayashi et.al., Annu.Rep.Res.Reactor Inst.Kyoto Univ. Vol.22 142 (1989)

[58] Swagelok®, http://www.swagelok.com/

[59] Geant4, http://wwwasd.web.cern.ch/wwwasd/geant4/geant4.html

[60] A.Veyssiere, H.Beil, R.Bergere, P.Carlos and A.Lepretre, Nucl.Phys.A, 159, 561 (1970)

[61] S.C.Fultz, R.L.Bramblett, J.T.Caldwell and N.A.Kerr, Phys.Rev.127, 1273 (1962)

[62] JENDL-3.2, http://wwwndc.tokai.jaeri.go.jp/jendl/j32/j32.html

[63] H.Hirayama, and T.Nakamura, Nucl.Inst.Meth.147, 563 (1977)

[64] J.W.Conant, F.J.Edeskuty, J.E.Hustib, and F.T.Thome, Cryogenics 15, 12 (1975)

[65] G.N.Whyte, Rad.Research 18,265 (1963)

[66] V.G.Anicich and J.H.Futrell, International journal of mass spectrometry and ion physics, 55, 189 (1983)

[67] P.Van der Donk, F.B.Yousif and J.B.A.Mitehell, Phys.Rev.A43, 5971 (1991)

[68] L.W.Nelms and H.G.Carter, "Nuclear-radiation-induced conversion of parahydrogen to orthohydrogen", Tech.Rep.FZK 351-352, NASA, (1968)

[69] E.B.Iverson, J.M.Carpenter, Proceeding of ICANS-XVI 16th Meeting of the International Collaboration on Advanced Neutron Sources, "Kinetics of Irradiated Liquid Hydrogen", May 12-15, (2003)

[70] H.W.Kohn, E.H.Taylor, J.Phys.Cem63, 500 (1959)

[71] M.Cordonnier, D.Uy, R.M.Dickson, K.E.Kerr, Y.Zhang, and T.Oka, J.Chem. Phys.113, 3181 (2000)

[72] M. Quack, Mol. Phys. 34, 477 (1977)

[73] V.Shevtsov et.al J.Low.Temp.Phys.104, 211(1996)

[74] G.W.Collins, P.C.Souers, J.L.Maienschein, and E.R.Mapoles, Phys.Rev.B.45, 549 (1992)

[75] T.Momose, C.M.Lindsay, Y.Zhang, and T.Oka, Phys.Rev.Lett.21, 4795 (2001)

[76] G.Placzek and E.Teller, Zeitschrift für Physik 81, 209 (1933)

[77] Derek A.Long, “The Raman effect”, John Wiley & Sons, Bradford, (2001)

[78] C.Schwartz and R.Roy, Journal of molecular spectroscopy 121, 420-439 (1987)

[79] H.G.M.Edwards, D.W.Farwell, A.C.Gorvin, and D.A.Long, Journal of Raman spectroscopy vol.17, 129-131 (1986)

[80] G.W.Collins.et.al., Phys.Rev.Lett.65, 444 (1990)

[81] J.R.Gains, R.T.Tsugawa, and P.C.Souers, Phys.Rev.Lett.42, 1717 (1979)